Small-angle X-ray and neutron scattering

Cy M. Jeffries[1]✉, *Jan Ilavsky*[2], *Anne Martel*[3], *Stephan Hinrichs*[4], *Andreas Meyer*[4], *Jan Skov Pedersen*[5], *Anna V. Sokolova*[6] *and Dmitri I. Svergun*[1]✉

Abstract | Small-angle scattering (SAS) is a technique that is able to probe the structural organization of matter and quantify its response to changes in external conditions. X-ray and neutron scattering profiles measured from bulk materials or materials deposited at surfaces arise from nanostructural inhomogeneities of electron or nuclear density. The analysis of SAS data from coherent scattering events provides information about the length scale distributions of material components. Samples for SAS studies may be prepared in situ or under near-native conditions and the measurements performed at various temperatures, pressures, flows, shears or stresses, and in a time-resolved fashion. In this Primer, we provide an overview of SAS, summarizing the types of instrument used, approaches for data collection and calibration, available data analysis methods, structural information that can be obtained using the method, and data depositories, standards and formats. Recent applications of SAS in structural biology and the soft-matter and hard-matter sciences are also discussed.

[1]*European Molecular Biology Laboratory, Hamburg Unit, Deutsches Elektronen-Synchrotron, Hamburg, Germany.*

[2]*Advanced Photon Source, Argonne National Laboratory, Lemont, IL, USA.*

[3]*Institut Max Von Laue Paul Langevin, Grenoble, France.*

[4]*Institut für Physikalische Chemie, Universität Hamburg, Hamburg, Germany.*

[5]*Department of Chemistry and Interdisciplinary Nanoscience Center (iNANO), Aarhus University, Aarhus C, Denmark.*

[6]*Australian Centre for Neutron Scattering, Australian Nuclear Science and Technology Organisation (ANSTO), Lucas Heights, New South Wales, Australia.*

✉*e-mail: jeffries@embl-hamburg.de; svergun@embl-hamburg.de*

https://doi.org/10.1038/s43586-021-00064-9

Small-angle X-ray scattering (SAXS) and small-angle neutron scattering (SANS) are widely used techniques for accessing the organization of materials at the ångstrom to micrometre length scale[1–10]. SAXS and SANS are based on the measurement of the intensity, I, of scattered X-rays or neutrons as a function of the scattering angle. The intensities are a summed convolution of the angle-dependent interference of the squared scattering amplitudes of X-ray or neutron spherical waves arising from all atoms illuminated within an incident beam. The resulting intensity pattern, $I(q)$, is expressed as a function of the magnitude of the momentum transfer vector $\mathbf{q}$, namely $\mathbf{q} = 4\pi\sin\theta/\lambda$, where 2θ is the scattering angle and λ is the radiation wavelength. There is a reciprocal relationship between the scattering angle and the length scales probed in the sample interior, $d = 2\pi/q$. As a result, the scattering intensities relate to the structures and the distribution of subcomponents either within the occupied volume elements of bulk materials (measured using a transmission geometry; FIG. 1a,b) or deposited at surfaces (when using grazing incidence[11–15]; FIG. 1c,d). Consequently, small-angle scattering (SAS) can be used to probe the structure of almost any material ranging from biomolecules, polymers and nanocomposites[8,16–23] to metal alloy precipitates, liquid clusters, liquid crystals, glasses, emulsions and colloidal suspensions. Further applications include analysing phase separation and formation[24,25], semiconductor and integrated-circuit surface design[26,27], concrete[28], and chocolate and, even, cheese manufacturing[29,30].

The simplest experimental set-up for a classical SAS experiment (FIG. 1a) consists of a source of X-rays or neutrons and a set of optical devices that define the beam energy and shape the beam geometry and direction (collimation). A sample is placed in the incident beam and the scattering profile is recorded on a 2D detector. For ultra-small or very-small-angle scattering applications, for example ultra-small-angle X-ray scattering (USAXS) and very-small-angle neutron scattering (VSANS), additional optical elements may be installed after the sample to access extremely low q values. Scattering arises due to the interaction of the incident beam with the atoms in the beam path. See BOX 1 for definitions of common scattering terms such as the atomic scattering factor, coherent and incoherent scattering, the scattering length, the average scattering length density and the contrast.

Each atom has a certain probability of scattering or absorbing an incident X-ray photon or neutron at a particular energy, which is described by its scattering factor. The probability of producing a scattering event — a change in direction of the incident X-ray photon or neutron through any given solid angle per unit time — is known as the differential scattering cross section, which is measured in square centimetres or barns (1×10^{-24} cm^2). The scattering cross section describes the magnitude of the interaction between an atom and an applied X-ray or neutron field that yields a particular type of scattering event, taking into account the flux (the number of photons or neutrons delivered per unit time) and energy. The scattering cross section is

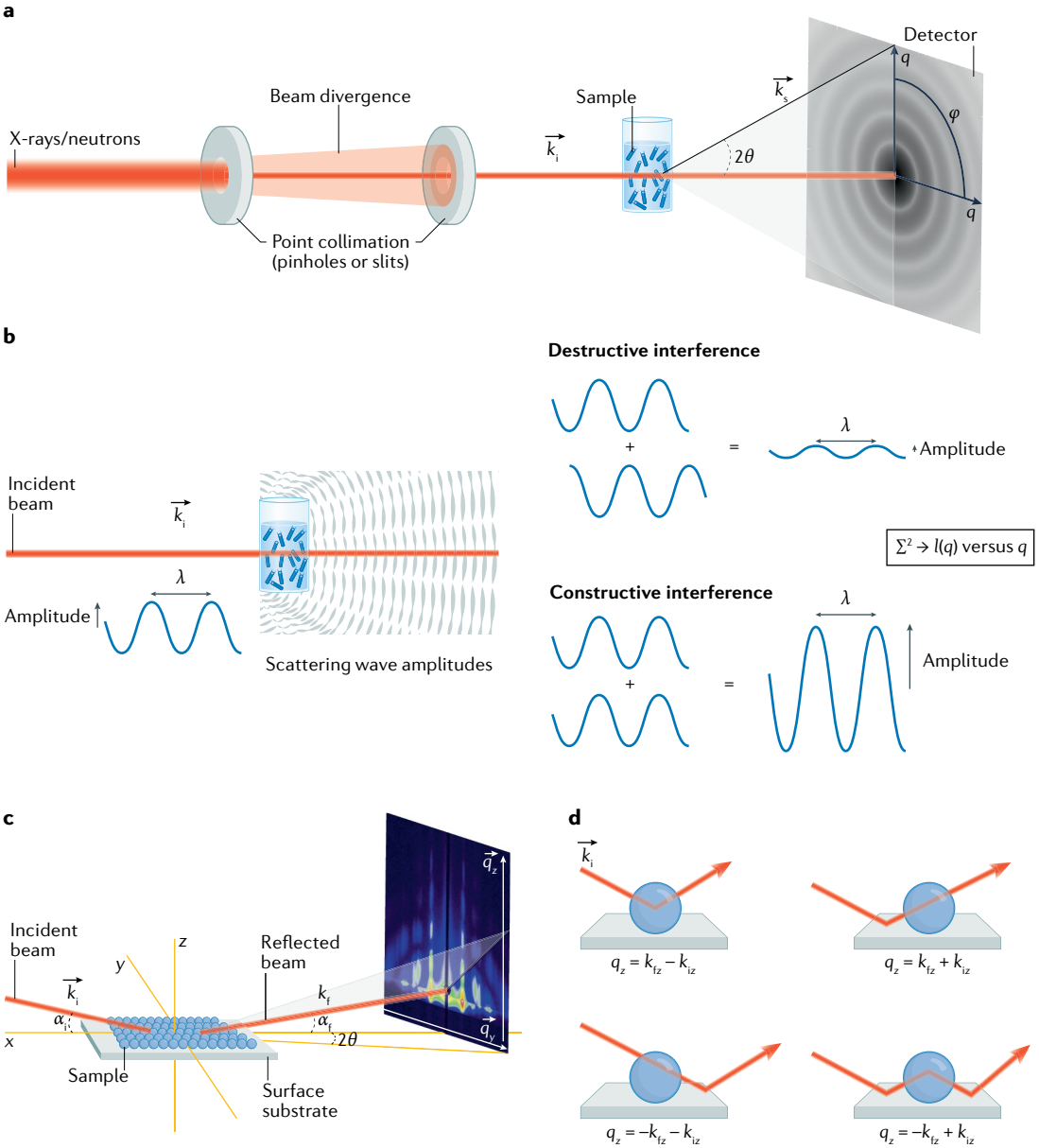

Fig. 1 | **Transmission and GISAS. a** | Transmission geometry set-up for small-angle X-ray scattering (SAXS) or small-angle neutron scattering (SANS) involving delivering a collimated beam through a sample. As the incident beam, k_i, travels through a sample, an extremely small portion of it interacts with the atoms to generate scattering events, k_s. The intensity of the scattered radiation is collected on a detector, the angular dependence of which is expressed in terms of momentum transfer, q. For isotropic scattering systems, the intensity at any point in q on the detector is (within statistical variance) the same and may be averaged around the azimuthal angle φ to generate a 1D isotropic $I(q)$ versus q scattering pattern. **b** | X-rays and neutron beams may be viewed as waves, or field vectors that propagate towards a sample with a wavelength, λ, and amplitude. When the incident beam is scattered elastically (no change in λ) and if preserved distance correlations exist between the scattering centres, a coherent wavefront develops that emanates from the sample where both constructive and destructive interference occurs in the wave amplitudes. The magnitude of the coherent scattering amplitudes as a function of angle relates to spatial correlations between scattering centres. Scattering amplitudes are not accessible experimentally; however, their squared magnitude yields scattering intensities that are measured on a detector. **c**,**d** | Grazing incidence small-angle scattering (GISAS). **c** | An incident X-ray or neutron beam, with wave vector k_i, hits the surface at very low incident angles α_i. The direct reflected beam, k_f, at α_f is covered by a beam stop in front of a 2D detector. An additional rod-like beam stop often covers the roughness scattering of the sample along q_z. Any electron density fluctuations inside the illuminated portion of the surface cause scattering in q_y and q_z directions onto the 2D detector. **d** | The four predominant grazing incidence scattering events described by the distorted-wave Born approximation (DWBA). The incident beam has four possibilities to interact with a scatterer (here, a sphere), which is free standing or buried in a thin layer on top of a surface substrate. The four outgoing wave vectors are able to interfere coherently, giving rise to the effective form factor of DWBA. Each wave is weighted by the corresponding Fresnel reflection coefficient and by the roughness of deposited layers and substrate.

Summed convolution
The scattering intensities, $I(q)$, may be conceptualized as the squared sum of the scattering wave amplitudes emanating from each scattering point. For coherent-elastic scattering events, if the distances between the scattering centres are spatially correlated, then the magnitude of the final scattered wave amplitudes (FIG. 1b) is dependent on the number and distribution of individual scattering centres and their respective scattering 'power' (the scattering length density).

Transmission geometry
A small-angle scattering (SAS) instrument configuration in which an incident X-ray or neutron beam travels through a sample that is placed in the beam path (typically perpendicular to the incident beam direction). The level at which the incident beam transmits through the sample is determined by numerous factors including the X-ray or neutron energy, the absorption and scattering properties of the sample and its thickness.

Grazing incidence
A small-angle scattering (SAS) instrument configuration in which an incident X-ray or neutron beam is directed at a very low incoming incident angle (the grazing incidence angle) towards a sample that is deposited on a surface (FIG. 2). The incident beam and the reflected beam generate scattering events that are dependent on numerous factors including the incident X-ray or neutron wavelength, the absorption and scattering properties of the sample, and the tilt angle of the sample surface relative to the incident beam.

quantified by the scattering length, b, typically expressed in centimetres.

At the energies used for most SAXS experiments (4–20 keV), the elastic scattering of X-ray photons may be viewed as occurring from the interaction between the incident X-ray field and individual electrons, without an associated change in energy. A free electron has a defined scattering length determined by the classical electron radius known as the Thomson scattering length (2.8179×10^{-13} cm). As atoms have different numbers of electrons, the elastic or coherent scattering length of atoms scale to the atomic number, and the more electrons an atom has, the more likely an elastic scattering event will occur; for example, a gold atom has a greater probability of scattering X-rays than a carbon atom. Electrons also have an associated inelastic cross section, where both a change in the energy and direction of a scattered X-ray photon occurs (also known as Compton scattering). Inelastic X-ray scattering is typically orders of magnitude smaller than elastic scattering and is linked to electron bonding and orbital/valence occupancy states. The excitations and associated energy changes of photons are analysed using techniques such as non-resonant X-ray Raman scattering[31,32] or resonant inelastic X-ray scattering[33–35]. Although the contributions of incoherent inelastic X-ray scattering to a SAXS profile are small, they must be considered when using X-ray free-electron laser applications[36].

In a classical SANS experiment, neutrons predominantly scatter from the nuclei of atoms. Each isotope has a unique probability of scattering an incident neutron elastically as this is dependent on neutron and proton content, configuration, volume, spin state and other nuclear properties. Consequently, coherent neutron scattering lengths do not scale with atomic number, cannot be predicted a priori and must be determined experimentally. For example, the thermal neutron coherent scattering length of gold[37] is 0.763×10^{-12} cm, which is similar to carbon (0.665×10^{-12} cm) and deuterium (^{2}H, 0.667×10^{-12} cm). The magnitude and the sign of coherent neutron scattering lengths of the isotopes — that may be positive or negative – is due to the complex nature of potential energy interactions and/or nuclear resonance fields in the compound nucleus that give rise to scattering or absorption. Neutron scattering may also include spin scattering or magnetic scattering components, each with associated cross sections. Further, neutrons may scatter inelastically, losing or gaining energy during a scattering event[38–42].

The measurement of elastic and coherent scattering phenomena provides structural information relating to preserved spatial correlations between scattering centres embedded within, and between, contiguous regions of different average scattering length density, ρ, in a material. Take, for example, the isotropic scattering of a pure, monodispersed population of freely tumbling particles in solution. Here, the scattering length density distribution of a particle, $\rho(\mathbf{r})$, describes the summed contributions of all correlated distance and time-preserved atomic positions within the particle volume. The scattering length density of the solvent is described by ρ_s, which at the length scales probed using SAS is often a featureless scattering matrix because longer-range distance correlations within the population of small solvent molecules are not spatially fixed at any one time. To obtain structural information from the macromolecules without scattering contributions from the bulk solvent, the signal from a matched solvent sample is typically measured separately and subtracted from the sample scattering. The scattering signal therefore refers to the difference $\Delta\rho(\mathbf{r}) = \rho(\mathbf{r}) - \rho_s$, or the excess scattering length density of the macromolecules. The average value,

Box 1 | Definition of common terms in small-angle scattering

Atomic scattering factor
The scattering factor, f, quantifies the magnitude of the scattering component, f', and the imaginary absorption component, if'', of an atom at a given energy. For X-rays, the atomic scattering factor is described as $f = f' + if''$, where the photoabsorption cross section, μ_a, can be calculated from the energy-dependent tabulated values of f'' ($\mu_a = 2r_o\lambda f''$, where r_o is the classical electron radius and λ is the X-ray wavelength).

Coherent scattering
A process where a correlated relationship of constructive or destructive interference is set up between the phase, amplitude and wavelength of elastically scattered radiation emanating from a sample. For a standard small-angle X-ray scattering (SAXS) or small-angle neutron scattering (SANS) experiment, the relationship across a coherent scattering wavefront is determined by time-preserved and spatially correlated atomic positions, or correlated collective atomic motions (phonons) within regions of excess scattering length density inside the sample.

Incoherent scattering
A decoupling in the relationship between the phase(s), amplitude(s) and wavelength(s) of scattered radiation emanating from a sample. Both elastic and inelastic scattering may yield incoherent scattering, which may be caused by, for example, a randomization in the phases of the scattering wave amplitudes from materials lacking time-preserved and spatially correlated or collective motions (for example, amorphous solids, liquids and gases), and for neutrons, incoherent spin scattering arising from uncorrelated nuclear spins within a material.

Scattering length
The probability of an atom to scatter radiation through any given solid angle per unit time, σ, is defined as an atom's scattering cross section, which relates to the scattering length of the atom, b, where $\sigma = 4\pi b^2$. The magnitude of the scattering length, which may refer to either elastic or inelastic scattering, is dictated by the strength of the interaction of an atom with an externally applied electromagnetic field or neutron potential and depends on the configuration of the field (for example, energy, direction and, for neutrons, nuclear spin and magnetic moment polarization). The atomic scattering length may be positive (that is, where the scattered radiation undergoes a 180° shift in phase relative to the phase of incident field) or negative (that is, the phase of the scattered radiation is maintained relative to the incident field). X-ray scattering lengths are always positive. For neutrons, several scattering events are possible, for example nuclear scattering, nuclear spin scattering and magnetic scattering (the latter arising from the magnetic field moments of electrons). The strength of the interaction of a material with neutrons is therefore determined by a combination of the three scattering lengths. Neutron scattering lengths may be either positive or negative.

Average scattering length density, ρ
The combined sum of the scattering lengths of the atoms within a material (in centimetres) within a given volume of material (in cubic centimetres). Therefore, the average scattering length density has units of inverse square centimetres.

Contrast
The contrast, $\Delta\rho$, is the average difference in scattering length density between distinct regions of a sample (for example, of a particle and a supporting solvent). The square of the contrast contributes to the magnitude of the coherent scattering intensities, that is, quantifies the inhomogeneous excess scattering length density fluctuations within the sample. As the contrast limits to zero (contrast-matched case, $\Delta\rho = 0$), the scattering will no longer be due to the form of the particles but solely due to their internal structure (refer to Eq. 2). The contrast may be adjusted, for X-rays by changing the average electron density of the supporting matrix (for example, addition of salts), or for neutrons via isotopic substitution (for example, altering ^{1}H/^{2}H volume ratios).

Form factor
A term describing the squared magnitude of the q-dependent coherent scattering amplitudes arising from regions of excess scattering length density after background scattering contributions have been subtracted. The form factor represents scattering intensities from the distribution of distances between spatially correlated scattering centres within the particle and does not account for the distribution/interactions between the particles, which are described by the structure factor.

Radius of gyration
(R_g). The root mean squared distance calculated from the centre of contrast (typically the centre of mass).

Probable frequency of real-space distances $p(r)$
(Otherwise known as pair-distance distribution function). The inverse Fourier transform of the form factor that converts the reciprocal space scattering $I(q)$ versus q into a frequency distribution, p, of real-space distances, r; that is, $p(r)$ versus r.

$\Delta\rho = \langle \Delta\rho(\mathbf{r}) \rangle$, is known as the contrast and is one of the most important characteristics of a SAS experiment as it defines the magnitude of the scattering signal.

If the average scattering length density of the sample and supporting matrix are identical (contrast-matched), $\Delta\rho$ will be close to 0. Consequently, the resulting background-subtracted scattering intensities will be exceedingly weak, only registering the scattering from any subtle density inhomogeneities in the sample caused by, for example, contributions from internally or externally bound waters, small molecules and ions. However, contrast matching is a critical component of neutron scattering experiments in particular, as it enables the selective interrogation of samples with different regions of average scattering length density. Importantly, for hydrogen (^{1}H) the thermal neutron coherent scattering length is negative (-0.374×10^{-12} cm), whereas for ^{2}H it is positive (0.667×10^{-12} cm). Therefore, substituting ^{1}H for ^{2}H within the sample by using mixtures of ordinary and heavy water[43] or by deuterating molecules radically alters $\Delta\rho$. Scattering contributions from components of different scattering length density may then be selectively contrast 'matched in' or 'matched out' of the data by manipulating $\Delta\rho$, and the structures and dispositions of components and their arrangement within higher-order assemblies or composite materials may be determined. This mechanism of isotopic substitution is routinely exploited for SANS with contrast variation or contrast matching experiments[44,45]. For SAXS, it is possible to perform contrast matching on macromolecules, nanoparticles and porous materials[46–48], although this is difficult as it involves manipulating the electron density and, therefore, the chemistry or physical chemistry properties of the sample.

After background scattering contributions have been subtracted, an isotropic scattering profile can be described by the absolute square of the Fourier transform of $\Delta\rho(\mathbf{r})$ taken over the coherently scattering volume, V:

$$I(q) = \frac{1}{V} \left| \int_V \Delta\rho(\mathbf{r}) \exp(i\mathbf{q} \cdot \mathbf{r}) \mathrm{d}\mathbf{r} \right|^2 . \quad (1)$$

For chaotically tumbling systems of identical particles, the intensity depends only on the magnitude of $\mathbf{q}$:

$$I(q) = n\Delta\rho^2 V^2 P(q) S(q), \quad (2)$$

where n is the number density of particles, V is the volume of a single particle and the rotationally averaged scattering form factor of the particle, $P(q)$, is expressed as:

$$P(q) = \frac{1}{V^2} \left\langle \left| \int_V \exp(i\mathbf{q} \cdot \mathbf{r}) \mathrm{d}\mathbf{r} \right|^2 \right\rangle . \quad (3)$$

Simply, the total scattering may be viewed as a set of individual scattering waves emanating from each scattering point internal to the particle volume (electrons for X-rays; nuclei for neutrons). Assuming elastic scattering, the wave amplitudes from each individual point-scatter combine into the sum of individual constructive or destructive interferences to form a final wave pattern (FIG. 1b). The level of coherent interference is determined by the spatially correlated distances between the individual scattering points, weighted by each point's probability to scatter an X-ray or neutron (that is, the scattering length of each atom). The combined coherent scattering amplitudes therefore encode information about the spatially preserved excess scattering length density distribution and, ultimately, the structure of the particles. Unfortunately, the coherent scattering amplitudes and their phases are inaccessible experimentally; however, the squared magnitude of the amplitudes manifests as the scattering intensity. Therefore, particle scattering is measured as the scattering intensities, $I(q)$ versus q, where the magnitude and decay of the intensities is dependent on the particle size, structure and contrast The term $S(q)$ in Eq. 2 is the scattering structure factor, which describes the interference of scattering waves from between different neighbouring particles in the sample and should not be confused with structure factors in crystallography that refer to diffraction amplitudes arising from preserved atomic positions between crystal lattice planes. The aim of many SAXS and SANS studies is the interpretation of $P(q)$ and $S(q)$ to obtain information about the excess scattering length density, $\Delta\rho(\mathbf{r})$, through the analysis of $P(q)$ and the interactions between the particles in the sample through the analysis of $S(q)$. For isotropic and dilute scattering systems, $S(q) \sim 1$ (REF.[49]) and the measured $I(q)$ will then represent the $P(q)$ weighted by the product of the contrast and volume squared of the particles (Eq. 2). The primary data analysis from such systems includes calculating the radius of gyration, R_g, and the extrapolated to zero angle or forward scattering intensity $I(0)$, which is related to the particle volume V^2, the probable frequency of real-space distances $p(r)$ and the maximum particle dimension, D_{max}.

The expression of the sample form factor becomes increasingly complicated as internal-structuring and long-range spatial correlations between particles become significant, for example in the presence of orientational bias or ordering that produces anisotropic scattering, for example from oriented fibres, magnetic lattices, stretched samples, samples under shear or strain. Sample orientation becomes important when using grazing incidence small-angle X-ray scattering (GISAXS) or grazing incidence SANS to assess surface structure, ordering and roughness. The q value in grazing incidence geometry is expressed in terms of x,y,z coordinates:

$$q_{x,y,z} = \frac{2\pi}{\lambda} \begin{bmatrix} \cos(\alpha_f)\cos(2\theta_f) - \cos(\alpha_i) \\ \cos(\alpha_f)\sin(2\theta_f) \\ \sin(\alpha_f) + \sin(\alpha_i) \end{bmatrix} . \quad (4)$$

The resulting intensities arising from scattering length density fluctuations at the surface relate to the surface scattering form factor, $P(q)$, and $S(q)$, similar to Eqs. 2, 3, except that both the magnitude and direction of q must be taken into account. An added complexity is that there are different scattering events that occur when describing the total scattering length density distribution at a surface: reflection/scattering through the sample; reflection from the supporting substrate into the sample; and transmission through the sample onto

the supporting substrate and subsequent reflection/scattering from the supporting substrate and multi-reflection events. These processes are compounded by surface defects and produce an effective surface form factor that is described by a distorted-wave Born approximation (DWBA)[12], which is used to model grazing incidence data[50] (FIG. 1d).

Pioneering work on SAXS for metallic alloys was first published by the French scientist Andre Guinier 80 years ago[51,52]. Major theoretical and experimental advances in SAS during the twentieth century were pioneered by P. Debye, O. Kratky, V. Luzzati, O. Glatter and H. Stuhrmann and included contrast variation[53] and the use of spherical harmonics for SAS data analysis[54]. Since the 1980s, experimental progress has concerned the use of high-brilliance synchrotrons (SAXS) and high-flux neutron reactors (SANS), and present-day SAXS/SANS is a highly dynamic and constantly growing field with methodological developments coming from numerous laboratories around the world.

In this Primer, we provide an overview of some of the key aspects of using SAXS and SANS for structural investigations. This includes a description of some of the instruments used for SAS, with an emphasis on the importance of proper calibration to define the correct frame of reference for data interpretation and modelling. We describe approaches for the analysis of SAS data from isotropic scattering systems and numerous applications are presented for interrogating structure and structural responses under a variety of sample conditions and environments, spanning biology, soft-matter physics and hard-matter physics. Given that SAS is a universal and adaptable technique, we do not discuss sample-specific preparation details and sample-specific data analysis approaches for anisotropic systems nor discuss techniques such as inelastic X-ray scattering or, for neutrons, inelastic and quasi-elastic scattering, magnetic scattering and polarized neutron spin scattering. We direct readers to several texts that provide extensive detail on the topics outlined in this Primer and other aspects of SAS for the material sciences[2,4,8,21,38,55–57].

Experimentation

The approach to any SAS experiment relies on configuring the instrument and the sample environment according to the type of sample being analysed. The relationship between the sample and the instrument is inseparable and the approach to any SAS experiment relies on the synergy between, and an understanding of, the type of sample and sample environment with the type and configuration of an instrument[58]. Both the instrument and the data must be calibrated and the sample conditions or environment optimized to obtain reproducible, quantitative and comparative results. Here, the main types of instrument used for SAS experiments are described in addition to data calibration methods. A brief overview of the sample environments often employed for SAS investigations is also presented.

Sample preparation

Sample preparation schemes for SAXS or SANS are almost as diverse as the range of materials that can be investigated (refer to Applications). Samples used for SAS — for example, polymers, non-crystallite materials, metals, organic or inorganic solids, coals, cement and thin films — display varying organization and may require specialized preparation or synthesis on a case by case basis; for example, numerous protocols exist for the preparation of biological macromolecules, which are somewhat unique in that they may be isolated in a pure and monodispersed form[59–61]. All SAS investigations are based on the relationship between the composition and physical state of the sample and a given instrument's parameters[58]; for example, how an incident beam may be optimized to a sample with respect to energy, flux, size and shape, and how the scattering intensities from the sample are detected and quantified in both magnitude and direction.

The X-ray or neutron scattering length density and X-ray or neutron absorption properties of a sample are important parameters to consider as both influence the magnitude of the measured signal. The scattering length density and subsequent contrast of a system (Eq. 1) may be manipulated during sample preparation by altering the element or isotope composition of either a target or a supporting matrix, to maximize or controllably alter the X-ray or neutron contrast of a system. Scattering length density and contrast calculators are available for biological samples[59,62,63] and resources from the National Institute of Standards and Technology (NIST) Center for Neutron Research include the scattering lengths and cross sections of elements and isotopes. Both atomic composition and sample thickness must be considered with respect to sample absorption; the sample thickness becomes especially pertinent for SAXS as many materials strongly absorb X-rays, especially as energy is decreased. Some X-ray energies may also result in unwanted X-ray fluorescence from a sample depending on the elemental composition and chemical state or bonding environment. For example, the X-ray absorption edge of zinc is approximately 10 keV — a common energy used for synchrotron SAXS — and zinc-containing samples may have to be measured at a different wavelength to avoid a high fluorescence background.

For SANS, where neutrons penetrate deep into samples, increasing the sample thickness may be advantageous for generating more scattering events. However, sample thickness is also guided by the sample nuclear isotope absorption properties and the neutron wavelength. For example, ^{10}B or ^{3}He have an enormous thermal neutron absorption cross section compared with the heavier nucleus of aluminium. Too thick a sample may also yield multiple scattering events or an increase in the magnitude of incoherent scattering arising from uncorrelated nuclear spin interactions within the sample, for example for materials rich in ^{1}H. Both multiple scattering and incoherent spin scattering may compromise SANS data quality and complicate data processing and interpretation. In addition, the incident X-ray or neutron flux as well as the beam size or shape are parameters that must be considered as they often determine the volume of sample exposed in the beam, the time a sample is exposed to the beam, radiation damage susceptibility and whether beam geometry corrections are necessary during data calibration and processing. The X-ray or

neutron instrument parameters in combination with optimizing the sample conditions, such as the contrast, volume, size, thickness, mass density, element or isotope composition, may have to be tailored accordingly for a particular SAS experiment. The advantage of SAS is the enormous versatility and adaptability of the instrument–sample relationship that no other technique arguably affords with such scope.

Transmission geometry

SAS is usually performed using transmission geometry, where an incident beam passes through the sample, typically perpendicular to the sample surface (FIG. 1a). The recorded signal represents the summed contribution from the volume fraction and contrast-weighted contributions from all atoms within the illuminated volume. When placed on an absolute scale ($I(q)$, inverse centimetres) the scattering intensities directly relate to the cross section of the sample, allowing quantitative information to be obtained regarding volume and molecular weight, scattering length density distributions, long-range and short-range ordering and bulk structural anisotropy.

Laboratory SAXS instruments

There are two main types of laboratory SAXS instrument: point source/pinhole collimation cameras[64] and Kratky line collimation cameras[65]. These instruments deliver a well-collimated monochromatic beam of X-rays from a source to the sample. Currently, the most commonly used laboratory-based X-ray sources are sealed X-ray tubes with focusing optics that deliver fixed-wavelength X-ray beams using either copper, molybdenum or silver targets (CuKα, 0.154 nm; MoKα, 0.0711 nm; AgKα, 0.059 nm)[66–68]. Higher X-ray flux can be obtained using either a MetalJet X-ray source[69,70], where the target is a stream of molten metal (gallium, 0.135 nm; indium-rich alloys, 0.051 nm), or a rotating anode tube where a solid target rotates to reduce local heat load. Recent advances have allowed the delivery of up to 10^9 photons s^{-1} within a beam of a few-hundred square micrometres, enabling the measurement of dilute polymers and biomacromolecular solutions within minutes and time-resolved investigations on the second timescale[71].

Pinhole and Kratky cameras produce different incident beam geometries. Pinhole cameras deliver the X-rays to the sample as a parallel (that is, not focused), low-divergence (near) point source, ensuring minimal effects are caused by the geometry of the incident beam on the subsequent scattering amplitudes emanating from the sample. When using a point source, there is a direct correspondence between the measured $I(q)$ at each value of q recorded on a 2D detector. Alternatively, the Kratky camera approach delivers the X-ray beam as a line. The line can be described as a set of infinite point sources in a row and, as a result, the scattering amplitudes emanating from any one point along the line become smeared into the slightly offset scattering amplitudes of neighbouring points (see Results). The magnitude of this effect is dictated by the line geometry, specifically its width and length. Therefore, the smeared $I(q)$ versus q profile from a Kratky camera configuration is dictated by both sample composition and beam geometry, and a beam geometry correction is required to convert the data into the final $I(q)$ versus q profile. Alternatively, real-space parameters or models can be smeared so as to describe the smeared scattering data.

The line collimation system illuminates a much larger sample volume than a point source and, therefore, generates more scattering events[72], which can be advantageous when measuring weakly scattering samples such as those composed of light elements (for example, biomolecules in solution). However, deconvoluting the smeared data or generating models or parameters that fit smeared data can be difficult[58]. The difficulty of these approaches depends on the type of sample; for isotropic scattering systems such as dilute proteins or polymers in solution, which are free to sample all rotational and translational states, data deconvolution is relatively straightforward[73–78], whereas data from samples that generate anisotropic scattering become increasingly difficult to deconvolute[58].

Finally, USAXS instruments have been developed that use crystal optics placed after the sample or Bonse–Hart[79,80] devices. Data from these instruments may also require de-smearing corrections[81]. USAXS optics are used to access very low q values and correspondingly large dimensions at the length scale of 1–2 μm (REF.[82]).

Synchrotron SAXS instruments

Most synchrotron sources generate X-rays using relativistic electrons to provide high-flux, high-brilliance and variable-wavelength X-rays. SAXS instruments at these facilities (FIG. 2a–c) have sophisticated optical elements to control beam size (down to a few micrometres), shape and energy distribution profiles (for example, Gaussian or 'top-hat' beam profiles), angular divergence (typically nanoradians) and focusing options (FIG. 2d).

Synchrotron sources afford unique opportunities to design experiments not otherwise possible using laboratory instruments that are typically limited to one wavelength and lower flux. The high brilliance of a synchrotron source combined with the high tunability of the beam size allows for several orders of magnitude more photons to be delivered to a sample (10^{12}–10^{14} photons s^{-1}) compared with laboratory instruments, enabling high-throughput screening[83–87] of low-concentration and limited-volume samples, the use of microfluidic sample delivery systems[88–90] and very fast time-resolved studies. Synchrotrons also allow for the selection of an X-ray wavelength to optimize the scattering and absorption of a material[91] and allow fine-tuning of the wavelength for anomalous SAXS, which is used to probe element-specific X-ray absorption edges to gain information on the spatial disposition of a particular element within a sample[92–97]. Example uses of anomalous SAXS include probing ions associated with metalloproteins, DNA or other types of polyelectrolytes and ions embedded in surfactant micelles or bound to nanoparticles[98–103].

The high flux of synchrotrons allows for data collection on the second to millisecond timescale for regular steady-state experiments, the sub-millisecond scale for time-resolved applications[104,105] and as quick

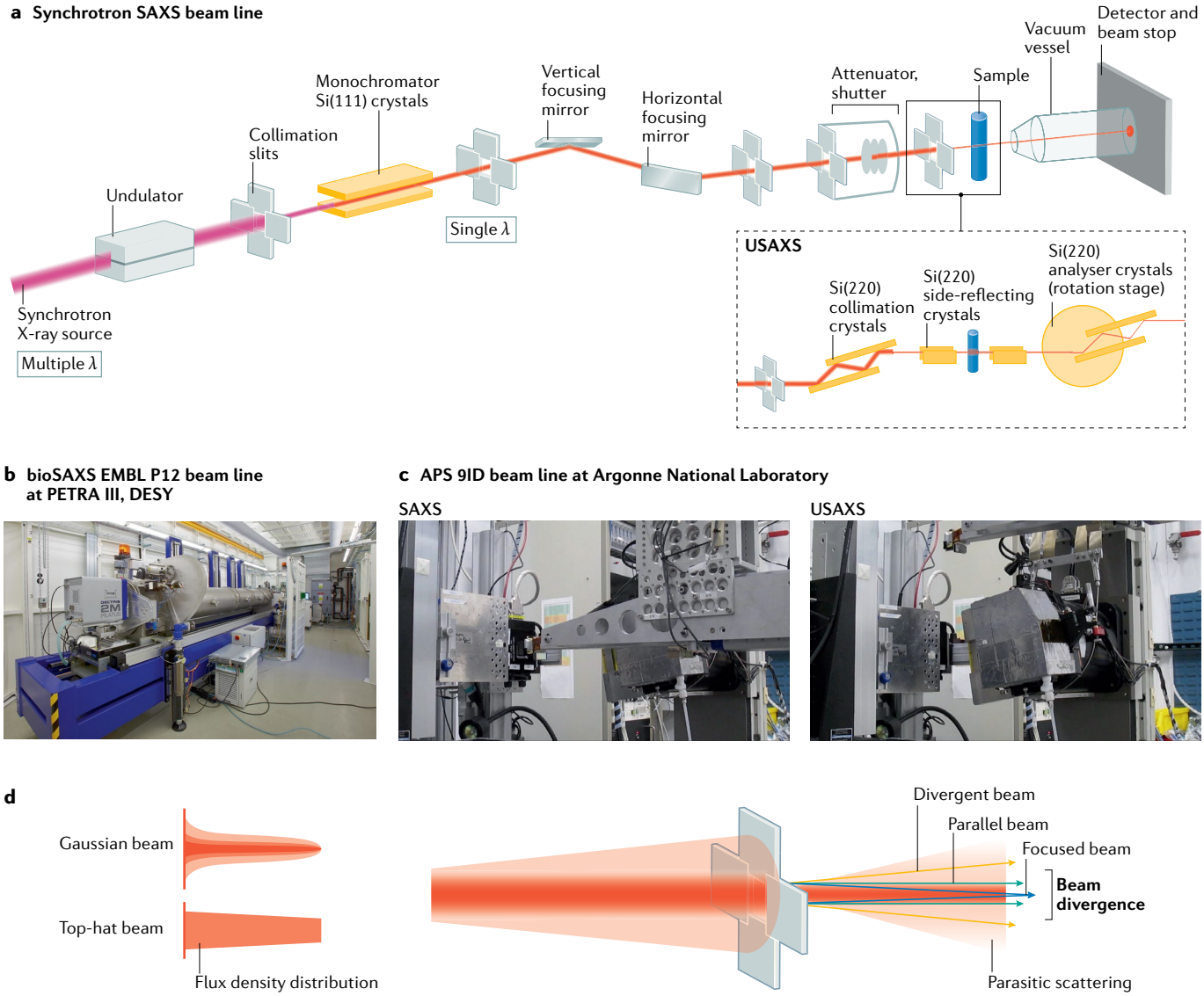

Fig. 2 | **Synchrotron SAXS instruments. a** | Synchrotron X-ray sources consist of relativistic electrons (or positrons) that undergo acceleration perpendicular to the direction of the initial velocity, for example through a set of magnets in an undulator. Electrons radiate multiple-wavelength X-rays. The undulator gap controls the energy spectrum released into the front end of the instrument. X-rays are directed towards a monochromator (for example a double Si(111) crystal), that selects a specific X-ray wavelength. The monochromatic X-ray beam is then shaped by vertical and horizontal focusing mirrors in combination with slits. Additional components include attenuators and shutters that control the X-ray flux and exposure. Ultra-small-angle X-ray scattering (USAXS) operations include installation of silicon crystals after the sample position that redirect the path of the very lowest-angle scattering intensities. **b** | The high-brilliance, low-background EMBL-P12 small-angle X-ray scattering (SAXS) beam line at PETRA III (DESY, Hamburg)[113] has been optimized for the high-throughput and fully automated measurement of extremely weak scattering samples such as dilute biomolecules in solution. The detector and detector tube can be moved to different positions to access different momentum transfer, q, ranges. **c** | The 9ID beam line[118,490,491] at the Advanced Photon Source, Argonne National Laboratory, performs both SAXS and USAXS measurements through robotic swapping of SAXS and USAXS detectors. **d** | The flux density of the beam depends on the shape of the initial source (horizontal and vertical dimensions) and the optical components of the beam line. The flux density may be delivered as a Gaussian, where a majority of the photons are located towards the centre of the beam, or as a 'top hat', where the flux density is more evenly distributed. Scattering or absorption from optical elements in the beam path is unavoidable and contributes to the instrument background. λ, wavelength. Part **b** reprinted with permission from Udo Ringeisen/EMBL, copyright: EMBL. Part **c**, image courtesy of Argonne National Laboratory.

as 100 ps for pump-probe experiments[106–108]. A typical synchrotron-based SAS device can measure about two orders of magnitude in q at once (for example, 0.05–5 nm^{-1}) and more advanced instruments provide an even larger q range. There are two main approaches, implemented separately or together, that can increase the available q range to access low-angle data and, thus, longer vector lengths ($q < 0.05\ nm^{-1}$) or increase q to >5 nm^{-1} for wide-angle X-ray scattering (WAXS) or grazing incidence WAXS. The first approach uses a set of detectors at fixed distances from the sample[86,109,110], in which the detector closest to the sample measures WAXS in parallel with SAXS from a second detector (alternatively, a single detector is moved at varying distance to the sample[93,104,111–117]). In the second approach, the wavelength of the X-ray beam is varied; increasing

Spallation
The process of applying proton bombardment to eject fragments from heavy metal target materials. Used to produce high-flux neutron beams without nuclear fission chain reaction.

the energy increases the accessible q_{max} at an equivalent detector position, as q is proportionate to $1/\lambda$.

The high brilliance of X-ray sources combined with the exceptional adaptability of the beam enables SAXS/USAXS methods to probe orders of magnitude in q and reach q values well below 0.01 nm^{-1} (REF.[118]). For Bonse–Hart-based USAXS, additional double-crystal optical elements can be employed, forgoing the need for beam geometry deconvolution (FIG. 2a). Such devices also enable the use of coherent portions of the incident beam for dynamic X-ray scattering measurements[119]. The brilliance of a synchrotron source simply allows for a sufficient number of scattered photons from the sample to get through the additional USAXS optical components, as opposed to being completely absorbed.

SANS instruments

There are two types of neutron source: nuclear reactors, which deliver a continuous source of neutrons of variable kinetic energy that are produced by nuclear fission events in the reactor chamber (FIG. 3a,b), and spallation sources[120–122], which use the collision of a proton beam with a tungsten or mercury target to generate neutrons, delivering a pulse-structured multi-wavelength beam. Neutrons from either source may be subsequently moderated (for example, through deuterium or cooled with liquid helium) to alter their kinetic energy. The desirable wavelength — or wavelengths if using a polychromatic beam — is selected with a quantifiable wavelength bandwidth ($\Delta\lambda/\lambda$). The neutrons are then delivered to the sample through guides that collimate the neutrons to shape and control beam size, beam divergence and neutron spin parameters. Fluxes per unit area of the beam are significantly lower (10^7–10^{15} s^{-1} cm^{-2}) than X-ray-based techniques and the beam size is typically larger, requiring longer exposure times and more sample. However, as neutrons predominantly interact with the nuclei of elements, or with magnetic fields internal to materials, they are deeply penetrating and, aside from the production of unavoidable secondary ionizing radiation

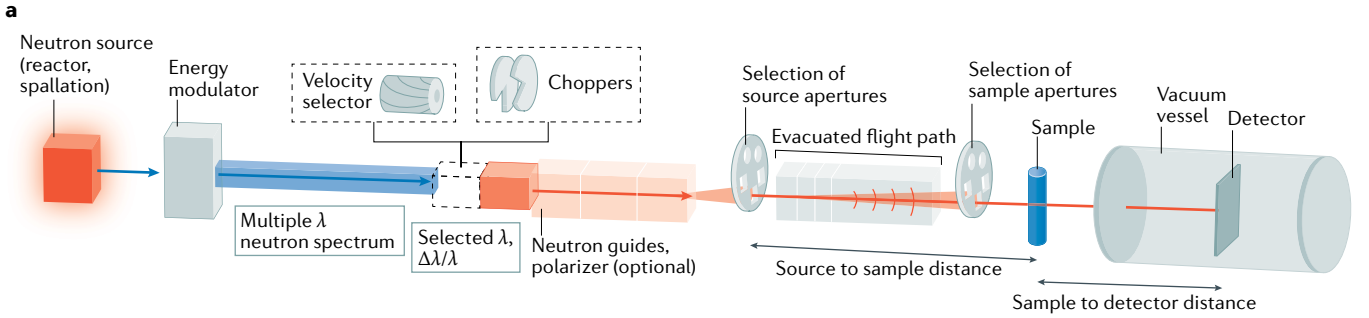

b QUOKKA-SANS and BILBY-ToF-SANS at ANSTO

c D22-SANS at ILL

Fig. 3 | **SANS instruments. a** | Neutron sources include both reactor (continuous) or spallation (pulsed) sources that generate multiple-energy neutrons. Depending on the application, high-energy neutrons from the source may be passed through helium-cooled deuterium to moderate their energy, increasing their wavelength, λ (0.1–2 nm and higher). For monochromatic instruments, the cold neutrons are passed through a fan-like spinning velocity selector or set of choppers, or sometimes a monochromator, which allows neutrons of selected band through to the downstream guides. The neutron guides transport neutrons to the sample via total internal reflection and apertures in the beam define the beam size and divergence. Time-of-flight (ToF) small-angle neutron scattering (SANS) can be designed on both reactors and spallation sources, and operate with a wide wavelength band, selected by a set of rotating choppers. **b** | The 40-m QUOKKA-SANS[131] (left) and single or multi-wavelength BILBY-ToF-SANS[160] (right) instruments in the neutron guide hall of the Australian Centre for Neutron Scattering (ANSTO). **c** | Sample stage area of the D22-SANS instrument at the Institut Laue-Langevin (ILL), showing the large evacuated detector tube after the sample position. Part **b**, image courtesy of Jamie Schulz, Australian Nuclear Science & Technology Organisation (ANSTO). Part **c**, image courtesy of © Ecliptique — Laurent Thion.

(for example γ-rays and X-rays; α-particles and β-particles), are generally less damaging to a sample compared with X-rays that may otherwise radically alter the electronic, that is chemical, environment via X-ray-induced radiation damage. The deeply penetrating nature of neutrons opens up the possibility of installing exotic sample environments[123] such as dielectric rheology devices[124], one or two-plane shear cells[125], high-temperature furnaces[126] and 3D-printed grazing incidence SANS devices[127].

Standard SANS applied to probing the structures of materials using either near-monochromatic or multi-wavelength neutrons relies on the measurement of elastic coherent scattering events. Unlike X-rays, neutrons have an associated 1/2 spin that can generate significant incoherent scattering from materials with disordered or uncorrelated nuclear spin states. Incoherent scattering for standard SANS is particularly evident for samples rich in ^{1}H, such as biomolecules and organic polymers[61,128], and generates high background noise in the coherent scattering profile[129]. Neutrons have a magnetic moment that can be manipulated and used to probe magnetic lattices[6,130]. Devices such as spin polarizers[131–133] are used to align neutron spins and allow the study of complex magnetic interactions or probe internal dynamics[134]. The sample itself may also be spin polarized and a combination of contrast variation and spin contrast variation can be used to improve the quantification of heterogeneous scattering length density distributions[96], as was used to determine the low-resolution structure of the ribosome[135–137]. In addition, magnetic focusing lenses or complex collimation geometries, for example those used in VSANS[138–140], may be used to extend the accessible q range[141,142] in combination with adjusting the neutron wavelength. Large-scale structures in the order of tens of micrometres may be probed with ultra-SANS instruments using Bonse–Hart optic geometry[143] in combination with real-space analysis using spin-echo SANS[144–146], which has diverse applications for the investigation of suspensions[147,148], nanoparticles[149,150] and other processes with large length scales such as the formation of silica thin films[151] and microgranules[152]. Further techniques such as time-involved small-angle neutron experiments allow sub-second and sub-millisecond temporal resolutions[153].

Often, multiple detector positions are used to cover different q ranges in SANS[131,154–157]. The distance of the sample to the detector correlates with the accessible angle that can be measured; therefore, to span a particular q range that encompasses both long and short internal distances within a sample, detector positions are changed during the measurement of the sample. The data recorded from each position are then merged to generate the final SANS profile. The merging process takes into account the sample transmission and the q resolution of the instrument, which is affected by a combination of the neutron wavelength spread ($\Delta\lambda/\lambda$), gravity, instrument geometry (for example, the source to sample and sample to detector distances) and detector pixel spot size[158,159]. For multi-wavelength SANS using reactor and spallation sources and methods that detect scattered neutrons based on their time-of-flight (ToF)[110,123,157,160–163], one detector position can be used to measure a wide angular range; however, this requires complicated data reduction and deconvolution techniques as each incident wavelength neutron generates its own q frame of reference.

Grazing incidence geometry

Instruments configured for grazing incidence or reflection geometry are designed to obtain structural information from materials either deposited on or buried at surfaces or interfaces, effectively analysing correlated nanometre to micrometre scattering length density fluctuations in two dimensions. The incident beam for grazing incidence is set to a low incoming angle or critical angle that is dictated by the composition of the sample material or the supporting substrate.

Both the incident beam and the reflected beam generate scattering events, with angular intensity distributions dependent on the structure of the material near the surface. Scattering provides information on the overall spatial distribution and organization of the sample and the surface roughness. An intense scattering pattern is obtained in grazing incidence geometry as the X-ray beam path length through the film plane is sufficiently long compared with the thickness of the sample. Each scattering pattern takes a few seconds to hours to record, depending on scattering contrast and beam intensity. The bulk scattering from the substrate that supports the sample is reduced because of the limited penetration depth of the incoming beam at the very low glancing angles used in a grazing incidence geometry, where the incident angle is set to near the critical angle of the substrate. The incidence angle is precisely controlled using a tilting sample stage and is typically 0.1–1.0°. The scattering that is recorded with a 2D detector is half covered by the substrate, and as a consequence the scattering is collected from multiple surface scattering events from above the sample horizon. At shallow angles near the critical angle of the substrate, the beam reflects strongly into the detector area and is covered with an additional beam stop. Owing to high reflectance, multiple scattering paths must be considered and calculated within the DWBA as, for example, 'sample islands' distributed across flat substrates[164]. The four terms of the DWBA, illustrated in FIG. 1d, are involved in the scattering process and its waves interfere coherently, giving rise to an effective form factor. Each of the terms must be weighted by the corresponding reflection coefficient. For experiments with low reflectance, for example those at larger incident angles or high levels of sample absorbance or roughness, analysis becomes similar to a SAS transmission geometry. Beside the form factor that arises from objects on flat substrates, ordered assemblies lead to additional Bragg reflections, similar to in an ordinary diffraction experiment. As the recorded scattering is always a product of the square of the form factor and the interference function, the intensity of the Bragg reflections is influenced by the intensity distribution of the form factor. Although the intensity of the reflections are affected by the form factor, the positions of the lattice reflections in terms of q (Eq. 4) are not affected, and the calculation of the lattice parameters

Bragg reflections
Reflections that occur for periodic structures with a spacing d (such as crystal matrices) at a scattering angle θ that is described by the Bragg relation, $2d\sin\theta = n\lambda$, where n is a positive integer and λ the radiation wavelength. This can be observed in bulk or for ordered materials deposited on surfaces when a grazing incidence beam illuminates a 2D lattice with well-defined symmetry-related periodicity.

of an ordered superlattice is straightforward. Grazing incidence small-angle scattering (GISAS) experiments can be performed under varying sample conditions (for example, temperature) to monitor structure changes in physical and chemical processes at the sample surface (see Applications).

Corrections and intensity calibration

The reliability and reproducibility of SAS data have dramatically improved owing to community efforts driven by large facilities and the availability of standards, stable radiation sources and current generation detectors. The uncertainty of the results is related to the uncertainties of data collection and sample parameters. Today, X-ray data collection uncertainty is typically better than uncertainties related to sample parameters such as thickness, homogeneity variations, concentration, imperfections in sample containers and so on. However, what remains critical is that both q-axis and intensity calibration are performed to place the experimental data within a mutual and interpretable frame of reference. Interpretation of data is assisted by proper correction of measured data during reduction to $I(q)$ versus q. This involves multiple steps and correction types, and is typically instrument and technique-dependent.

Instrument q-axis calibration can be performed using silver behenate[165,166] (FIG. 4a,b) or other standards, such as a grating with defined line spacing[167]. The q-axis calibration should be performed when an instrument parameter such as the wavelength or sample to detector

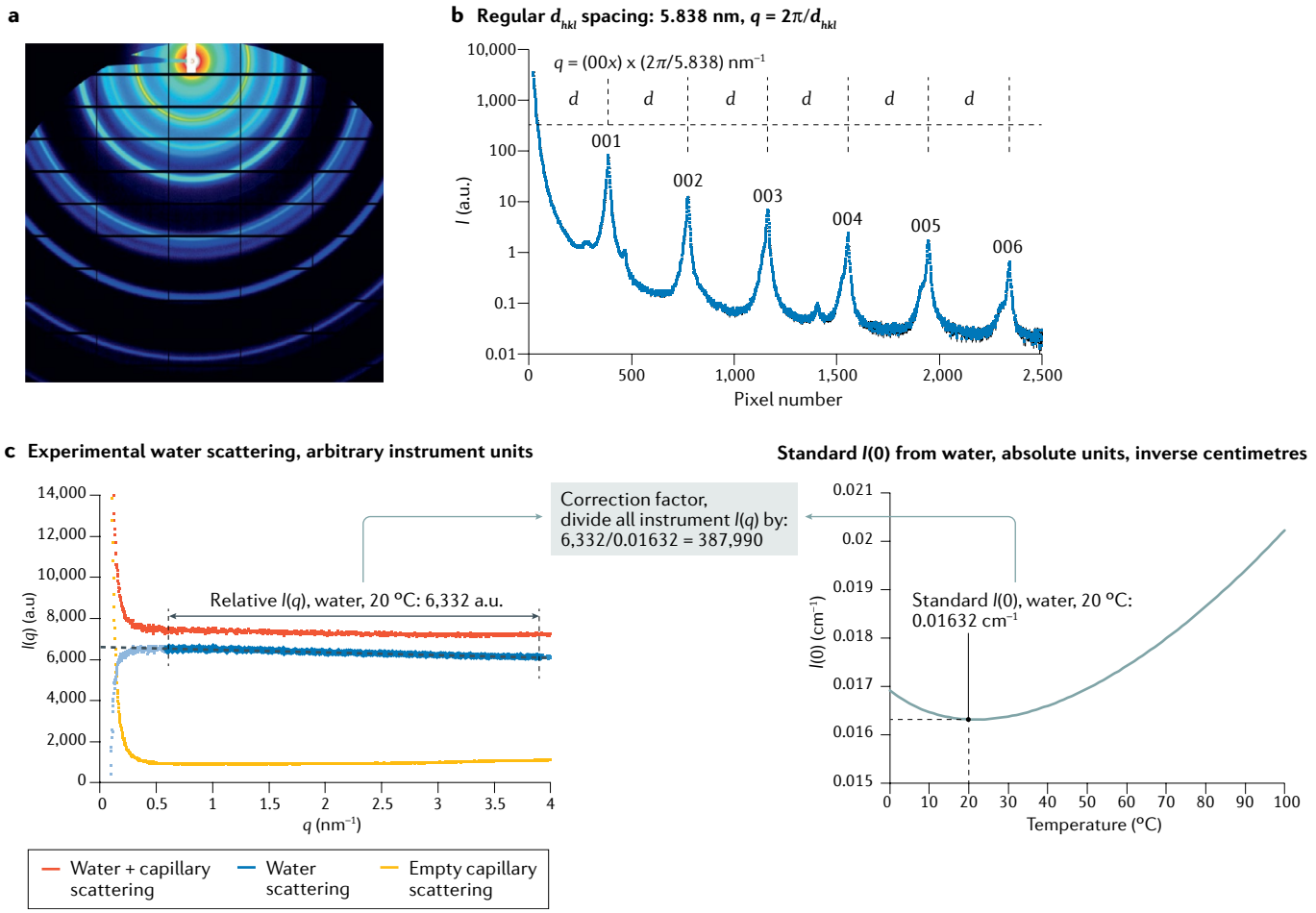

Fig. 4 | **q-Axis calibration and $I(q)$ absolute scaling. a** | Detector image of the Debye–Scherrer powder diffraction rings produced by silver behenate (AgBeh), a long-chain fatty acid silver salt (behenic acid; $CH_3(CH_2)_{20}COO{\cdot}Ag$) used for q-axis calibration. **b** | The corresponding azimuthal averaged 1D powder diffraction profile expressed in terms of arbitrary intensity versus pixel number on the detector. The crystallite structure of AgBeh produces intense d_{hkl} 001 peaks of known lattice spacing, $d_{001} = 5.838$ nm (REF.[165]) (5.8363–5.8381 nm (REF.[492])), $d_{002} = 2.919$ nm, $d_{003} = 1.946$ nm and so on, that may be used to convert the pixel number on the detector into the corresponding q value ($q = 2\pi/d_{hkl}$). In addition, the beam centre and sample to detector distance may be calculated[434,440], the wavelength ($\lambda = 2d\sin\theta$) and/or wavelength spread ($\Delta\lambda/\lambda$) verified and other corrections determined such as detector tilt, beam geometry smearing effects and pixel resolution (that is, Δq per pixel as a function of q). Whenever the incident λ or sample to detector distance changes, the q axis must be re-evaluated. **c** | One method to convert $I(q)$ measured in arbitrary units (a.u.) into an absolute scale (inverse centimetres) is achieved by measuring a standard sample with known scattering properties, in this example, water. Two single-angle X-ray scattering (SAXS) profiles are measured using identical experimental conditions (sample thickness, exposure time, X-ray wavelength and so on): water in a sample container, and the empty container. Empty cell scattering contributions are subtracted to obtain the $I(q)$ profile of water. The magnitude of water scattering recorded on the detector is calculated (magnitude of the black dashed line) to obtain the water scattering in arbitrary instrument units. This arbitrary value is compared with the known standard $I(0)$ of water at the given experimental temperature. The resulting scale factor is calculated and applied to all scattering intensities to obtain $I(q)$ in inverse centimetres.

distance is altered. Primary beam intensity is obtained using intensity monitors, placed before and after the sample to allow for the quantification of the sample transmission of the incident beam that is proportionate to the sample absorption.

Various data correction procedures have been developed[58,168–171]. Instrument control and data reduction software generally apply the required corrections for sample transmission, thickness, beam geometry, wavelength, q-axis calibration, $I(q)$ calibration, beam stop position and detector artefacts automatically to all data[172–175]. It should be noted that weaker sample scattering will require more careful correction of the data[176] as scattering intensities become similar in magnitude to the inherent and unavoidable background scattering from the instrument, for example that caused by the optical components of the beam line. Instrument background corrections for a strongly scattering solid sample with high contrast, such as porous rock, may have a lower impact on the SAS profile than corrections required for, for example, a dilute protein in solution in a capillary. When using SANS over SAXS, additional and more complicated corrections are required, often arising from neutron beam properties[177] such as beam size, neutron guide and aperture geometry, sample to detector positions, the neutron wavelength distribution and the ToF, if using multi-wavelength neutron applications. GISAS geometry(s) necessitates careful evaluation of each 2D image measured at different tilt angles principally because both the in plane and the out of plane components of the scattering are additionally affected by the tilt angle-dependent 'warping' of the intensities with the refraction of the incident beam and the different types of surface scattering event (FIG. 1d). Advanced algorithms are required to disentangle sets of experimental 2D images that take into account these modulations to obtain the final 'unwarped' 2D scattering of the sample[178,179].

The process of detecting scattering events and then placing $I(q)$ versus q profiles within a standard frame of reference is fundamental for data interpretation. Modern X-ray detectors achieve these steps through built-in software run directly in application-specific integrated circuits[180]. Two detector types dominate current SAXS devices: scintillator-based charge-coupled devices, for example Rayonix, and pixel-array detectors such as Dectris Eiger, Pilatus[181] or Rigaku HyPix[182]. Both detector types can detect millions of photons per pixel per second, with pixel sizes in the range of 50–200 μm^2, low electronic noise and consistent pixel to pixel energy thresholds (the response of each individual pixel to a particular X-ray wavelength). Because SAS intensities may decay several orders of magnitude over a given q range, pixels must possess a high dynamic range (the ability to accurately measure both extremely high and extremely low intensities) while maintaining a linear response between the number of photons detected and the output signal to ensure that the recorded signal from the detector corresponds to the number of photons counted. For SANS, ^{3}He or boron-based[183] detectors are mainly used with pixel sizes in the millimetre to centimetre range. The size of beam, detector pixel size, energy-detection threshold and maximum q range that can be measured all contribute to a SAS instrument's performance.

Detectors are not perfect and require many corrections to account for deviations in the energy-dependent linear pixel response, to consider threshold sensitivity (flat fielding[184]) and to remove contributions from dead or hot pixels. We refer readers to REF.[58] for an excellent review by Pauw of necessary detector and other corrections. For charge-coupled device detectors, corrections for thermal fluctuations and read-out noise, also known as dark current corrections, and the detection and removal of 'zingers' — noise caused by cosmic rays or natural radioactive decay — may be necessary. As most detectors used for SAS are flat and the scattering wavefront emanating from the sample is a virtual sphere, spherical corrections become increasingly important at higher scattering angles or at smaller distances between the sample and the detector.

Absolute calibration of scattering intensities (FIG. 4c) significantly increases the value of SAS data. When $I(q)$ is placed on an absolute scale (inverse centimetre), quantitative information about the volume of particles, scattering length densities, contrasts, absolute specific surface areas and molecular weights can be evaluated using a scaled frame of reference for length, area and volume that directly relates to the length, area and volume scale of the sample. Absolute scaled data thus provide a quantifiable link between the experimental $I(q)$ and the physical dimensions of the sample, and absolute scaled data are comparable with experiments performed on different instruments across different facilities using different configurations. Absolute calibration is performed using a standard with known scattering properties such as pure water or glassy carbon, or using known instrument or device transmission geometry parameters[176,185–190]. The advantage of routinely using a documented absolute intensity standard, such as, for example, the glassy carbon-based NIST Standard Reference Material 3600 (NIST SRM3600)[190], is that one can quickly verify performance of the instrument and also trace the calibrated experimental scattering intensities back to the original verified standard.

Sample environments

Sample environments for SAXS and SANS span those associated with generic forms of sample delivery to those in specifically engineered and tailored devices that may include the integration of additional analytical probes such as lasers, spectrometers and magnets[191]. Sample environments include gel, paste or powder sample cells, in which samples are loaded between two low-background scattering/absorption windows or mounted on a grid support and held in the beam. The sample holder may be placed on a moveable x–y stage so that the sample can be systematically scanned at different coordinate positions to account for internal orientational bias, for example when probing differences in anisotropic scattering through a material[88,192,193]. The incorporation of pressure[194], shear[195,196], stretch or high-temperature sample cells is routine for both hard-matter and soft-matter samples, and these cells can be used to suit an instrument's parameters and capabilities; for example,

magnetorheological SANS set-ups for the analysis of complex magnetic fluids under shear flow and a magnetic field[197].

Temperature-controlled capillaries or cuvettes are generic sample holders for solution-based samples in transmission geometry and are constructed from materials with low intrinsic background scattering and absorption properties, such as quartz. The solution sample may be held in the capillary, or delivered to the beam under continuous flow that refreshes the sample being exposed and helps limit the effects of radiation damage and is, thus, particularly useful in SAXS[198]. The use of continuous flow size-exclusion chromatography (SEC)[199–202] or ion-exchange chromatography[203,204] is becoming increasingly popular for the separation of individual components within sample mixtures; in these techniques, sample components are separated on a column matrix where the separation is based on particle size for SEC and differences in charge for ion-exchange chromatography. Separated components for SEC–SAXS or SEC–SANS are delivered from the column to the beam line in a continuous flow, enabling the sequential analysis of the separated sample component's scattering profiles. Additional laser light scattering such as multi-angle laser light scattering or dynamic light scattering, spectrophotometers and refractometers may be integrated into the flow stream to provide additional quantification of the molecular weights and concentrations of the separated components and to assess the effectiveness of the separation step[205].

The incorporation of time-resolved measurements to quantify structural changes is readily achievable using SAS. The microsecond to millisecond timescale is routinely accessible using SAXS owing to the use of modern synchrotron radiation sources and fast frame-rate detectors. For SANS, minute timescales are typically achievable, with more recent and significant advances allowing measurements on a sub-millisecond scale. The key to time-resolved experiments is the delivery of a triggering mechanism to effect a change of state and the subsequent measurement and accurate timing of this state change. Triggering mechanisms for SAXS may include lasers for photosensitive reactions[206], pressure changes[207] or, more often, the controlled mixing and delivery of sample components. Mixing as a triggering mechanism can also be used for SANS[208–210], in addition to the application of an externally controlled magnetic field applied to the sample position[153].

There are two main experimental set-ups for time-resolved solution sample experiments: stop and flow time-resolved (SF-TR) and continuous flow time-resolved scattering experiments. In the SF-TR approach[211], a stop and flow device controls component injection through a mixing chamber and delivers the mixed sample to a capillary, at which point the flow is stopped and the SAS profile measured. The time limit of stop and flow devices and the sample consumption — which may be hundreds of microlitres to a millilitre over the course of an experiment — is dictated by the internal tubing length of the stop and flow device and the minimum time it takes for the sample to reach the point of measurement from the mixing chamber (also known as the dead time, typically a few milliseconds). Each time point of the reaction is assessed by systematically increasing the delay time of the measurements from the minimum dead time of the stop and flow device, up to several seconds or minutes, before exposing the mixed sample to the beam. It may also be possible to monitor the progression of a reaction during the course of exposure at each time point where the data are recorded as set of individual high frame-rate images. For SF-TR SAXS, as the measurements are performed when the sample is stopped in the beam, the sets of scattering profiles need be carefully evaluated to ensure that any observed changes in the scattering are ascribed to the mixing trigger and not caused by X-ray-induced damage.

Continuous flow time-resolved experiments[105] are similar, in principle, to SF-TR measurements but instead of stopping the flow after mixing, the sample components are mixed and passed quickly through the beam line. By calibrating the dead time and altering this time by changing the tubing length, changing flow rates or simply shifting the beam to a different position along the flow path, it is possible to monitor the reaction of a continuously refreshing sample caught at a particular time point after the mixing process. This approach can access microsecond to picosecond timescales of a reaction[107] and does not require a high frame-rate detector. A further advantage of this system is that using a continuous flow reduces the effects of radiation damage to the sample, which is particular useful for SAXS.

Safety and ethical considerations

All large-scale SAXS and SANS facilities adhere to high levels of safety by following the as low as reasonably achievable (ALARA) principles to ensure minimal exposure to radiation sources. This includes installing physical barriers such as lead or concrete shielding around the source and instruments, maintaining physical distance, minimizing interaction time with the instrument and sample, monitoring radiation and undertaking compulsory safety training. For SANS, it is especially important that all components that have been exposed to the neutron beam are measured for signs of activation. Any spills must be contained using measures dictated by on-site radiation safety and protection specialists. For biological and chemical samples, the requisite safety protocols must be adhered to; for example, understanding of biological and chemical risk categories and their sanctioned waste disposal procedures. The nature of the components of a sample must be disclosed to health and safety officers and those responsible for on-site laboratories and any beam-line staff.

Beam time at large-scale facilities is publicly funded and comes with a high operational and infrastructure cost. Consequently, beam time is typically awarded based on the independent evaluation and merit of scientific proposals. It is poor form to secretly measure samples that are not disclosed for both safety and ethical reasons. When shipping samples, the safety protocols of the facility where the measurement takes place should be considered specifically to ensure that any shipped samples fall within the health and safety guidelines of the facility.

Results

The raw results of any SAS experiment are a set of images where the active pixels of the image represent the count of X-ray or neutron scattering events. Below, we describe how to place image data in the context of both a standardized $I(q)$ and q frame of reference, taking into account the instrument set-up. An approach to the interpretation of SAS data measured from solution samples that produce isotropic scattering is also described.

Data and processing

Modern SAXS and SANS instruments typically collect scattering data as a set of 2D images on a detector. After detector corrections and calibration of the q axis have been applied (FIG. 4a,b), the intensity data on the 2D images recorded in transmission geometry are analysed in terms of q and the rotation angle, φ, around the beam centre coordinates. For anisotropic scattering, the 2D images may be further subdivided into limited φ-angle wedges, for example when measuring the scattering from oriented or ordered samples such as fibres and nematic phases[212]. For GISAS, 2D data are analysed in terms of the DWBA (FIG. 1d) and the simulation of 2D data from models[50,213–216]. See BOX 2 for common terms relating to SAS data analysis such as azimuthal averaging, the Porod volume, V_p, the Guinier behaviour, the Hankel transformation, volume-element bead modelling and principal component analysis and singular value decomposition.

A common simplified approach for data reduction in transmission geometry is shown in FIG. 5. The 2D data from the sample and the matched solvent, measured over a selected time interval, are first azimuthally averaged around a given φ to generate 1D scattering profiles. A large fraction of SAS is done on isotropic systems, in which case the azimuthal averaging occurs for each point in q, maximizing the φ available on the detector (FIG. 5a). However, a significant fraction of the microstructures of interest generate anisotropic scattering patterns, caused by biased structural orientations within the sample — for example, oriented fibres[217], polymers[218], coatings, nanocomposites[219], nanocrystalline assemblies[220] and nanoparticles[221]. In these cases, the scattering by the sample varies with the direction of a scattering vector in 3D. This typically results in a 2D image where the intensity at a given q also varies with φ on the detector (FIG. 5b). The analysis of anisotropic data is beyond the scope of this Primer[222,223], but in simple terms it is often necessary to probe the type of microstructured anisotropy within the sample by measuring it carefully in different orientations. In correctly selected orientations, the 2D intensity profile $I(q,\varphi)$ can fully represent the 3D scattering from the sample. An appropriate model of the microstructure then needs to be developed using modelling tools such as sasView. There are two main approaches to the analysis of anisotropic data; either the 2D data are reduced in terms of azimuthally averaging the intensities through selected φ wedges on the detector, resulting in set of 1D $I(q,\varphi)$ curves, or some tools enable fitting the 2D data $I(q_x,q_y)$ directly.

The standard errors of $I(q)$, written as $\sigma I(q)$, are assessed through individual pixel counts, which follow Poisson statistics if recorded on a photon counting detector; in this case, the error of the intensities is given by the square root of the number of counts. The data are then normalized to the transmitted beam to take into account the absorption of the sample and the matched solvent background. Scattering from the solvent background is subtracted from the sample scattering to generate a 1D reduced and subtracted scattering profile. The standard error on the 1D data set can then be calculated using simple error propagation. Often, the intensity is considered as a scattering cross section and the data are preferentially placed on an absolute scale ($I(q)$, inverse centimetres). Alternatively, the intensities may be scaled to a known standard with the same

Box 2 | **Common terms in SAS data analysis**

Azimuthal averaging
The process of averaging quantities at points that occur at the same distance, r, relative to a shared common origin, O, through a given angle, φ. For example, and as occurs for the isotropic scattering case in transmission geometry (FIG. 1), averaging the scattering intensities recorded on a 2D detector around the circumference of a circle defined by a radius q from the beam centre. Refer to FIG. 7.

Porod volume
A volume determined from the inverse of the scattering invariant, Q, which is calculated from the integral of the normalized-scattering Kratky plot ($I(q)/I(0)q^2$ versus q) (FIG. 8c). For globular homogeneous bodies, the Porod volume, V_p, relates to the physical particle volume and may further be used to evaluate the molecular weight of monodisperse compact particles such as proteins in solution[499–501]. The Porod volume may be influenced by the scaling relationships between the particle volume, surface area and surface roughness, which influences the magnitude of the decay in the scattering intensities as a function of q at higher angles[231] (FIG. 8a).

Guinier behaviour
Small-angle scattering (SAS) intensities measured at low scattering angles that are dependent on the forward scattering and radius of gyration, R_g, of a particle (see Eq. 8 and FIG. 8a,b). The maximum extent of the Guinier region is often defined to a qR_g of 1.0 to 1.3, that on a Guinier plot ($\ln(I(q))$ versus q^2) generates a linear relationship for a pure, monodispersed and ideal particle sample absent from interparticle interactions.

Hankel transformation
A mathematical transformation that expresses a function in reciprocal (q space) as an integral over a function in real space weighted by so-called aspherical Bessel functions. This transformation is useful to represent and rapidly compute scattering amplitudes and intensities, $I(q)$, of a particle with a given structure and is utilized in the multiple representation of SAS (Eq. 14).

Volume-element bead modelling
The process of parameterizing a real-space model in three dimensions as a collection of smaller volumes, called volume elements, that describe the larger total volume of excess scattering length density (for example, in the case of a volume packed with a set of dummy atom beads). The small volume elements are ascribed a phase identity with a relative scattering length (for example, a 'particle phase' and a 'solvent phase'). As both the position and the phase of the small volume elements are always known, the scattering profile from the total occupied volume may be readily calculated. During modelling, the 'phases' of these volume elements are allowed to interconvert based on minimization routines guided by the fit of the model to the SAS data (such that the bead phases are allowed to swap identity between 'particle phase' and 'solvent phase'). A point is eventually reached where the combined volume elements of the particle phase become fixed in space and fits the SAS data, and thus represents the real-space volume and shape of the excess scattering length density (see FIG. 10a).

Principal component analysis and singular value decomposition
Mathematical approaches allowing one to assess the number of significant components required to describe multiple sets of data by their linear combination. In SAS, these approaches are employed to analyse scattering from collected mixtures of different particles or different states at varying conditions to determine what the theoretical minimum number of states required to adequately describe the whole set of data.

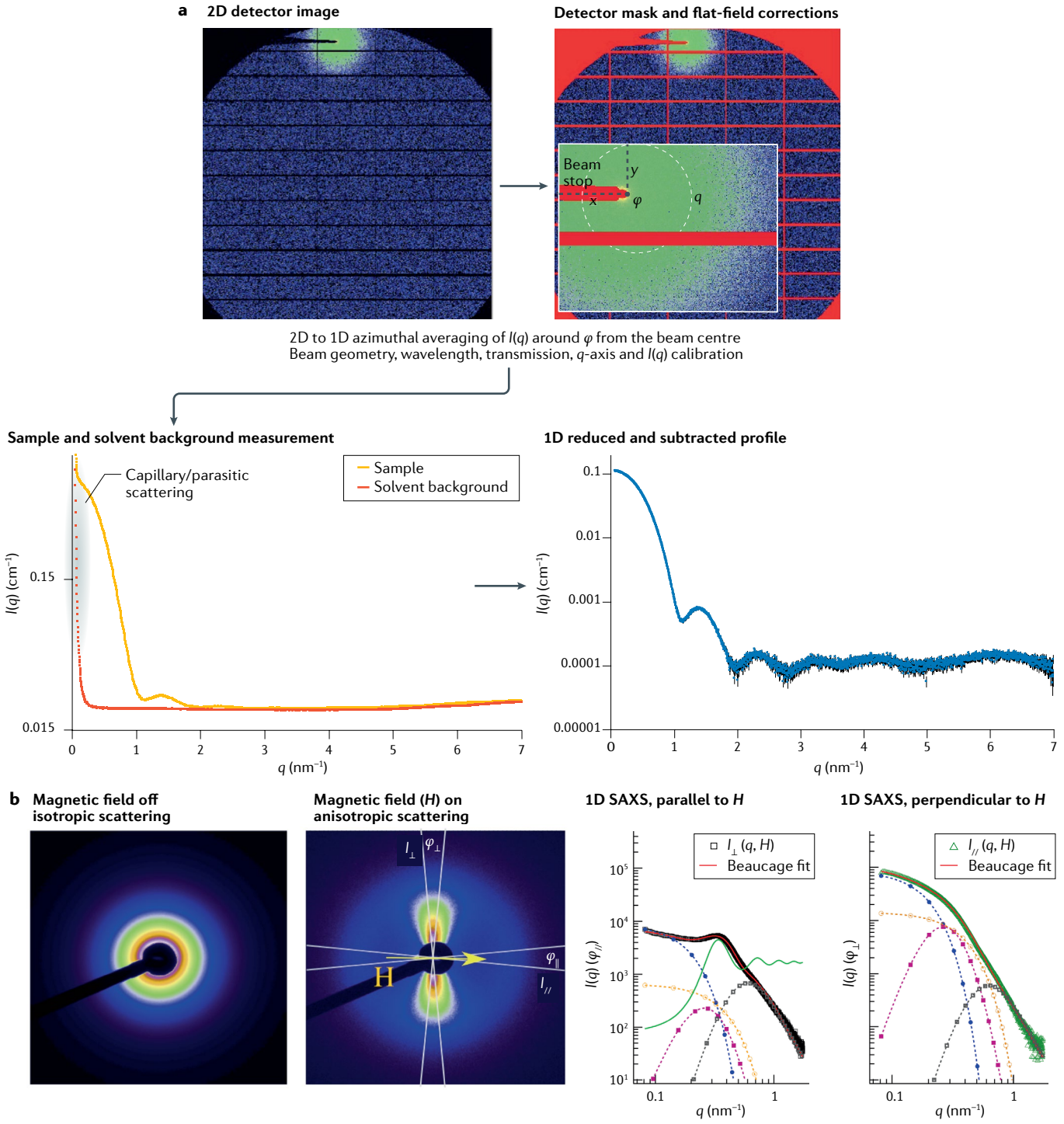

or similar contrast and partial specific volume as the sample, for example for proteins in solution[59,224]. If the isotropic scattering data were measured from a non-point source (FIG. 6a), beam geometry corrections can be applied (FIG. 6b,c).

For SAXS and SANS, the data can be normalized to the sample concentration to assess concentration-dependent effects in the sample, such as interparticle interactions, and merged if recorded from different detector positions (FIG. 7a–c). For anisotropic scattering samples, additional beam geometry and detector position corrections are required, for example when merging USAXS and SAXS data[225].

In general, a reduced experimental scattering profile captures the following terms:

$$I_{s,0}(q) = \frac{I_{s,m}(q)}{t_s \phi_s T_s d_s} - \frac{I_{b,m}(q)}{t_b \phi_b T_b d_b} - \left(\frac{1}{\phi_s T_s d_s} - \frac{1}{\phi_b T_b d_b} \right) I_{noise}(q). \quad (5)$$

Fig. 5 | **Basic scheme for data reduction. a** | Data are recorded on a 2D detector, in this case small-angle X-ray scattering (SAXS) data recorded on a Dectris Pilatus 6M. Regions such as 'hot pixels', inter-module detector gaps and the beam stop are masked out (for example, using FIT2D (REF.[434])). If necessary, additional flat-field corrections are applied to the image (for example, to take into account pixel sensitivity). The *x*,*y* pixel coordinates of the beam centre are defined and *q*-axis scaling is applied. For isotropic scattering, azimuthal averaging of $I(q)$ recorded at each q is performed around the beam centre coordinates (maximizing rotation angle, φ, for each q), ignoring the masked areas, and a subsequent reduced 1D scattering profile is generated. Additional corrections to the intensities are applied, for example the data are scaled to the transmitted beam to take into account sample absorption; the intensities are placed on an absolute scale (inverse centimetres), or normalized to a unit exposure time or sample concentration. For samples in solution, such as macromolecules or polymers, the scattering from an exactly matched solvent blank is also measured, preferably in the same sample capillary and instrument configuration, and then the 1D solvent scattering profile is subtracted from the sample scattering to generate the reduced and background-subtracted $I(q)$ data representing the scattering from macromolecules in the sample. **b** | Example of an isotropic to anisotropic scattering transition in a colloidal ferrofluid (manganese ferrite core–shell $MnFe_2O_{4+\delta}$@γ-Fe_2O_3 particles) caused by the application of an external magnetic field, H. With the field off, the particles are randomly oriented within the sample and generate isotropic scattering and are analysed as described in part **a**. When the magnetic field is switched on, anisotropic scattering is produced caused by the field-induced alignment of the ferrofluid particles within the suspension. In this case, the anisotropic scattering data may be analysed (right) in terms of narrower range of azimuthal φ wedges, for example along the principle orientation axes, to generate 1D scattering profiles parallel ($I(q), \varphi_{//}$) or perpendicular ($I(q), \varphi_{\perp}$) to the direction of the magnetic field[493]. The resulting 1D scattering profiles may be modelled as a set of components (dotted lines; 'Beaucage fit'[222,223]) taking into account Guinier and Porod behaviours, structure factors, polydispersity, cluster orientations and mean distances between particles both parallel and perpendicular to the magnetic field. Part **b** is adapted from REF.[493], CC BY 4.0 (https://creativecommons.org/licenses/by/4.0/).

Here, $I_{i,\mathrm{m}}(q)$ is the measured intensity for the sample ($i = \mathrm{s}$) or background ($i = \mathrm{b}$) and t_i, ϕ_i, T_i and d_i are the acquisition time, average incident flux during acquisition, sample transmission and sample thickness, respectively. The last term corrects for background, which is proportional to acquisition time and not to incident flux, and $I_{\mathrm{noise}}(q)$ is measured with the beam blocked at the sample position normalized by the time of the measurement. For dilute solutions, the last term is often very small. The errors on $I_{\mathrm{s},0}(q)$ can be calculated by simple error propagation. The data are usually provided in the form of 1D data files with error bars propagated from the original counting statistics on the detector. There are diverse approaches to data reduction and processing that span fully automated, on-the-fly data reduction strategies to manual interventions aided by data processing software. Automated data pipelines for SAXS[85,173] applied to the analysis of dilute macromolecules have several advantages, including on-the-spot detection of radiation damage during the course of X-ray exposure and the additional extraction of structural parameters such as R_{g}, D_{max}, $p(r)$ profiles and molecular weight, which provide near-immediate feedback on the structure of the sample after the scattering contributions from the solvent have been subtracted. Systematic differences in the structural parameters, for example those observed through a concentration series, can be quickly assessed, and sample or data collection conditions adjusted accordingly. Common data reduction programs are listed in TABLE 1 and additional tools and details can be found, for example, at the SAS Portal.

Analysis of data from solution samples

The approaches for analysing data from isotropic scattering systems such as particle suspensions, macromolecules and polymers in solution (FIG. 8a) have been well reviewed[8,60,226]. The initial analysis steps involve simple data transforms, for example generating Guinier plots at very low angles ($\ln I(q)$ versus q^2 for $qR_{\mathrm{g}} < 1.3$)[51] (FIG. 8b), Kratky plots ($I(q)q^2$ versus q) (FIG. 8c) and Porod–Debye plots ($I(q)q^4$ versus q or q^4)[4,227]. This is followed by the estimation of R_{g}, $I(0)$ and scattering invariants, associated Porod volume and scaling behaviours from the data. The steps above give insight into the scattering length density bounded volume, its size and shape weighting within this volume, and mass and surface fractal dimensions, for example compact or globular, flat, hollow, disordered or rod-like[4,228–232]. A key step is to convert the scattering intensities into a real-space representation by calculating the $p(r)$ function, or pairwise distance distribution (FIG. 8d). This function is a frequency histogram of real-space distances between pairwise volume elements, weighted by the scattering length density. For dilute, non-interacting and isotropic systems, the scattering intensity (Eq. 1) can be written as:

$$I(q) = 4\pi \int_0^{D_{\mathrm{max}}} p(r) \frac{\sin qr}{qr} \mathrm{d}r. \qquad (6)$$

This equation can formally be inverted, but in practice is solved by regularized indirect inversion methods[1,233,234] to yield $p(r)$. The procedure automatically extrapolates to $q = 0$ and gives the intensity value as $I(0) = 4\pi \int_0^{D_{\mathrm{max}}} p(r)\mathrm{d}r$ and the radius of gyration as $R_{\mathrm{g}}^2 = \int_0^{D_{\mathrm{max}}} r^2 p(r)\mathrm{d}r / [2\int_0^{D_{\mathrm{max}}} p(r)\mathrm{d}r]$. For samples where the contrast and partial specific volume are known or can be calculated[63] and the concentration has been determined, the absolute scaled $I(0)$ can be used to determine the volume or the mass, M, of the particles[59,224].

For centrosymmetrical particles such as spheres, cylinders and planar particles, $p(r)$ can be deconvolved into a radial excess scattering length profile, $\Delta\rho(\mathbf{r})$[235,236]. Alternatively, $\Delta\rho(\mathbf{r})$ can be obtained by fitting its Fourier transform squared directly to the data[237]. Both of these approaches involve regularization.

Another common way of analysing data from particle suspensions is to fit models such as analytical or geometric models to the experimental intensity, where the model form factors are calculated and then compared with the data. These models are usually expressed in terms of form, $P(q)$, and structure, $S(q)$, factors as shown in the Introduction. The models depend on some structural parameters that are optimized when the models are fitted to the experimental data. The form factor can be, for example, that of a homogeneous sphere with radius R[238]:

$$P(q) = \left[\frac{3(\sin qR - qR\cos qR)}{(qR)^3}\right]^2. \qquad (7)$$

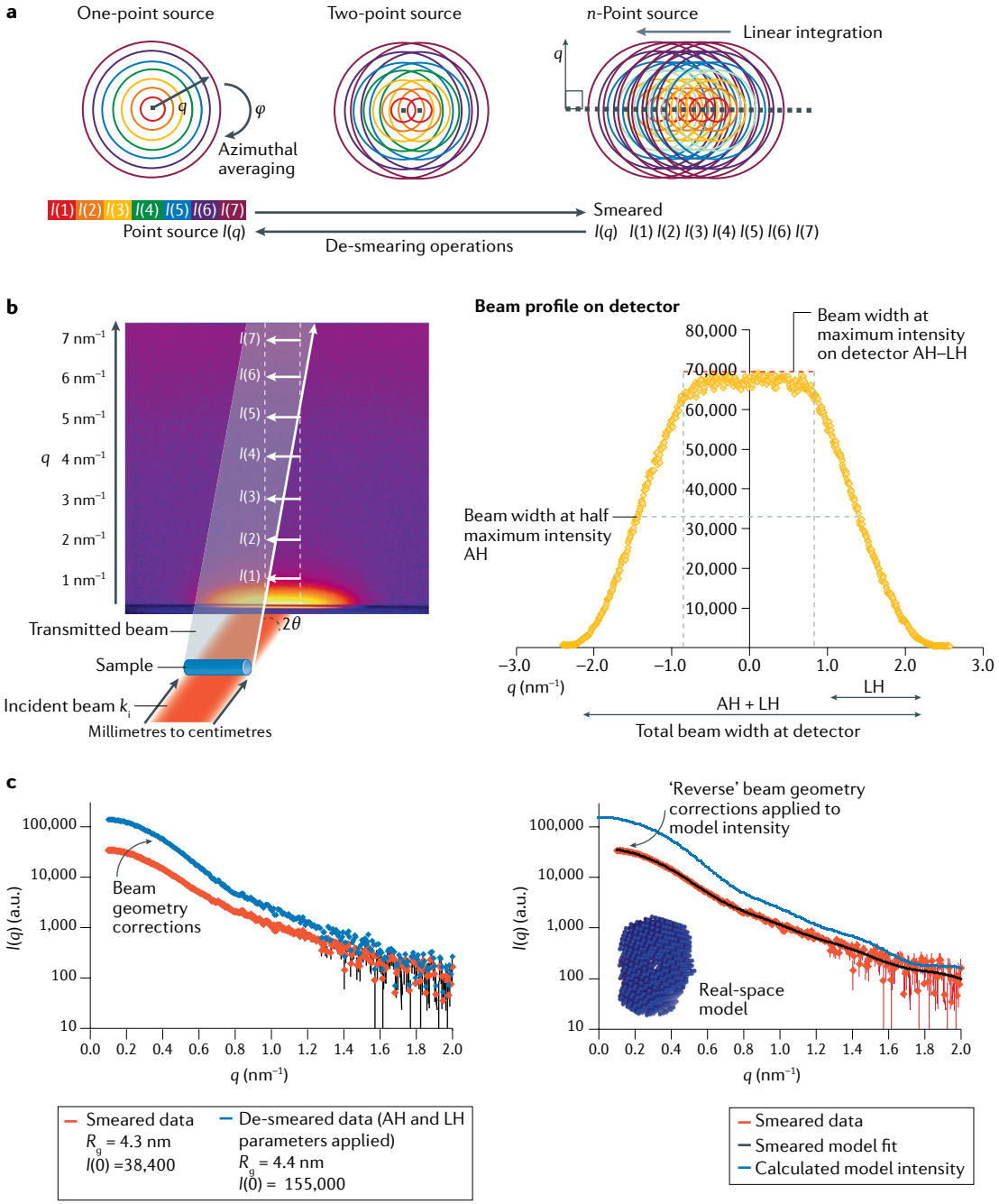

Fig. 6 | **Example of beam geometry correction — slit smearing. a** | For isotropic small-angle scattering (SAS) data measured using a point source, the $I(q)$ measured relative to the beam centre at any given q vector around the azimuthal angle φ is independent, resulting in direct correspondence between $I(q)$ measured for each value of q in two dimensions. If two point source beams are used, $I(q)$ from one point source begins to add at the intersection of the slightly shifted q frame of reference of the next door neighbour. As the number of neighbouring point source increases, and ultimately tends to infinity, that is, a line collimated instrument, the only common q frame of reference along the line of point sources becomes that perpendicular to the line, where the $I(q)$ intensities become smeared together. **b** | 2D to 1D data reduction using a line source instrument requires linear integration of the smeared scattering intensities across the detector parallel to the incident beam, perpendicular to the vertical q axis. The geometry of the measured beam profile is that of a trapezoid, the widths of which depend on the length of the slit used for the collimation. Trapezoidal parameters AH and LH provide a measure of the magnitude of the smearing effect on the data and are used to correct for the smearing effect of the incident beam geometry. **c** | Either smeared data are corrected for the beam geometry, providing a de-smeared scattering profile, or, alternatively, real-space models are developed and their calculated scattering profiles are corrected for the beam geometry and compared with the smeared data.

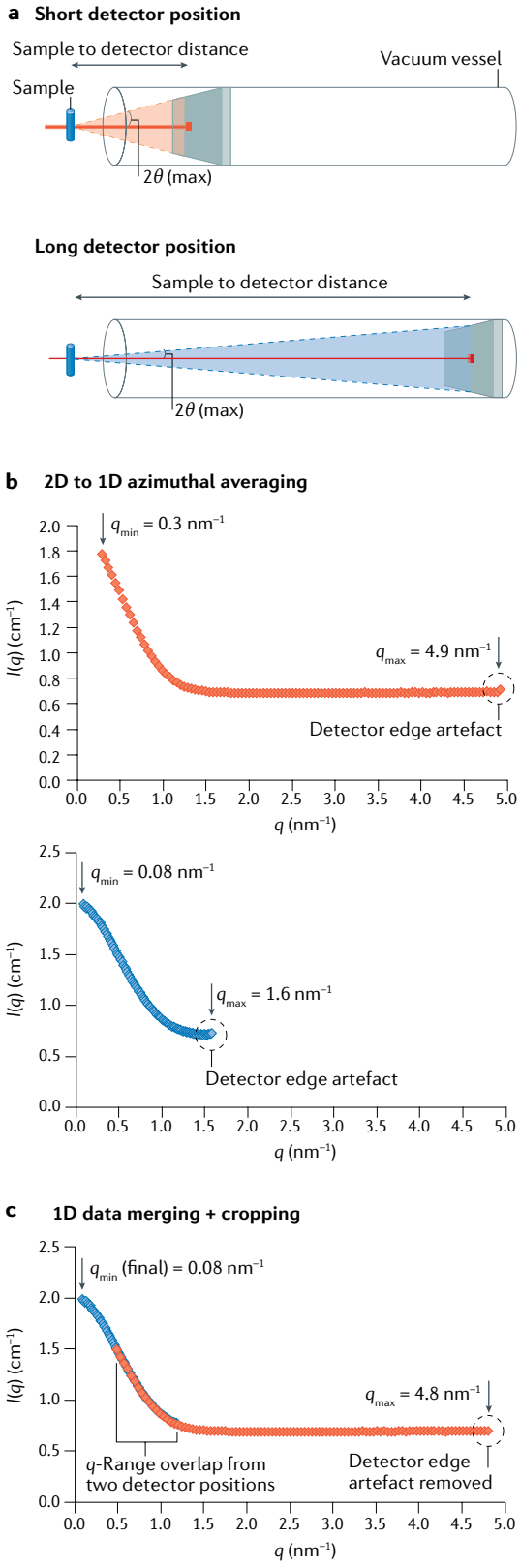

Fig. 7 | **Data merging. a** | To extend the experimental q range, small-angle scattering (SAS) data may be measured at multiple detector positions. Shorter detector positions record data to higher angle and vice versa. **b** | Azimuthal averaged data from the detector positions are generated, each with a respective q_{min} and q_{max} and a common q-range overlap. **c** | Data are scaled and merged together using the q-overlap region from the two detector positions as a frame of reference to produce the final SAS profile over the extended q range.

This function approaches unity for very low values of q where the Guinier behaviour is observed as $q \to 0$[51]:

$$P(q) \approx \exp\left(-\frac{(qR_g)^2}{3}\right). \quad (8)$$

In this equation, $R_g = \sqrt{\frac{3}{5}}R$ represents the radius of gyration of the sphere. At large angles, the scattering decays strongly and follows, on average, the Porod behaviour[227]:

$$P(q) \approx \frac{9}{2}(qR)^{-4}. \quad (9)$$

The fits of the models to the experimental data are performed using a weighted least squares method[239,240]:

$$\chi^2 = \frac{1}{N-p}\sum_{i=1}^{N}\frac{(I_{meas}(q_i) - I_{model}(q_i))^2}{\sigma_i^2}. \quad (10)$$

The reduced χ^2 functional is minimized to get the best agreement between the model, $I_{model}(q_i)$, and the measured data, $I_{meas}(q_i)$. In this expression, σ_i are the standard errors of the measured intensities, N is the number of data points and p is the number of parameters in the model, which are optimized during the fit. A satisfactory fit to the data, and assuming that the errors of the intensities have been correctly specified through the data reduction procedure, gives $\chi^2 = 1$, meaning on average the deviation in the model is equal to the standard error of the data points. Note that if there are too many points at high q values with large errors (oversampling), χ^2 can be <1 even if the fit has systematic deviations from the data. In such cases, re-binning the data may be required so that the data points more properly represent the information content of the data set[241]. Systematic deviations are often examined by plotting $(I_{meas}(q_i) - I_{model}(q_i))/\sigma_i$ against q and looking for sequences of data points with positive and negative deviations, respectively[242]. Note that standard procedures for optimizing χ^2 also provide standard errors in the fit parameters. If the parameters of the model are highly correlated, the errors can be estimated by Monte Carlo-based methods[243].

Sometimes, the measured data are significantly smeared by the instrument owing to the beam geometry, detector resolution and wavelength spread. For neutrons, this is nearly always the case and needs to be considered in the calculation of theoretical or model intensities. The distribution of q contributing to the signal, when the instrument setting is q, can be described by the resolution function $R(q,q)$. With this, the intensity is:

$$I(q) = \int_0^\infty R(q,q)I_{model}(q)\mathrm{d}q. \quad (11)$$

Table 1 | **Image, data reduction and analysis tools**

Software	Application	Image and/or data reduction	Data analysis and modelling	Ref.
ATSAS	SAS/bioSAS	✓	✓	Available online and for download; Franke et al., 2017 (REF.[427])
AXES	bioSAXS	–	✓	Available online; Grishaev et al., 2010 (REF.[428])
BioXTAS RAW	bioSAXS	✓	✓	Available to download; Hopkins et al., 2017 (REF.[429])
CCP-SAS & SASSIE-Web	SAS	–	✓	Available online; Perkins et al., 2016 (REF.[430])
BornAgain	GISAS	–	✓	Available to download; Pospelov et al., 2020 (REF.[216])
D+	SAXS	–	✓	Available to download; Ginsburg et al., 2019 (REF.[431])
DAWN	SAXS	✓	–	Available to download; Filik et al., 2017 (REF.[432])
DPDAK	SAXS/ GISAXS	✓	–	Available to download; Benecke et al., 2014 (REF.[433])
ESRF SAXS Programs	SAXS	✓	–	Available to download; Narayanan et al., 2018 (REF.[104])
FIT2D	SAS	✓	–	Available to download; Hammersley, 2016 (REF.[434])
fitGISAXS	GISAXS	–	✓	Babonneau, 2010 (REF.[213])
FoxS	SAXS	–	✓	Available online; Schneidman-Duhovny et al., 2016 (REF.[273])
GRASP	SANS	✓	–	Available to download; Dewhurst 2003 (REF.[435])
GIFT	SAS	–	✓	Bergmann et al., 2000 (REF.[436])
GIXSGUI	GISAXS	✓	–	Available to download; Jiang, 2015 (REF.[437])
HiPGISAXS	GISAXS	–	✓	Available to download; Chourou et al., 2013 (REF.[214])
IMAGEJ	SAS/GISAS	✓	–	Available to download
IRENA	SAS	–	✓	Available to download; Ilavsky and Jemian, 2009 (REF.[438])
IsGISAXS	GISAXS	–	✓	Available to download; Lazzari, 2002 (REF.[215])
Mantid	SANS	✓	–	Available to download; Arnold et al., 2014 (REF.[439])
NIKA	SAS/GISAS	✓	–	Available to download; Ilavsky, 2012 (REF.[440])
NIST software package	SANS/ ultra-SANS	✓	✓	Available to download; Kline, 2006 (REF.[441])
Pepsi-SAXS	SAXS	–	✓	Available to download; Grudinin et al., 2017 (REF.[270])
ScÅtter	SAXS	–	✓	Available to download
SCATTER	SAXS	✓	✓	Available to download; Förster et al., 2010 (REF.[442])
SASfit	SAS	–	✓	Available to download; Breßler et al., 2015 (REF.[443])
sasPDF	SAS	–	✓	Liu et al., 2020 (REF.[444])
sasView	SAS	✓	✓	Available to download
SAXSquant	SAXS	✓	–	Anton Paar
US-SOMO	SAXS	–	✓	Brookes and Rocco (REF.[398,445])
WAXSiS	SAXS	–	✓	Available online; Knight and Hub, 2015[446])
WillItFit	SAS	–	✓	Pedersen et al., 2013[300])

GISAS, grazing incidence small-angle scattering; GISAXS, grazing incidence small-angle X-ray scattering; SANS, small-angle neutron scattering; SAS, small-angle scattering; SAXS, small-angle X-ray scattering.

Core–shell and multiple-shell particles
Particles consisting of contiguous but spatially distinct layered regions of different average scattering length density. For example, a detergent micelle that in water forms an external layer of higher electron density (the hydrophilic heads) surrounded by a less electron-dense core (the hydrophobic tails).

The resolution function can either be measured or calculated[169,244].

The form factors of numerous geometrical models have been calculated and can be used for modelling SAS data[239,240]. These also include form factors of core–shell and multiple-shell particles. For systems consisting of dissolved and, perhaps, self-assembled molecules, knowledge of the molecular properties — partial specific volumes, scattering lengths and concentrations of the components — may be used to restrain the model. For example, for a micelle described by a core–shell model, the aggregation number can be used as a fitting parameter and the number density of micelles can be calculated as the mass concentration divided by the mass of a micelle calculated from the molecular mass and the aggregation number. The core volume is given

Polydispersity
Systems containing a distribution of sizes, or displaying a level of non-uniformity of structural states. For example, a monomer–dimer particle equilibrium (a mixture of different molecular weights) or disordered polymers (that may have the same molecular weight but, when viewed as a population, sample different conformations in solution).

by the aggregation number multiplied by the mass of the fraction of the lyophobic part of the molecule. If not spherical, additional parameters must be used for describing the shape of the core; for example, the axis ratio can be used for an ellipsoid. Note that the core is usually 'dry' and the scattering length density is known, whereas solvent molecules present in the lyophilic shell should be taken into account as these increase the shell volume and decrease its scattering length.

For some applications, the purpose is to determine the polydispersity of particles in the sample. This can be done by assuming a certain form for the size distribution

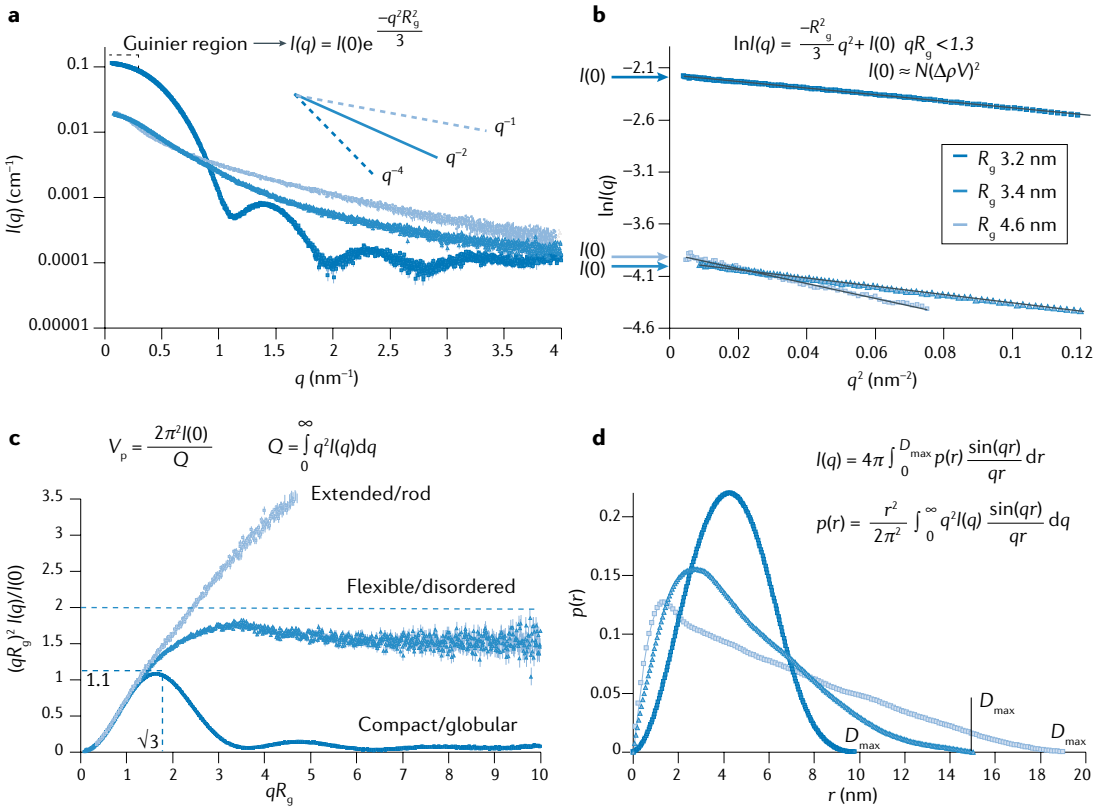

Fig. 8 | **Representative results. a** | 1D reduced and background-subtracted small-angle X-ray scattering (SAXS) profiles from three proteins in solution (dark blue, blue and light blue), normalized to protein concentration (milligrams per millilitre, or number density N) and time, and measured using approximately the same contrast, $\Delta\rho$, conditions. Scattering intensities that span the lower q values of the profiles may be approximated by the Guinier relation[51], where $I(q)$ is dependent on the contrast-weighted size and radius of gyration, R_g, of the proteins. The point where the scattering functions would cross $I(q)$ at $q = 0$, that is $I(0)$, relates to the volume squared of the particle. It is immediately apparent that the dark blue protein is much bigger than the blue and light blue proteins, which are both of a similar size. The rate at which the scattering data decays as a function of angle ($q^{-\xi}$, where ξ is the Porod exponent) relates to both the size and structure of the particles, in particular the scaling relationship between the scattering length density within the surface boundary of the particle volumes[4,231]. ξ decreases as the volume/surface ratios change, from more spherical compact ($\xi = 4$) to hyper-extended/rod-like ($\xi = 1$). **b** | Corresponding Guinier plots from the SAXS data. $I(0)$ can be obtained from the intercept whereas R_g can be derived from the negative slope of the plot. Although the dark blue protein has a significantly larger squared volume (and hence mass) than the other two proteins, the R_g is surprisingly similar to the blue protein (3.2 nm cf. 3.4 nm). Yet when comparing blue and light blue proteins that are of a similar size (similar $I(0)$), the R_g of the light blue protein is significantly bigger (4.6 nm). Guinier analysis and scattering data from part **a** already suggest significant differences in the scattering length density distributions of the three protein samples. For example, for a small protein to have a similar R_g to a large protein, the smaller one must sample more extended, non-globular states. **c** | Dimensionless Kratky plot of scattering data. The dark blue protein generates a plot typical of all compact globular structures, with a peak maximum at $I(\sqrt{3}) = 1.1$. The blue protein has properties of a highly flexible or intrinsically disordered system, with scattering nearing a plateau of 2 at higher values of qR_g. The light blue protein is a stiff-extended rod. This helps support the R_g results from the Guinier analysis. Relationships between the integral of a regular Kratky plot ($I(q)q^2$ versus q), known as the scattering invariant Q, and its relationship to the Porod volume, V_p (not to be confused with particle volume) are also displayed. **d** | Probable frequency of real-space distances, $p(r)$ profiles, calculated using indirect inverse Fourier transform methods[1,233,246,494–496]. In this instance, the $p(r)$ of the compact dark blue protein and of the rod-shaped light blue protein may be interpreted as the frequency of vector lengths internal to a single particle. Both samples are monodisperse and, as a result, there is an equal contribution to the $p(r)$ from each individual protein in the sample population. However, for the blue flexible protein, $p(r)$ does not represent the vector lengths internal to a single particle as the sample is structurally polydisperse (refer to part **c**). In this case, $p(r)$ represents the volume fraction-weighted contribution from each subpopulation in the ensemble of protein structural states. φ, rotation angle; D_{max}, maximum particle dimension; V, scattering volume.

Centrosymmetrical potentials
Energy potentials that are distributed symmetrically with respect to a central point.

(for example, Gaussian, Schulz or log-normal) and convolving it with the form factor for a shape that has to be assumed or known from observation, for example from microscopy imaging. Note that one cannot determine both size distribution and form factor at the same time as they are linked mathematically[245]. If the size distribution is not known, one can use regularized free-form methods for determining it[246,247]. Indirect Fourier transformation methods may also be employed to obtain the volume-weighted radius or particle size distributions from samples with varying degrees of polydispersity, for example those of nanoparticles, micelles and microemulsions[1,246,248,249].

When concentration effects are present in the SAS data, one can try to extrapolate the data to zero concentration using a Zimm approach[250,251]; however, it is sometimes necessary to include structure factors, $S(q)$, in the analysis. Analytical expressions for $S(q)$ that are easy to use in data fitting exist for some simple centrosymmetrical potentials, such as a hard-sphere potential, a screened Coulomb potential and a sticky hard-sphere potential[239,252–254]. The simplest is the hard-sphere potential, which only depends on the hard-sphere volume fraction and the hard-sphere interaction radius[255]. Similarly, if the particles aggregate and form clusters, this can also be included in the analysis by including a structure factor[49]. The typical aggregate structures are linear, random flight, fractal and compact clusters.

For polymers or particles with attached polymers, there are model expressions taking into account the many conformational degrees of freedom of such molecules. The simplest is that of a polymer chain obeying Gaussian statistics, which has the form factor[256]:

$$P(q) = \frac{2(\exp(-x) - 1 + x)}{x^2}, \quad (12)$$

where $x = q^2 R_g{}^2$ and $R_g{}^2$ is the ensemble-average square of R_g. There are a large number of analytical form factor expressions available for star and branched polymers with Gaussian chains and also for block copolymer micelle models with Gaussian chains[257–259] and semi-flexible chains[260]. Similar models exist for cases where the polymers are self-avoiding; however, the expressions are only numerical in these cases[259].

A classical tool to calculate form factors of complex structures is the Debye equation, which can be used for structures consisting of centrosymmetrical sub-particles (or atoms)[261]:

$$P(q) = \sum_{i,j=1}^{M} f_i(q) f_j(q) \frac{\sin\left(qd_{i,j}\right)}{qd_{i,j}}, \quad (13)$$

where $f_i(q)$ are amplitude factors of the sub-particles, $d_{i,j}$ is the distance between the centres of the ith and the jth particle, and M is the number of sub-particles. The amplitude factors represent a Fourier transform of the radial scattering length density profile. When the sub-particles are identical, their form can be taken outside the double sum, which simplifies the calculation.

An alternative representation of the form factor uses spherical harmonics introduced to SAS by Stuhrmann[54]:

$$\begin{aligned} I(q) &= \sum_{l=0}^{L} I_l(q) \\ &= 2\pi^2 \sum_{l=0}^{L} \sum_{m=-1}^{l} |A_{lm}(q)|^2, A(\boldsymbol{q}) \\ &= \sum_{l=0}^{L} \sum_{m=-1}^{l} A_{lm}(q) Y_{lm}(\Omega). \end{aligned} \quad (14)$$

Here, $Y_{lm}(\Omega)$ are angular functions defined on the surface of the unit sphere, $A_{lm}(q)$ are the multipole contributions to the scattering intensity and L defines the number of harmonics, which also represents the resolution. The functions $A_{lm}(q)$ are related by a Hankel transformation to radial functions in real space, which are computed from the $\Delta\rho(\mathbf{r})$ distribution. The spherical harmonics formalism allows for convenient representation and rapid computation of the scattering intensities, and this is used in many advanced analysis algorithms[262–268].

Computation of intensities from known structures is frequently used to screen available models against the experimental data. In biological applications, SAS is often computed from atomic-resolution structures, for example those deposited in the Protein Data Bank (PDB)[264,269–272]. However, for the calculation of the signal for a protein in solution, one needs to consider that only the excess scattering contributes. The excess scattering is usually obtained by subtracting the scattering of the displaced solvent, which is achieved by placing dummy Gaussian form factors on the position of the atoms so that the total volume matches that of the protein. Additionally, a well-defined layer of water molecules with an effective density higher than that of bulk water must be included in the calculations[271]. There are numerous programs publicly available for calculating SAS intensities in this way that provide a simple way of checking whether the solution structure is the same as the crystal, NMR or high-resolution cryo transmission electron microscopy structure. Methods are available to determine the oligomeric or domain structure by performing random searches[268,273,274]. Similarly, the structure of complexes of different proteins and nucleic acids can be determined when high-resolution structures of the constituent molecules are available. Restraints of connectivity and known distances between various amino acids or nucleotides can be included in the optimization as penalty functions added to the reduced χ^2, to make the models physically reasonable and to agree with other available data. It is also possible to complete high-resolution structures using hybrid methods, where the missing parts are represented by dummy residues. These model calculation and modelling programs are listed in TABLE 1 and online resources are provided in the Related Links.

Ab initio methods for SAS are applied for determining shapes when high-resolution models are not available[263,265,275]. The structures are optimized by Monte Carlo or genetic algorithm-based approaches with the inclusion of penalty functions that gives physically reasonable models. The shape determination methods do not give a

unique model, although the solutions are biased towards physically reasonable models. Therefore, it is usual to perform a series of, for example, 10–20 repetitions, and compare and analyse these to get the most representative model and assess the variation of the models[276]. Biological complexes with internal flexibility pose particular problems as the SAS data cannot be fitted with a single structure[262]. The ensemble optimized method[262,277] has been developed for analysing data from such systems. In this method, a large set of structures are first generated and then structures are selected by a genetic algorithm for finding a subset/ensemble of structures, which together can fit the data. Further analyses of these structures are made to identify the main classes of structures that contribute to the ensemble.

Applications

SAS may be used in and of itself as a stand-alone application to interrogate structures and changes in structures of materials. However, both SAXS and SANS can also be used in synergy with other methods and integrated into a diverse range of hybrid-methodological approaches such as combining high-resolution and low-resolution methods, spectroscopy, tomography, imaging, kinetics, thermodynamics, physical chemistry, molecular biology and so on. Here, we describe some general considerations when using SAS for structural investigations and its application to structural biology, soft matter and the hard-matter sciences.

General issues should be considered when thinking of SAS applications. These include the physical condition of the sample (liquid or solid, diluted or concentrated, macroscopically homogeneous or heterogeneous), whether outer influences may change the condition of the sample (temperature, pressure, oxidation), and whether structures in the sample change over time and at what rate. These and other considerations should guide the selection of appropriate sample environment and SAS set-up. A selection of contemporary SAS applications is outlined in TABLE 2 that demonstrates the utility of SAS for interrogating the structure, the organization and, in some cases, the evolving structural changes that occur in a wide variety of materials from biomolecules to polymers, gels, suspensions, microemulsions, surfactants, minerals, metals, clays, catalysts, nanoparticles, nanocrystallites, complex fluids and energy storage devices under a diverse array of sample environments spanning static measurements to shear, pressure, temperature, stretching and extrusion.

Four simulated transmission SAS results are shown in FIG. 9 to illustrate the scattering results for rod-like particles in different situations using a two-phase model. Here, the two different compounds are the surrounding matrix and nanometre-sized domains or particles. The domains can be single macromolecules, self-assembled molecules or other aggregates, colloids, atomic clusters, crystals, grains or pores in a material. Diluted scattering domains are independent from the position of their neighbouring domains and only scattering from the form factor $P(q)$ appears. Higher concentrations lead to packing of the domains, producing the additional structure factor $S(q)$. In the examples shown in FIG. 9, the cylinders have an aspect ratio of 1:5 and are either randomly distributed or oriented along the vertical axis. For oriented structures, the azimuthal distribution of the scattered intensity in the 2D pattern of the detector is not uniform, allowing the particle orientation in the sample to be determined.

Thin film layers, interfaces and buried structures close to surfaces are investigated using GISAS. GISAS can be also applied to liquids with a double-crystal deflector, where the beam is adjusted towards the sample surface, instead of tilting the sample surface towards the beam[278,279]. In addition, in situ structural investigations under grazing incidence may be performed in a multitude of controlled sample environments to assess time-resolved changes in vacuum, air or other atmospheres.

Structural biology

Determining the structures of biological macromolecules, such as proteins, polynucleotides, lipids and carbohydrates, and assessing their structural responses in the context of biological functions are necessary to understand life at the molecular level. SAXS and SANS investigations focus on extracting structural parameters such as R_g, D_{max}, $p(r)$ and molecular weight (FIG. 8) and developing models of biomacromolecules in solution (FIG. 10a). In the simplest case, a population of macromolecules or a complex is purified under dilute conditions (0.5–10 mg ml^{-1}) to minimize measurable interparticle interactions. When a sample is pure, homogeneous, monodisperse and non-interacting, the scattering intensities are proportional to the concentration, the squared product of the contrast and particle volume and $P(q)$ (Eq. 2). The background-corrected SAS profile therefore reflects the size, shape and structure of the macromolecules in the sample.

A key strength of SAS for structural biology is that structural changes in biological macromolecules can be quantified in response to changing the sample environment. Adjusting the pH, ionic strength, pressure[280,281], shear[282] and temperature gives access to a wide array of structural information that includes conformation and structural perturbations or changes in oligomeric and other association states that are increasingly being evaluated using time-resolved studies spanning the microsecond to second range[105,283–285]. The data are always measured from, and modelled in the context of, population states, and both SAXS and SANS are extremely sensitive towards detecting and quantifying the disposition of these populations. For example, if the oligomeric state of a macromolecule or complex is fixed as a stable population of monomers or dimers, and the conformational sampling of the population is very narrow, then the resulting scattering pattern from the sample may be interpreted in terms of a single particle in solution (be it as a stable monomer, dimer or a stable multicomponent complex or higher-order assembly). However, biological systems may not always adopt single-state populations. For example, proteins may self-associate into a mixture of oligomers or undergo spontaneous self-assembly over time via intermediates into a final equilibrium state. In addition, the conformational

Table 2 | **Selected SAS applications**

Experiment	Method	Application	Material	Ref.
Time-resolved	SAXS	Microfluidics, molecular folding	Protein	Graceffa et al., 2013 (REF.[105])
	SANS	Flow reactor, potentiometry	Surfactant	Hayward et al., 2018 (REF.[330])
	SAXS	Microfluidics, shear-induced phase	Block copolymer micelles	With et al., 2014 (REF.[447])
	SAXS	Stopped flow, phase transition	Microgel	Keidel et al., 2018 (REF.[331])
	USAXS	Thermal treatment, crystallization	Bulk polymer	Konishi et al., 2018 (REF.[448])
	GISAXS	Spin coating, laser interferometer	Block copolymer solution	Fleury et al., 2019 (REF.[449])
	SAXS	Thermal treatment, release kinetics	Silica-filled micelles	Mable et al., 2017 (REF.[450])
Temperature	SAXS/SANS	Phase diagram	Polymer microemulsion	Shim et al., 2019 (REF.[451])
	SAXS/WAXS	FTIR, melt crystallization	Bulk polymer	Tashiro and Yamamoto, 2019 (REF.[452])
	GISAXS	Heat zone annealing, orientation	Block copolymer	Samant et al., 2016 (REF.[453])
	GISAXS	Laser heating, self-assembly	Block copolymer	Yu et al., 2020 (REF.[454])
Flow	SANS	Microfluidics, orientation	Complex fluid	Lopez et al., 2015 (REF.[455])
	SAXS	Microfluidics, scanning	Protein fibrils	Lutz-Bueno et al., 2016 (REF.[88])
	GISAXS	Sorption, swelling	Hydrogel	Phillipp et al., 2015 (REF.[456])
Shear	SAXS	Oscillatory shear, coherent scattering	Self-healing hydrogel	Lin et al., 2019 (REF.[457])
	SAXS/WAXS	Flow-induced crystallization	Polymer solution	Dunderdale et al., 2020 (REF.[458])
Extrusion	SAXS	Hollow fibre spinning	Block copolymer solution	Sankhala et al., 2019 (REF.[332])
	SAXS	Micro liquid jet	Block copolymer solution, gold nanorods, silica	Schlenk et al., 2018 (REF.[459])
Stretch/strain	SAXS/WAXS	Uniaxial stretching, crystal orientation	Bulk polymer	Defebvin et al., 2016 (REF.[460])
	SAXS/WAXS	Uniaxial stretching, phase transition	Bulk polymer	Pepin et al., 2019 (REF.[461])
	SAXS/WAXS	Blown film	Bulk polymer	Zhao et al., 2018 (REF.[462])
Porosity	SAXS/SANS	CO_2 sequestration, oil exploration	Minerals	Cheshire et al., 2017 (REF.[463])
Precipitation	SANS	Ageing under heat treatment	Metals	Coakley et al., 2015 (REF.[464])
	SAXS/SANS	Alloy contrast variation, composition	Metals	Ohnuma et al., 2009 (REF.[353])
	SAXS/WAXS	Ageing kinetics	Metals	Zhang et al., 2016 (REF.[349])
Pressure	SAXS	Autoclave polymerization	Block copolymer	Alauhdin et al., 2019 (REF.[465])
	SANS	CD4 contrast matching, porosity	Minerals	Bahadur et al., 2016 (REF.[466])
Spatial mapping	SAXS	Tensor computed tomography (3D)	Bone	Liebi et al., 2015 (REF.[337])
	SAXS	Computed tomography (3D)	Bulk polymer	Hu et al., 2020 (REF.[467])
	SAXS/WAXS	Scanning (2D)	Porous clay	Leu et al., 2016 (REF.[468])
	SAXS/X-ray diffraction	Computed tomography (3D)	Cardiomyocytes	Reichardt et al., 2020 (REF.[469])
Magnetic field	SAXS	Low field	Block copolymer	Gopinadhan et al., 2017 (REF.[470])
	SAXS	Low to high field	Block copolymer	McCulloch et al., 2013 (REF.[335])
UV radiation	SAXS	UV photoswitching	Polymer network	Gu et al., 2018 (REF.[471])
	SAXS/GISAXS	UV photoreduction	Silver colloids	Harada and Katagiri, 2010 (REF.[472])
Etching	GISAXS	Ion etching, lithography	Silica masks, magnetic layers	Meyer et al., 2017 (REF.[340])
	GISAXS	Ion etching, ageing, self-assembly	Semiconductor	Bikondoa et al., 2013 (REF.[473])
Solvent vapour/gas	GISAXS	Gas sorption, chemiresistance	Gold colloids	Olichwer et al., 2016 (REF.[474])
	GISAXS	Solvent vapour, self-assembly	Triblock copolymer film	Lee et al., 2019 (REF.[339])
	GISAXS	Gas, sintering, in operando	Catalyst	Hejral et al., 2016 (REF.[475])
	SAXS	Humidity, temperature	Proton-conductive membrane	Mochizuki et al., 2014 (REF.[476])
Coating	GISAXS	Sputtering	Metal on block copolymer	Schwartzkopf et al., 2017 (REF.[477])
	GISAXS	Spray	Polymer colloid	Zhang et al., 2016 (REF.[478])
	GISAXS	Slot die printing	Ion conducting polymers	Dudenas and Kusoglu, 2019 (REF.[479])
	GISAXS	Atomic layer deposition, X-ray fluorescence	Metals	Dendooven et al., 2016 (REF.[480])

Table 2 (cont.) | **Selected SAS applications**

Experiment	Method	Application	Material	Ref.
Electrochemistry	SAXS	Impedance spectroscopy	Membrane/polyionic liquids	Folkertsma et al., 2017 (REF.[408])
	GISAXS	Electrode roughening	Metal/electrolyte	Ruge et al., 2014 (REF.[481])
	GISAXS	Solar cell ageing	Organic solar cell	Schaffer et al., 2016 (REF.[482])
	SAXS/SANS	Fuel cell conditioning	Battery electrodes	Kabir et al., 2019 (REF.[483])
	SANS	In operando fuel cell	Lithium ion battery	Hattendorf et al., 2020 (REF.[484])
	SAXS	Microstructure	Solid oxide fuel cells	Allen et al., 2014 (REF.[485])
Ozonolysis	SAXS/WAXS	Raman spectroscopy	Organic film	Milsom et al., 2021 (REF.[486])
Self-assembly	GISAXS/grazing incidence WAXS	Liquid–air interface	PbS nanocrystals	Geuchies et al., 2016 (REF.[487])
	SAXS/SANS	Particle size	Catalyst ink	Yang et al., 2017 (REF.[488])
Laser irradiation	GISAXS	Laser-induced periodic structures	Polymer film	Rebollar et al., 2015 (REF.[489])

FTIR, Fourier transform infrared; GISAXS, grazing incidence small-angle X-ray scattering; SANS, small-angle neutron scattering; SAS, small-angle scattering; SAXS, small-angle X-ray scattering; USAXS, ultra-small-angle X-ray scattering; WAXS, wide-angle X-ray scattering.

sampling of macromolecules may include structurally labile regions interspersed with structurally defined regions, such as in modular proteins with repeat motifs connected by flexible linkers. Finally, intrinsically disordered proteins exist as a structurally heterogeneous population with no definable structure. The oligomeric state or conformational sampling of macromolecules may be modelled from SAS profiles in terms of the volume fraction contribution of each individual component to the final scattering intensities. Such analyses include measuring concentration series data to yield concentration-dependent parameters such as R_g, molecular weight and so on that reflect changes in oligomeric state and may include extracting affinity constants between components. Intrinsically disordered or flexible macromolecules can be analysed in terms of ensembles.

The most common application of SAS in structural biology is to build models that describe the structural state(s) of biomolecules in solution[286,287]. For monodisperse solutions, the scattering can be modelled in terms of a single particle; for polydisperse samples, mixtures or ensembles analysis is employed[288,289]. SAS is one of the few techniques capable of generating 3D population-state models to describe such systems[262,277,290]. The models may be calculated ab initio using volume-element bead modelling[263,265,291] or, in the case of proteins, dummy amino acid modelling[267,275] that can include stacked helical structures[292]. Atomistic modelling is also employed and incorporates high-resolution models from X-ray crystallography, NMR spectroscopy[293,294], electron microscopy, homology/molecular dynamic calculations[267,268,295] or normal-mode analysis[266]. Atomistic approaches are routinely used to evaluate differences between high-resolution structures and the solution state(s) of macromolecules that may or may not be coincident, such as the effect of crystal packing forces that may trap single states not present in solution, or build missing regions of mass[268,274] otherwise not accounted for in high-resolution structures due to intrinsic structural disorder. Electron density retrieval has been recently developed for SAXS[296–298] and diverse approaches for modelling membrane protein and other constrained model systems are available[299,300]. More advanced analyses using principal component analysis and singular value decomposition may yield additional insight into the theoretical minimum number of components in a polydisperse sample, and even in cases where intermediates in time-dependent assembly processes cannot be measured in isolation, low-resolution models of the intermediates can be directly derived from the data[291].

Contrast variation can additionally probe the structures of individual components within large assemblies[301]. Different classes of biological macromolecules have different average electron density when measured with SAXS or different average nuclear isotope density (in particular, ^{1}H per unit volume) when measured with SANS. By manipulating the scattering length density of the sample or the scattering length density of the solvent, the component contributions can be selectively contrast-matched to obtain the location of individual components bound within an assembly[44,302–304]. SANS with contrast variation is of particular importance, and can be achieved either by isotopically substituting light hydrogen ^{1}H for deuterium ^{2}H in the solvent or by the isotopic labelling of non-exchangeable ^{2}H in macromolecules. Combining SANS and SAXS offers scope for investigating a wide range of biological samples spanning the simple homogeneous case[305,306] through to more complicated systems such as protein–protein and protein–polynucleotide complexes[307–310], membrane proteins[311–313], nanodiscs[314], macromolecular assemblies[135,315] and nano-conjugates[316] as well as understanding phase transitions[24,25], molecular crowding effects[317,318], protein fibrillation and intermediate fibrillation processes[319–321], self-association, ordering and crystallization processes[89] and intrinsic structural disorder[322,323] in addition to tracking structural responses through time or through alterations to the chemical or physical sample environment[324,325].

Soft matter

Dilute soft-matter systems may be analysed in a similar way to biological macromolecules in solution. Analysing the form factor $P(q)$ during the self-assembly of molecules enables structural changes to be followed in

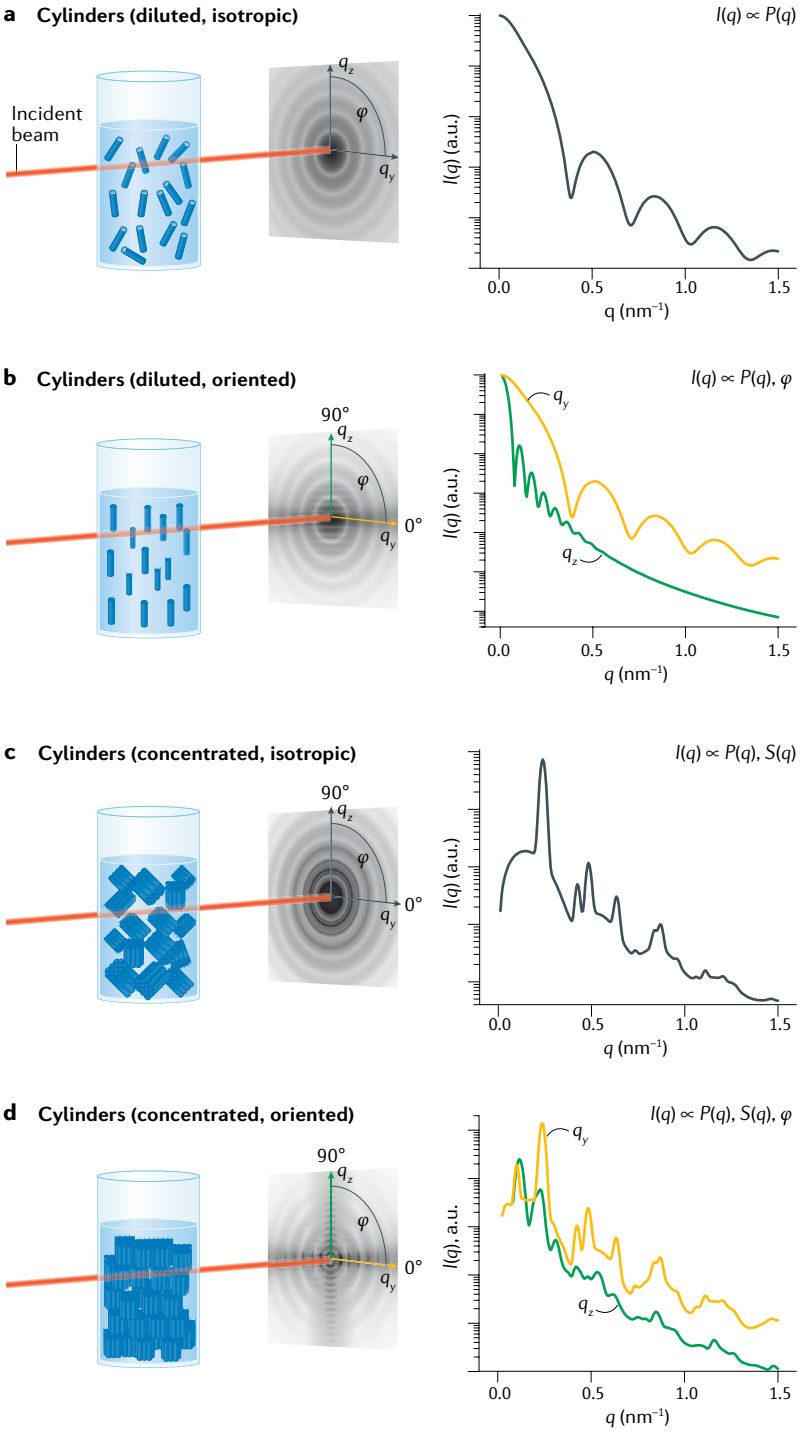

Fig. 9 | **Schematic display of scattering patterns from rod-like cylindrical particles in different concentration regimes and orientations. a** | Diluted, randomly oriented particles relative to the beam path result in isotropic form factor $P(q)$ scattering. The azimuthal intensity for each q,φ (where φ is the azimuthal angle) is equal within statistical variance and can be averaged to achieve better estimates of $I(q)$. **b** | Non-interacting but oriented particles in the beam path produce anisotropic scattering that can be analysed in terms of the dependence of $I(q)$ and φ that may be used for determining the degree of orientation. Here, different 1D intensity profiles are shown calculated for q_y corresponding to $\varphi = 0$ (yellow), which is dominated by scattering from across the oriented cylinder diameters (equatorial scattering), whereas at q_z, $\varphi = 90$ (green), the scattering is dominated by the longer oriented cylinder lengths (meridian scattering). **c** | Concentrated hexagonal clusters of cylinders, where each cluster is randomly oriented in the beam path, produces isotropic scattering. The scattered intensity $I(q)$ is now a function of both the form factor $P(q)$ and the structure factor $S(q)$. Isotropic between-cluster interactions as well as intra-cluster correlated repeat distances manifest in the scattering profile, in particular as Bragg reflections (strong peaks) caused by systematic ordering of the cylinders internal to each cluster. **d** | When the concentrated cylindrical clusters are oriented in the beam, the scattering distribution is as in the second case, that is, the bulk ordering within the sample produces anisotropic scattering. Bragg reflections of the hexagonal arrangement of cylinders within each cluster show along the equator (q_y, yellow) whereas along the meridian (q_z, green) systematic-repeat distances from between the clusters appear as strong peaks caused by the formation of correlated repeat distances of the stacked layers through the sample.

response to variations in external conditions. For example, aggregates evolve by covalent or physical attachment of small units by polymerization or self-assembly; polymers form colloidal suspensions; and amphiphilic molecules such as tensides, phospholipids or block copolymers build stable micellar core–shell structures with different sizes and shapes such as spheres, cylinders, vesicles or multilamellar structures. These evolution steps are typically investigated using microfluidic devices (FIG. 10c). Microfluidic devices may have separate feeding channels for different compounds to create a mixing zone. By controlling continuous flow rates and concentrations into the mixing zone, the kinetics of a reaction or the dynamics of self-assembled structures can be determined on a molecular level with minute to second to sub-millisecond time resolutions[105,326] by positioning the X-ray or neutron beam at various spots along the mixing zone. As an example, a millisecond temporal resolution was demonstrated for the formation process of block copolymer micelles[327–329].

To avoid X-ray radiation damage in organic matter, time-resolved SANS can be used on high-flux neutron sources. One example is a continuous flow sample environment to study potentiometric titrations on an aqueous anionic surfactant solution[330]. Alternatively, a simpler approach involves a stop-flow cell where the reactants are injected stepwise into a vessel illuminated by the beam, which has been used to investigate the time-dependent structural evolution of a microgel[331]. In addition to varying the concentration, other parameters such as temperature, light or electric and magnetic fields can also be applied in a purpose-built reaction chamber. SANS with contrast variation employing $^{1}H/^{2}H$ isotopic substitution is also an invaluable tool across polymer sciences, as illustrated in FIG. 10e.

Depending on their attractive and repulsive forces, aggregates may form superstructures at higher concentrations and result in new phases with repeating and well-ordered distances, which causes the interference function $S(q)$ to become significant. FIGURE 9c shows the scattering pattern for hexagonally arranged

cylinders with randomly oriented superstructures. The type of superstructure formed depends on parameters such as the molecular composition, molecular weight, blend ratio, concentration and solvent. The phases range from close-packed spherical structures to hexagonal or rectangular arranged cylinders, bicontinuous phases and various sheet and lamellar structures. One example is the use of in situ SAXS during solution-spinning of a block copolymer to characterize the different morphologies of the spun hollow fibre membranes[332]. The nanoscale morphology of soft matter may also change under flow and impact material properties during or after fabrication; affected properties include fibre strength, long-range ordering of block copolymers or the optical properties of liquid crystals. For example, flow-induced crystallization of isotactic polypropylene was analysed with Rheo-SAXS and compared with other rheological measurements[333] to obtain information on the mechanisms of polymer crystallization under flow for the development of new 3D-printing and micro-moulding materials.

Condensed soft matter, when considered as a bulk material, can be analysed using similar structural mechanisms to those described above. The only difference is that a rearrangement of the macromolecules inside the material is slow or even hindered when the material is below its glass transition temperature. Instead of the solvent, one of the components of the material itself is now the matrix. In such systems, physical parameters such as temperature play a main role in inducing substructural rearrangements, phase transitions or molecular orientations, in addition to mechanical forces such as pressure, strain, shear, or melt flow, or electrical or magnetic fields (FIG. 9d). By analysing the azimuthal distribution of $I(q)$, the orientation of substructures may be calculated. For example, the microstructural evolution during the step-cycle deformation of a poly(ether ester) elastomer was analysed in terms of the orientation and relaxation of the hard and soft segments of a semi-crystalline polymer[334]. The dynamics of magnetic field-induced alignment of block copolymers was investigated using in situ SAXS to calculate orientation functions[335].

In a blend, the composition, polydispersity, superstructure, orientational order or distribution of a certain compound can be macroscopically heterogeneous. This appears especially in natural or synthetic hierarchical systems and can affect material properties such as stiffness or elasticity. In addition, unwanted heterogeneity is often a problem for functional materials such as fibres, foils or building materials. 2D micro-scanning SAXS experiments and 3D SAXS–computed tomography allow spatial mapping of structure distributions inside materials. SAXS–computed tomography experiments using novel mathematical approaches demonstrated high-resolution orientational mapping of the structures in hierarchical systems such as bone and tooth[336–338].

Self-assembly of block copolymers in thin films is important for many industrial applications, as block copolymers can act as lithographic templates for inorganic materials or as coating materials. Self-assembled block copolymer films can reach an almost perfectly tailored nanometre-sized structure over large areas, which depends on several parameters. GISAXS is a versatile tool for in situ studies of self-assembly processes under the influence of applied vapours[339], fields or temperature (FIG. 10b) and for inorganic material transfer processes[340].

Finally, the structure of hybrid materials with hard and soft matter can also be investigated using SAS. For example, SAXS was used to analyse superstructure formation in 3D continuous networks of binary mixtures of metal nanoparticles with a triblock terpolymer[341]. SAS is an invaluable technique for nanoparticle research in general[342] to interrogate particle sizes and formation, suspension[343], dispersion[344], ordering and crystallization processes[220,345,346].

Hard matter

Applying SAXS to hard materials requires very thin samples or high X-ray energies for sufficient transmission through thick samples, and adds complexity in terms of hardware and sample to detector distances needed to achieve needed minimum q values. Although specialized instruments with energies over 50 keV are available at synchrotron sources, SANS is often preferred because of higher neutron penetration through most hard materials compared with X-rays. With SANS, magnetic samples may also be measured in a magnetic field to separate magnetic and nuclear scattering[6] contributions and provide additional information about the sample magnetic structure.

Parasitic scattering subtraction can be challenging in hard materials. Surface defects on thin samples such as scratches, powder particles, boundaries and voids scatter strongly and create unwanted background. Multiple scattering is also common for powders. However, because the scattering length density and subsequent contrasts are typically higher in solid materials than in soft matter, some of the sample-related parasitic scattering can be mitigated by sample preparation or selection. For example, parasitic surface scattering can be mitigated by polishing. Internal parasitic scattering such as that created by grain boundaries, however, may not typically be mitigated.

Precipitate size, shape and density are important in metals as they affect metal and metal alloy properties during manufacture[347]. Studies of precipitation behaviours in alloys are among the earliest applications of SAS[348]. Low-q USAXS scattering probes grain boundaries and other large features, whereas intermediate-q scattering from SAXS combined with high-q data from WAXS reveals information on precipitate growth and the ordered structure of small atom clusters in the γ-phases of aluminium alloys (FIG. 10d). By combining in situ SAXS and WAXS, the dissolution kinetics of different precipitate populations can be quantified together with their activation energies for computer simulations[349]. SANS is commonly used to analyse steels and nickel-based alloys[350], and typically combined with transmission and scanning electron microscopy, atom probe tomography[351] and other techniques[352]. Combining SAXS and SANS can also be used for simultaneous data analysis because X-ray and neutron contrasts are different for many elements and lead to elemental composition quantification of nanosized oxide precipitates in alloys[353].

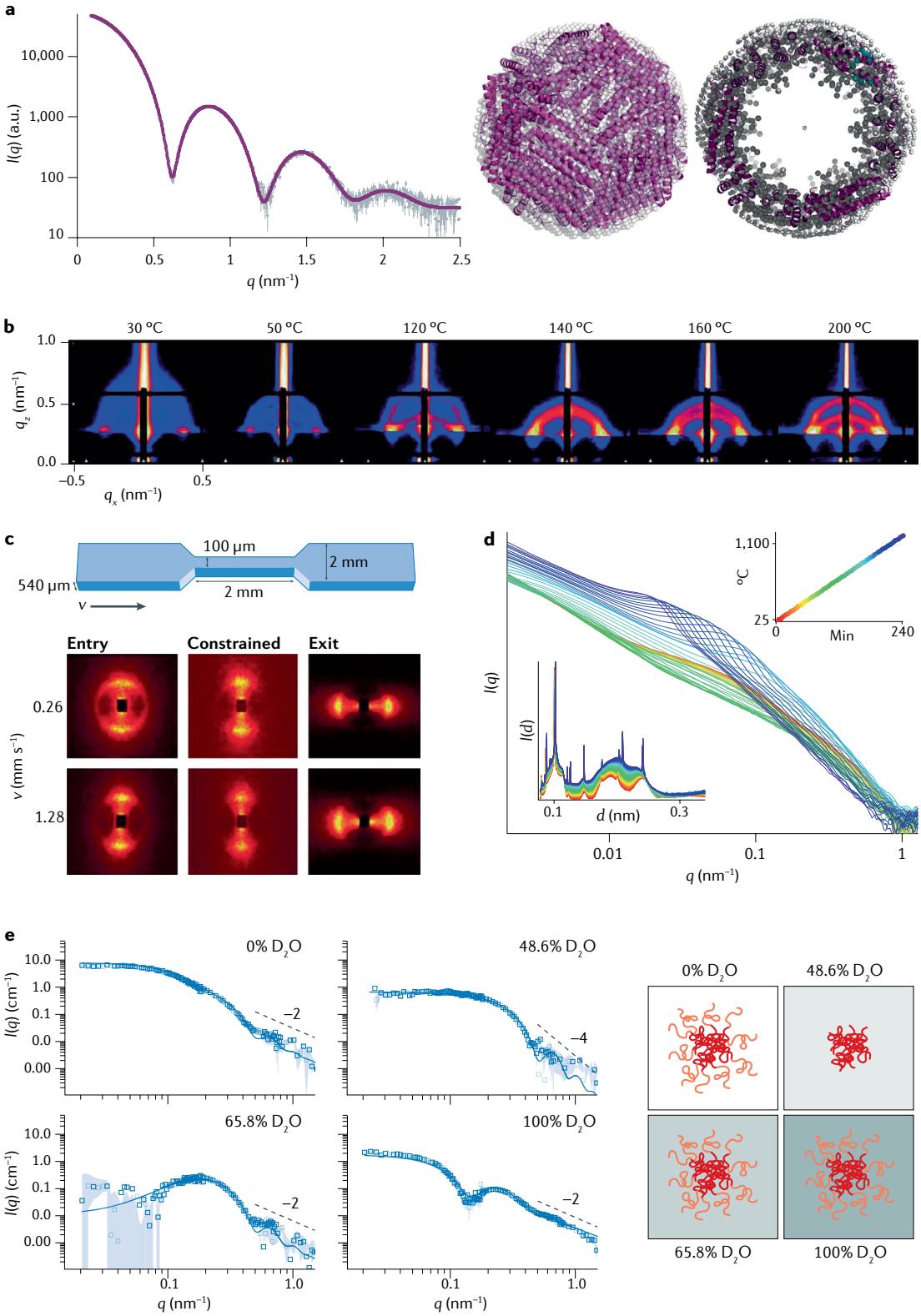

Porosity is another common feature of many natural materials such as rocks, shales, minerals, shells and soils. Pore size distribution, pore shape and pore connectivity are critically important as they determine functional properties as well as the behaviour of liquids such as oil or water in these materials. SANS/ultra-SANS and, to a lesser degree, SAXS/USAXS have been routinely applied to measure porosities[354–357] because they are the only techniques that can access structural information at the nanometre level within bulk samples. SAS results are less sensitive to sample preparation and interrogate larger sample volumes that are more statistically representative compared with optical and electron imaging. In addition, SAS typically characterizes void sizes smaller than

Fig. 10 | **Example applications. a** | Probing the solution state of biomacromolecules using small-angle X-ray scattering (SAXS). A DAMMIN[265] ab initio bead model (transparent grey spheres) and subsequent fit to the SAXS data (magenta line) are shown for the apoferritin protein assembly. A cut-through section of the assembly is also shown from an ab initio model calculated using GASBOR[275], an alternative dummy amino acid modelling approach that includes a modelled hydration layer (small white spheres). A comparison with the high-resolution X-ray crystal structure of apoferritin is also displayed (magenta ribbons). Refer to the SASBDB[369] entry SASDFN8 (REF.[205]). **b** | Grazing incidence small-angle X-ray scattering (GISAXS) patterns of the liquid crystalline block copolymer[497] poly(dimethylsiloxane-b-11-(4′-cyanobiphenyl-4-yloxy)undecylmethacrylate) and the structural microphase order to order evolution of the block copolymer films during thermal annealing from a smectic A phase through poorly oriented hexagonally packed cylinders and towards increased in-plane ordering and the formation of an isotropic phase at higher temperatures. **c** | Small-angle neutron scattering (SANS) data from a SDS/octanol/d-brine system using a microfluidic device[389] consisting of an entry port 2 mm wide funnelling into a constrained 100-μm path length, a chamber 2 mm long and subsequent exit. Example 2D SANS data measured from the fluid at various positions along the micro-cell and at various flow rates (*v*, millimetres per second) are displayed, providing information on lamellar formation and alignment upon entry, constriction and exit. The direction of the flow shown by an arrow[455]. **d** | Ultra-small-angle X-ray scattering (USAXS)–SAXS and wide-angle scattering (WAXS; inset) showing development of precipitate and ordered phases within a nickel–aluminium–silicon-based alloy as a function of temperature (25–1,100 °C)[491,498]. Precipitate size distribution and phase structure, that is, the development of intermetallic γ-phases, informs the development of precipitation-strengthened metal alloys. **e** | SANS with contrast variation measured from a block copolymer consisting of a deuterated polyacylate (dPA) linked to a the polyelectrolyte polystyrene sulfonate (PSS) in solutions containing different %v/v D_2O in the presence of calcium. SANS shows significant changes in scattering intensity as the contrast is varied, illustrating the systematic 'matching-in' and 'matching-out' of the dPA and PSS scattering contributions. Detailed analysis of data shows that the block copolymer spontaneously forms a spherical micelle-like structure of a definable aggregation number and polydispersity, consisting of a solvated dPA core (right schematic, dark red) surrounded by a corona of self-avoiding PSS polymer chains (right schematic, light red)[128]. Part **b** is reprinted from REF.[497], CC BY 3.0 (https://creativecommons.org/licenses/by/3.0/). Part **c** is adapted from REF.[455], CC BY 4.0 (https://creativecommons.org/licenses/by/4.0/). Part **e** is adapted from REF.[128], CC BY 4.0 (https://creativecommons.org/licenses/by/4.0/).

the typical resolution of tomography techniques. SAS experiments using contrast matching with intrusion of liquid or gas can quantify individually open and closed pore populations and pore connectivity under various pressure conditions[358].

Complex materials such as concrete may require a combination of contrast-matched SANS and SAXS to quantify all components[359]. Fresh concrete sets over 40 days at different rates, and understanding its microstructural evolution requires in situ or timed experiments[360] and a combination of techniques including contrast-matched SANS and SAXS, WAXS and imaging[361].

To understand surface oxidation processes, in situ SAXS at temperatures up to 1,500 °C can be performed in a controlled atmosphere. For example, metallic glass powder particles annealed for up to 12 h form an oxide shell on a metallic core with surprisingly homogeneous shell thickness. Absolute calibrated SAXS data analysis yields the oxide weight fraction as a function of time and temperature[362].

GISAS can probe catalyst efficiency and stability using custom-made chambers with temperature, gas composition controls and gas analysers to provide in-line chemical reaction monitoring[363]. Absorption spectroscopy can be added to monitor the electronic structure of catalysts in combination with SAS[364]. When interested in buried structures at the nanometre resolution, the use of standing waves for GISAXS can resolve both the in-plane correlation of the nanostructures and their buried depth information[365].

Reproducibility and data deposition

Numerous ongoing initiatives across the SAS community aim for SAS experiments to be findable, accessible, interoperable and reusable (FAIR). These initiatives focus on data reproducibility and standards, and include establishing reporting guidelines and tabulated data summaries as well as developing data repositories and data formats capturing relevant details of SAS experiments that encompass raw and processed data, modelling and the associated metadata linked to an experiment.

SAS standards in structural biology

For solution scattering experiments in structural biology, reporting guidelines for SAXS and SANS have been set out by the International Union of Crystallography (IUCr) Commission on Small Angle Scattering and the SAS Validation Task Force (SASvtf)[366]. These guidelines are increasingly used across the structural biology community and the subsequent reporting tables have been adopted by numerous journals.

The guidelines encompass four main topics[367]: sample details; instrument details; experimentally determined structural parameters; and software/methods employed for data reduction, analysis and modelling. The sample details include the sample name (for proteins, the protein name must be consistent with UniProt nomenclature), source organism, components of the supporting buffer and sample concentration. Any relevant prior assessment of the sample quality using alternative methods such as multi-angle laser light scattering, analytical ultracentrifugation, dynamic light scattering, SEC, polyacrylamide gel electrophoresis and so on may be reported along with the type of SAS experiment that generated the published SAS data. The instrument that was used to measure the sample should be reported together with instrument parameters such as X-ray and neutron wavelength(s), exposure time(s), sample to detector distance(s), q range(s), intensity calibration method and normalization. Structural parameters extracted from the data including parameters obtained from Guinier, $p(r)$, Porod volume analyses and molecular weight estimates from the scattering data are necessary. The software and methods employed for data reduction, analysis and modelling should be listed. Where fitting the data is required, such as for data–data or data model fits, the assessment of the fit should be reported using the reduced χ^2 test[368] or correlation map P value[242].

Small Angle Scattering Biological Databank

The Small Angle Scattering Biological Databank (SASBDB) is an open access repository for SAS data, metadata and models primarily from bioSAS experiments[369,370]. The SASBDB allows the inclusion of complementary biophysical characterization data related to a SAS experiment and tailored deposition options for

biological samples falling outside the 'typical' solution scattering format. Depositing the scattering experiment in the SASBDB includes four steps: defining the sample or the exact macromolecular sequence information and atomic composition of the buffer or solvent components; uploading the scattering data obtained from the sample along with associated structural parameters; uploading instrument and experimental details; and uploading model and model fit files. Scattering data are uploaded as .dat, .txt or .pdh files in a three-column format for 1D reduced and background-corrected profiles listing q, $I(q)$ and $\sigma I(q)$, where $\sigma I(q)$ are the errors on the scattering intensities. Models are uploaded in .pdb format. A full deposition guide is available through the SASBDB website and the steps and requirements for deposition, including data formats and what is often overlooked by depositors, are described in REF.[369].

The data and metadata of each individual SASBDB entry are assessed by SASBDB curators for consistency and completeness with respect to the IUCr reporting guidelines. Any revisions or additional statements necessary to clarify an individual entry are requested from the depositor prior to acceptance. Importantly, interpreting data, drawing conclusions or policing data quality are not in the remit of the SASBDB and are left to the peer review process and the scientific community.

To impartially assess SASBDB entries, a set of reporting tables, data displays and metric validation tools are populated automatically during deposition and shown on each SASBDB entry page. These plots and tables include a display of the primary scattering data, a comparison of the expected molecular weight calculated from sequence/atomic composition with the experimental molecular weight, a comparison between the R_g obtained from the Guinier approximation and that extracted from the $p(r)$ profile — with corresponding plots of both — in addition to the dimensionless Kratky plot representation of the 1D scattering profile. Graphical sliders on each entry page provide a visual representation of where a SASBDB entry sits relative to all SASBDB entries, from red ('worse') to blue ('better'). These sliders report whether the minimum q value of a data set is sufficient to encompass the reported maximum particle dimension as well as the quality of model fits to the data, including normalized residual plots that provide visual feedback to assess the quality of the model fits.

The preferred route for SAS project uploads is through the SASBDB website, which offers data and metadata deposition. Alternatively, structural biologists with X-ray or neutron diffraction, NMR spectroscopy or electron microscopy data and models can co-deposit SAS data into the SASBDB or link pre-existing SASBDB entries to the Worldwide Protein Data Bank (wwPDB) using its OneDep System.

The Protein Ensemble Database and PDB-Dev

For intrinsically disordered or denatured proteins, combined NMR, SAS and other related data can be deposited in the Protein Ensemble Database[371], including results and models obtained from molecular dynamic simulations. The more recent PDB-Dev databank[372] archives integrative/hybrid structure determination approaches for structural biology[373,374]. The PDB-Dev acts as an archiving hub and links with experimental databanks and techniques including the SASBDB, wwPDB, Electron Microscopy Data Bank (EMDB), Biological Magnetic Resonance Data Bank (BMRB) and Electron Microscopy Public Image Archive (EMPIAR), and references mass spectrometry, Förster resonance energy transfer, chemical cross-linking, electron paramagnetic resonance and proteomics resources.

Data formats CIF and NeXus

The Crystallographic Information File (CIF)[375] is the standardized file format for crystallographic diffraction data and has become part of the structural biology community, with mmCIF in macromolecular crystallography[376] and sasCIF for bioSAS[377]. The format is a machine and human readable Self-defining Text archive and Retrieval (STAR) system that utilizes standard dictionary and ontology definitions to facilitate interoperability between biological macromolecule-focused databanks such as the SASBDB and the wwPDB.

An important challenge for SAS investigations is how to appropriately capture and disseminate experimental results, modelling, instrument details and sample information for increasingly complex experimental set-ups, sample environments and samples. Although the quantifiable monodisperse or polydisperse state of biological macromolecules makes them arguably unique with respect to developing a reporting framework, standardizing such workflows becomes increasingly difficult for the plethora of samples in the material sciences. For example, what may be generally applied to the analysis of any dilute monodispersed protein sample may not be relevant to the temperature-dependent SAXS/USAXS/WAXS analysis of metal precipitate/crystalline phases, or to analysing changes in the direction of liquid-flow densities in microfluidic devices.

To encapsulate numerous and often bespoke SAS projects, the canSAS initiative and the NeXus International Advisory Committee spearheaded the development of the NXcanSAS interoperable data model as a standard packaging system for any type of n-dimensional SAS data, from 1D $I(q)$ profiles to 2D images and multimodal data sets such as TR-SAS, GISAS, (ToF) SANS and so on[378,379]. The NXcanSAS data packaging model integrates the machine-readable Hierarchical Data Format version 5 (HDF5), making it amenable to storing and retrieving large heterogeneous data sets and their metadata. Although at present there are no dedicated databanks for the deposition of SAS investigations for the material sciences, the NXcanSAS philosophy tackles the problem of systematically capturing and packaging data, metadata and analyses for subsequent retrieval from experiments spanning simple to complex systems.

Limitations and optimizations

The processing and interpretation of SAS profiles are linked by several interdependent variables that must all be considered. These variables combine the physics of the scattering process itself with the quality and

reproducibility of the samples, the configurable parameters of the instrumental set-up and the applied data processing and standardization steps. In addition, SAS data provide limited low-resolution information about the specimen and the interpretation of the scattering profiles in terms of structural models may often be ambiguous. This limitation as well as common experimental problems encountered for SAXS, SANS and SAS are discussed below.

Low resolution and the phase problem

Unlike single-crystal diffraction, SAS data cannot be used to locate the positions of individual atoms within a material or to provide high-resolution atomic structures. SAS emerges from the preserved spatial correlations within and between contiguous regions of different average scattering length density in the sample where the sample may be conceptualized as a suspension — for example, liquid–liquid, liquid–solid, solid–solid, solid–gas, solid–surface and so on — that lacks an ordered single-crystal lattice. The absence of such a lattice, which otherwise amplifies the scattering signal to wide angles as diffraction spots to provide atomic length scale information, means that the coherent SAS amplitudes for most samples rapidly decrease with increasing scattering angle. The coherent portions of a SAS profile predominantly capture the spatial information of long-range distance correlations between the density variations of the suspension. These variations go to define the extent, shape and surface morphology of any one region of averaged scattering length density, as opposed to defining each atomic position within the sample. SAS is by definition 'low resolution'.

A common issue for SAXS, SANS, X-ray and neutron crystallography is that the phase information of the scattered amplitudes is lost in the measured intensities. The loss of phase information means it is impossible to directly transform an individual scattering profile into a real-space structure, which requires both the amplitudes and phases of the scattered waves. The experimental scattering data are also measured over a limited momentum transfer range $[q_{min}, q_{max}]$ with finite Δq intervals, making experimental SAS data discontinuous and incomplete because of instrument resolution and the limits of detector technology. Indirect methods are therefore usually employed to extract real-space information such as distance distributions (refer to Results). The phase problem and the nature of the data cause an issue for SAS data interpretation. When developing real-space models, multiple distinct real-space objects can sometimes yield equivalent calculated scattering profiles[380] that all provide an adequate description of, and fit, the experimental data. The inherent ambiguity of an experimental scattering profile, where more than one model may fit the data, requires additional constraints or assumptions during data interpretation. These constraints may be based on the physical nature or chemistry of the sample, or the inclusion of additional information. The analysis of multiple sets of experimental data collected under different conditions, most notably SANS contrast variation, yields a set of interrelated scattering profiles that limit modelling outcomes. SAS is often used with other methods such as electron microscopy, NMR, Förster resonance energy transfer and so on, and the information from these methods also allows further ambiguity reduction in SAS data interpretation.

Common experimental issues

SAXS. For some sample categories such as biological or soft materials, for example polymers and gels, sample damage may be caused by high radiation doses during SAXS measurements. As X-rays primarily interact with electrons via absorption or scattering processes, they unavoidably form free radicals or break chemical bonds within the sample[381]. This effect becomes significant under high-flux synchrotron beams, where beam-induced sample heating may also occur. Detecting and quantifying X-ray-induced damage[382,383] by, for example, using on-the-fly comparative data analysis during sample exposure[242], and mitigating X-ray damage effects by, for example, altering the sample environment[198,384–388] or measuring sample states prior to the onset of damage, are a critical component of SAXS.

SANS. Regular ^{1}H dominates the isotopic composition of many biological and soft-matter samples used for SANS. The incoherent scattering length of ^{1}H is extremely large compared with other isotopes and samples rich in ^{1}H produce incoherent background that may require increasing sample concentration or sample exposure time to improve coherent scattering pattern measurements. Alternatively, the isotopic substitution of ^{1}H for ^{2}H by, for example, substituting $^{1}H_2O$ with $^{2}H_2O$ in a supporting solvent or the non-exchangeable deuteration of a macromolecule alters the neutron contrast and decreases incoherent scattering contributions. However, the substitution of ^{1}H for ^{2}H may also decrease the solubility of a macromolecule or alter the binding affinity between components of a sample. In addition, as neutron beams are typically much larger in size than X-ray beams, SANS experiments also often require larger sample quantities (100s of microlitres to millilitres) than SAXS samples (10s to 100s of microlitres), especially during contrast variation experiments[59]. However, recent advances in hardware and neutron flux have seen decreases in sample exposure times and beam sizes that are useful for higher-contrast systems, even in microfluidic sample environments[389].

Data analysis from ToF SANS instruments is more complicated compared with selectable single-wavelength SANS. Portions of the incident neutrons gain energy when interacting with hydrogen in the sample, leading to the incorrect estimation of the total ToF and, hence, the estimation of the neutron wavelengths, resulting in the rise of incoherent background. This issue gets compounded with ToF SANS as the background and transmission are also wavelength-dependent[162,177,390,391]. For hard-matter SANS experiments, the Bragg edge effect has to be considered[392,393]. In the Bragg edge effect, neutrons of certain wavelengths undergo full reflection, which leads to a dip in the transmission function and makes it impossible to obtain $I(q)$ for a range of

Mean-free path
The average distance travelled between successive collisions of an X-ray or neutron with the atoms of a material, which modifies the direction or energy of the X-rays or neutrons (for example, between multiple scattering events).

neutron wavelengths, resulting in possible gaps in the data.

General SAS. When background scattering contributions must be subtracted, as is the case for structural analysis of dilute biomolecules or polymers, accurately measuring both the sample scattering and the background scattering is necessary[60]. For solutions, the background subtraction requires the supporting solvent of the sample to be matched exactly to the corresponding solvent blank[59,394] in terms of solvent X-ray or neutron scattering and absorption properties. Matching the sample solvent to the background solvent, for example by using dialysis, may be difficult if the sample is prone to self-association over time, especially as the sample concentration increases. The particles themselves occupy space within the sample that is not present in the pure solvent, meaning the effective volume of solvent illuminated by an X-ray or neutron beam is always smaller for the sample than the solvent blank. Diluting the sample and performing a concentration series measurement will yield insight into background solvent mismatch or whether samples undergo concentration-dependent oligomerization. In the very dilute regime, the excluded-volume effect is typically of little consequence; for example, for protein samples less than 5–10 mg ml^{-1}. However, for SANS, additional contributions from incoherent spin scattering from solvents rich in ^{1}H may complicate sample solvent background matching and decrease the accuracy of the subtraction process; isotopically, substitution ^{1}H with ^{2}H can mitigate the issue. It is also important that the experimental configuration of an instrument stays near identical between measurements so that the scattering and absorption contributions by the instrument (for example, from optical devices, sample holders and so on) are taken into account during any data subtraction procedures. Modern instruments are manufactured to the highest levels of precision to ensure consistent instrument backgrounds are achieved.

The polydispersity of a sample also poses a challenge for data interpretation. The scattering profiles from these types of dilute polydisperse system represent a summed contribution from all components in the population $I_k(q)$, weighted by their volume fractions, v_k:

$$I(q) = \sum_k v_k I_k(q). \quad (15)$$

As the distribution of states within in a population widens, it becomes increasingly difficult to delineate and quantify individual particle contributions within the dilute population[245]. This is especially the case with aggregate formation: as $I(q)$ scales to the square of a kth component's particle volume, even trace aggregate at low volume fraction can ruin a SAXS or SANS profile. Measuring concentration series data to evaluate concentration-dependent parameters[224,395] that reflect changes in oligomeric state and extracting affinity constants[396] can yield insights into polydispersity.

The physical separation of mixture components prior to measurement has also become increasingly popular, for example via in-line SEC or ion-exchange chromatography[199–202,204,205,387,397,398], although the results are not always trivial to analyse. Chromatographic separation experiments require identification and correction for background scattering fluctuations, which — especially for X-rays — can be caused by potential beam-induced deposition of the sample on the capillary/cell surface during the chromatography run (capillary fouling/radiation damage)[386,387] or the release of dissolved gasses as bubbles caused by beam-induced heating. The effectiveness of the chromatographic separation of the sample components must also be assessed to determine whether the elution has been successful or whether poorly separated species with overlapping peaks still require data analysis in terms of component mixtures[398,399]. Outside the dilute regime, more advanced data analysis and models are required to describe the size distribution and particle interactions[252,400–403].

Another challenge for both SAXS and SANS is multiple scattering[404–406], where some or most of the detected neutrons or X-rays represent more than one scattering event inside the sample[129]. Multiple scattering may occur when the mean-free path between two scattering events for each neutron or X-ray is comparable with or smaller than the sample thickness. Although multiple scattering theory has been developed[407], some ways to mitigate this issue include studying thinner samples, decreasing the wavelength or changing contrast.

Challenges for SAS

The applicability of SAS across disciplines spanning biology, soft matter and hard matter effectively makes the technique universal. Going forwards, the challenge continues to be combining quality sample preparation and interpreting the data given the inherent ambiguity of SAS data analysis. Here, prior assumptions from a priori knowledge or the inclusion of experimental results from alternative techniques are often indispensable. For example, numerous assumptions help to guide the modelling outcomes during restoration of protein structural state(s) — assumptions such as proteins as single polymers not forming disconnected entities, not having hard geometric or spiked surfaces, being enantiomer-selective and not being branched polymers[8]. Although these constraints significantly reduce unfeasible modelling outcomes, the scattering data may remain highly ambiguous[380] and modelling results may be over-interpreted.

The difficulty of interpreting data increases as the complexity of a sample increases from isolated non-interacting dilute materials to higher-order integrated systems. Understanding the physicality of the sample prior to an experiment and how it may be affected when exposed to radiation, and interpreting potentially ambiguous data, are the fundamental challenge facing all SAS experiments. Structure factor contributions, polydispersity, heterogeneous contrast, multiple scattering events, orientation bias, susceptibility to radiation damage or simple ageing all have to be considered. Consequently, bespoke modelling approaches based on general SAS principles need to be tailored to interpret data from specific samples, and often invoke

information from various methods to support the conclusions drawn from the data.

Outlook

SAS is a highly dynamic field and new approaches are constantly being developed to tackle the intrinsic data ambiguity and complex sample conditions.

Novel approaches

At the hardware level, in situ complementary techniques enable one to condition and co-analyse the sample, whereas in operando measurements follow the structural changes correlated with the functional cycles of the sample. Examples of sample conditioning include illumination, temperature, humidity and the application of magnetic fields. On bioSAS instruments, SEC is routinely employed with additional light-scattering devices to ensure sample monodispersity[205]. In situ analysis techniques available include UV–Vis absorbance and fluorescence spectroscopies, dynamic light scattering and impedance spectroscopy[408]. Today, SAXS and SANS can also be measured simultaneously[409]. In operando systems that can correlate sample function to sample structural states are used to characterize electrical devices[410–413] and improve technical processes in energy storage. The beam itself can also be adapted to the sample conditions or to reveal particular aspects of the sample. For instance, very high-intensity X-ray beams make it possible to measure aerosols under ambient conditions[414]. Reducing the beam size while keeping sufficient intensity enables scanning with high spatial resolution both using X-rays[415] and neutrons[416].

Recent advances in data analysis are aimed at developing new approaches to assess data quality and build structural models. For biological applications, some examples are a method to quantitatively estimate the information content in SAS data (SHANUM[241]), an iterative procedure for density modelling (DENSS[296–298]) and an approach to reconstruct the shape of an intermediate for evolving mixtures (DAMMIX[291]). Several recent developments also include constraints inherited from complementary techniques[273].

Looking forwards

In the experimental field, a priority for SAS over the next decade is to capitalize on next-generation and increasingly brilliant radiation sources to interrogate structure and dynamics in the solid, fluid and surface states, with a focus on very fast time-resolved processes. Effective sample delivery modes such as liquid jets/sheets, microfluidic and raster 'on-chip' devices, tape drives and so on, as well as sample environments based on 3D printing, will play an important role. The effective use of high-brilliance sources will require very low-background instruments coupled to controllable beam parameters in terms of beam shape, size, energy and flux, and the inclusion of pump and probe beam cutter systems to deliver X-ray pulses in combination with sensitive high frame-rate detectors.

Future SAXS applications will require a synergic approach providing sample environments and X-ray instruments that can be tailored case by case as well as adaptable to standard, well-established experimental approaches. In line with these developments, understanding and mitigating radiation damage will likely require further evaluation with respect to sample preparation and experimental planning as the X-ray flux density of new generation instruments continues to increase.

For SANS, radiation damage is much less of an issue. However, as SANS flux density is much lower than for SAXS, longer sample exposure times and larger sample quantities are typically required, which constrains time-resolved studies. Consequently, the priority for many existing and proposed neutron facilities is the optimization of neutron flux in step with reducing instrument background. For instance, the sample cell used for SEC–SANS measurements on the Institut Laue-Langevin (ILL) D22 instrument[200] and for microfluidic time-resolved applications[389] has been optimized to make use of all of the sample volume and mask any source of background scatter to increase the accuracy and reproducibility of the measurements. This has allowed a lowering of the incident beam intensity and beam size required to obtain interpretable data. Such beam line and sample environment upgrades are expected to lower sample quantities, allow for shorter exposure times and allow for automated and higher-throughput sample delivery at SANS beam lines.

Instrument developments will also necessitate increasing computational power for data analysis, storage, interoperability and access. Future SAS investigations will likely generate terabytes of data per experiment. There will therefore be a need for faster automated data processing as well as the systematic management of the raw and associated experimental metadata. This will likely include the development of interdisciplinary and mutually interpretable open access databanks. It is also expected that analysis and modelling methods will be developed further to capitalize on the rapidly increasing power of modern computers.

Looking beyond

As a near-universal technique for interrogating the structure and disposition of materials, SAS is well positioned to seamlessly integrate with diverse areas of research. The inclusion of parallel hybrid methods for SAS data interpretation is of paramount importance to build more complete and accurate descriptions of materials, materials properties and materials' response to change. These associated methods include the co-analysis of SAXS and SANS data with atomic force microscopy, X-ray and neutron crystallography, solution and solid-state NMR spectroscopy, mass spectrometry, HDXMS (hydrogen–deuterium exchange coupled with mass spectroscopy), Förster resonance energy transfer, circular dichroism spectropolarimetry, and infrared, Raman scattering, static and dynamic laser light scattering as well as computational molecular dynamics, modelling and data simulations. SAS may also be used together with X-ray powder diffraction to study colloidal crystal suspensions[417] or with light refractive index measurements to answer interesting optical questions such as the construction of spherical eye lenses[418]. The recent 'resolution revolution' in cryo electron microscopy[419,420]

is poised to take advantage of SAS to complement the single, static-image representation of frozen biomolecules with population-state processes that scattering experiments can access, such as self-association, assembly, ensemble states, dynamics, crowding, equilibrium processes, kinetics and even the structure and dynamics of water[421]. A very active subject today concerns the combined application of SAS with inelastic X-ray and neutron scattering, X-ray spectroscopy, reflectivity and NMR to further our understanding of water 'in bulk' (solid or liquid) or at surfaces[422–426], which has implications across numerous industries, for example in pharmaceutical manufacturing, food processing and so on, as well as providing fundamental science for chemistry, biology, geophysics, metallurgy, additive manufacturing, climate and the environment.

Published online: 12 October 2021

1. Glatter, O. A new method for the evaluation of small-angle scattering data. *J. Appl. Cryst.* **10**, 415–421 (1977).
2. Feigin, L. A. & Svergun, D. I. *Structure Analysis by Small-Angle X-ray and Neutron Scattering* (Plenum, 1987).
3. Fratzl, P. Small-angle scattering in materials science — a short review of applications in alloys, ceramics and composite materials. *J. Appl. Cryst.* **36**, 397–404 (2003).
4. Glatter, O. & Kratky, O. *Small Angle X-ray Scattering* (Academic, 1982).
5. Mortensen, K. in *Advanced Functional Molecules and Polymers* Vol. 2 (ed Nalwa, H. S.) 223–269 (Overseas Publishers Association, 2001).
6. Mühlbauer, S. et al. Magnetic small-angle neutron scattering. *Rev. Mod. Phys.* **91**, 015004 (2019).
7. Radlinski, A. P. & Hinde, A. L. Small angle neutron scattering and petroleum geology. *Neutron. N.* **13**, 10–14 (2002).
8. Svergun, D. I., Koch, M. H. J., Timmins, P. A., & May, R. P. *Small Angle X-Ray and Neutron Scattering from Solutions of Biological Macromolecules* 1st edn (Oxford Univ. Press, 2013).
9. Stieger, M., Richtering, W., Pedersen, J. S. & Lindner, P. Small-angle neutron scattering study of structural changes in temperature sensitive microgel colloids. *J. Chem. Phys.* **120**, 6197–6206 (2004).
10. Higgins, J. S. & Benoit, H. C. *Polymers and Neutron Scattering* (Clarendon, 1994).
11. Renaud, G. et al. Real-time monitoring of growing nanoparticles. *Science* **300**, 1416–1419 (2003).
12. Sinha, S. K., Sirota, E. B., Garoff, S. & Stanley, H. B. X-ray and neutron scattering from rough surfaces. *Phys. Rev. B Condens. Matter* **38**, 2297–2311 (1988).
13. Müller-Buschbaum, P. in *Applications of Synchrotron Light to Scattering and Diffraction in Materials and Life Sciences* (eds Gomez, M., Nogales, A., Garcia-Gutierrez, M. C. & Ezquerra, T. A.) 61–89 (Springer, 2009).
14. Hexemer, A. & Muller-Buschbaum, P. Advanced grazing-incidence techniques for modern soft-matter materials analysis. *IUCrJ* **2**, 106–125 (2015).
15. Müller-Buschbaum, P. Grazing incidence small-angle neutron scattering: challenges and possibilities. *Polym. J.* **45**, 34–42 (2013).
16. Meisburger, S. P., Thomas, W. C., Watkins, M. B. & Ando, N. X-ray scattering studies of protein structural dynamics. *Chem. Rev.* **117**, 7615–7672 (2017).
17. Krueger, J. K. & Wignall, G. D. in *Neutron Scattering in Biology Biological and Medical Physics, Biomedical Engineering* Ch. 8 (eds Fitter, J., Gutberlet, T. & Katsaras, J.) 127–160 (Springer, 2006).
18. Lakey, J. H. Neutrons for biologists: a beginner's guide, or why you should consider using neutrons. *J. R. Soc. Interface R. Society* **6** (Suppl. 5), S567–S573 (2009).
19. Koch, M. H., Vachette, P. & Svergun, D. I. Small-angle scattering: a view on the properties, structures and structural changes of biological macromolecules in solution. *Q. Rev. Biophys.* **36**, 147–227 (2003).
20. Krueger, S. SANS provides unique information on the structure and function of biological macromolecules in solution. *Phys. B: Condens. Matter* **241–243**, 1131–1137 (1997).
21. Putnam, C. D., Hammel, M., Hura, G. L. & Tainer, J. A. X-ray solution scattering (SAXS) combined with crystallography and computation: defining accurate macromolecular structures, conformations and assemblies in solution. *Q. Rev. Biophys.* **40**, 191–285 (2007).
22. Lipfert, J. & Doniach, S. Small-angle X-ray scattering from RNA, proteins, and protein complexes. *Annu. Rev. Biophys. Biomol. Struct.* **36**, 307–327 (2007).
23. Bizien, T. et al. A brief survey of state-of-the-art BioSAXS. *Protein Peptide Lett.* **23**, 217–231 (2016).
24. Da Vela, S. et al. Kinetics of liquid–liquid phase separation in protein solutions exhibiting LCST phase behavior studied by time-resolved USAXS and VSANS. *Soft Matter* **12**, 9334–9341 (2016).
25. Martin, E. W. et al. A multi-step nucleation process determines the kinetics of prion-like domain phase separation. *Nat. Commun.* **12**, 4513 (2021).
26. Renaud, G., Lazzari, R. & Leroy, F. Probing surface and interface morphology with grazing incidence small angle X-ray scattering. *Surf. Sci. Rep.* **64**, 255–380 (2009).
27. Smilgies, D. M., Busch, P., Papadakis, C. M. & Posselt, D. Characterization of polymer thin films with small-angle X-ray scattering under grazing incidence (GISAXS). *Synchrotron Radiat. N.* **15**, 35–42 (2002).
28. Allen, A. J. & Thomas, J. J. Analysis of C–S–H gel and cement paste by small-angle neutron scattering. *Cem. Concr. Res.* **37**, 319–324 (2007).
29. Adams, C. P. et al. Small and ultra-small angle neutron scattering studies of commercial milk. *Food Struct.* **21**, 100120 (2019).
30. Peyronel, F., Marangoni, A. G. & Pink, D. A. Using the USAXS technique to reveal the fat globule and casein micelle structures of bovine dairy products. *Food Res. Int.* **129**, 108846 (2020).
31. Fister, T. T. in *XAFS Techniques for Catalysts, Nanomaterials, and Surfaces* (eds Iwasawa, Y., Asakura, Y., & Tada, M.) 237–250 (Springer International, 2017).
32. Sahle, C. J. et al. Planning, performing and analyzing X-ray Raman scattering experiments. *J. Synchrotron Radiat.* **22**, 400–409 (2015).
33. Lundberg, M. & Wernet, P. in *Synchrotron Light Sources and Free-Electron Lasers: Accelerator Physics, Instrumentation and Science Applications* (eds Jaeschke, E., Khan, S., Schneider, J. R. & Hastings, J. B.) 1–52 (Springer International, 2019).
34. Ament, L. J. P., van Veenendaal, M., Devereaux, T. P., Hill, J. P. & van den Brink, J. Resonant inelastic X-ray scattering studies of elementary excitations. *Rev. Mod. Phys.* **83**, 705–767 (2011).
35. Dziarzhytski, S. et al. The TRIXS end-station for femtosecond time-resolved resonant inelastic X-ray scattering experiments at the soft X-ray free-electron laser FLASH. *Struct. Dyn.* **7**, 054301 (2020).
36. Slowik, J. M., Son, S. K., Dixit, G., Jurek, Z. & Santra, R. Incoherent X-ray scattering in single molecule imaging. *N. J. Phys.* **16**, 073042 (2014).
37. Sears, V. F. Neutron scattering lengths and cross sections. *Neutron. N.* **3**, 26–37 (1992).
38. Squires, G. L. *Introduction to the Theory of Thermal Neutron Scattering* 3rd edn (Cambridge Univ. Press, 2012).
39. Zaccai, G. & Jacrot, B. Small angle neutron scattering. *Annu. Rev. Biophys. Bioeng.* **12**, 139–157 (1983).
40. Andreani, C., Colognesi, D., Mayers, J., Reiter, G. F. & Senesi, R. Measurement of momentum distribution of lightatoms and molecules in condensed matter systems using inelastic neutron scattering. *Adv. Phys.* **54**, 377–469 (2005).
41. Andreani, C., Krzystyniak, M., Romanelli, G., Senesi, R. & Fernandez-Alonso, F. Electron-volt neutron spectroscopy: beyond fundamental systems. *Adv. Phys.* **66**, 1–73 (2017).
42. Middendorf, H. D. Biophysical applications of quasi-elastic and inelastic neutron scattering. *Annu. Rev. Biophys. Bioeng.* **13**, 425–451 (1984).
43. Ibel, K. & Stuhrmann, H. B. Comparison of neutron and X-ray scattering of dilute myoglobin solutions. *J. Mol. Biol.* **93**, 255–265 (1975).
44. Heller, W. Small-angle neutron scattering and contrast variation: a powerful combination for studying biological structures. *Acta Crystallogr. Sect. D* **66**, 1213–1217 (2010).
45. Whitten, A. E. & Trewhella, J. in *Micro and Nano Technologies in Bioanalysis: Methods and Protocols* (eds Foote, R. S. & Lee, J. W.) 307–323 (Humana, 2009).
46. Grishaev, A., Anthis, N. J. & Clore, G. M. Contrast-matched small-angle X-ray scattering from a heavy-atom-labeled protein in structure determination: application to a lead-substituted calmodulin–peptide complex. *J. Am. Chem. Soc.* **134**, 14686–14689 (2012).
47. Garcia-Diez, R., Gollwitzer, C. & Krumrey, M. Nanoparticle characterization by continuous contrast variation in small-angle X-ray scattering with a solvent density gradient. *J. Appl. Cryst.* **48**, 20–28 (2015).
48. Hua, D. W., D'Souza, J. V., Schmidt, P. W. & Smith, D. M. in *Studies in Surface Science and Catalysis* Vol. 87 (eds Rouquerol, J., Rodrīguez-Reinoso, F., Sing, K. S. W. & Unger, K. K.) 255–261 (Elsevier, 1994).
49. Larsen, A. H., Pedersen, J. S. & Arleth, L. Assessment of structure factors for analysis of small-angle scattering data from desired or undesired aggregates. *J. Appl. Cryst.* **53**, 991–1005 (2020).
50. Santoro, G. & Yu, S. in *X-ray Scattering* (ed. Ares, A. E.) 29–60 (IntechOpen, 2017).
51. Guinier, A. La diffraction des rayons X aux tres petits angles; application a l'etude de phenomenes ultramicroscopiques [French]. *Ann. Phys.* **12**, 161–237 (1939).
52. Guinier, A. & Fournet, G. *Small Angle Scattering of X-Rays* (Wiley, 1955).
53. Stuhrmann, H. B. & Kirste, R. G. Elimination der intrapartikulären Untergrundstreuung bei der Röntgenkleinwinkelstreuung an kompakten Teilchen (Proteinen) [German]. *Z. für Physikalische Chem.* **46**, 247 (1965).
54. Stuhrmann, H. Interpretation of small-angle scattering functions of dilute solutions and gases. A representation of the structures related to a one-particle scattering function. *Acta Cryst. Sect. A* **26**, 297–306 (1970).
55. Sivia, D. S. *Elementary Scattering Theory: For X-ray and Neutron Users* (Oxford Univ. Press, 2011).
56. Fernandez-Alonso, F. & Price, D. L. in *Experimental Methods in the Physical Sciences* Vol. 44 (Academic, 2013).
57. Lovesey, S. W. *Theory of Neutron Scattering from Condensed Matter* Vols 1 and 2 (Clarendon, 1984).
58. Pauw, B. R. Everything SAXS: small-angle scattering pattern collection and correction. *J. Phys. Condens. Matter* **25**, 383201 (2013).
59. Jeffries, C. M. et al. Preparing monodisperse macromolecular samples for successful biological small-angle X-ray and neutron-scattering experiments. *Nat. Protoc.* **11**, 2122–2153 (2016).
60. Grishaev, A. Sample preparation, data collection, and preliminary data analysis in biomolecular solution X-ray scattering. *Curr. Protoc. ProteSci.* **70**, 17.14.11–17.14.18 (2012).
61. Krueger, S. in *Biological Small Angle Scattering: Techniques, Strategies and Tips* (eds Chaudhuri, B., Muñoz, I. G., Qian, S. & Urban, V. S.) 65–85 (Springer, 2017).
62. Sarachan, K. L., Curtis, J. E. & Krueger, S. Small-angle scattering contrast calculator for protein and nucleic acid complexes in solution. *J. Appl. Cryst.* **46**, 1889–1893 (2013).
63. Whitten, A. E., Cai, S. & Trewhella, J. MULCh: modules for the analysis of small-angle neutron contrast variation data from biomolecular assemblies. *J. Appl. Cryst.* **41**, 222–226 (2008).
64. Allen, A. J. in *International Tables for Crystallography* Ch. 5.8, 673–696 (Wiley, 2019).
65. Fritz, G. & Bergmann, A. SAXS instruments with slit collimation: investigation of resolution and flux. *J. Appl. Cryst.* **39**, 64–71 (2006).
66. Bruetzel, L. K. et al. A Mo-anode-based in-house source for small-angle X-ray scattering measurements

of biological macromolecules. *Rev. Sci. Instrum.* **87**, 025103 (2016).
67. Skarzynski, T. Collecting data in the home laboratory: evolution of X-ray sources, detectors and working practices. *Acta Cryst. Sect. D.* **69**, 1283–1288 (2013).
68. Tache, O. et al. MOMAC: a SAXS/WAXS laboratory instrument dedicated to nanomaterials. *J. Appl. Cryst.* **49**, 1624–1631 (2016).
69. Larsson, D. H., Takman, P. A. C., Lundström, U., Burvall, A. & Hertz, H. M. A 24 keV liquid-metal-jet X-ray source for biomedical applications. *Rev. Sci. Instrum.* **82**, 123701 (2011).
70. Hemberg, O., Otendal, M. & Hertz, H. M. Liquid-metal-jet anode electron-impact X-ray source. *Appl. Phys. Lett.* **83**, 1483–1485 (2003).
71. Lyngso, J. & Pedersen, J. S. A high-flux automated laboratory small-angle X-ray scattering instrument optimized for solution scattering. *J. Appl. Cryst.* **54**, 295–305 (2021).
72. Bergmann, A., Orthaber, D., Scherf, G. & Glatter, O. Improvement of SAXS measurements on Kratky slit systems by Gobel mirrors and imaging-plate detectors. *J. Appl. Cryst.* **33**, 869–875 (2000).
73. Soliman, M., Jungnickel, B.-J. & Meister, E. Stable desmearing of slit-collimated SAXS patterns by adequate numerical conditioning. *Acta Cryst. Sect. A* **54**, 675–681 (1998).
74. Lake, J. An iterative method of slit-correcting small angle X-ray data. *Acta Cryst.* **23**, 191–194 (1967).
75. Glatter, O. A new iterative method for collimation correction in small-angle scattering. *J. Appl. Cryst.* **7**, 147–153 (1974).
76. Singh, M. A., Ghosh, S. S. & Shannon Jnr, R. F. A direct method of beam-height correction in small-angle X-ray scattering. *J. Appl. Cryst.* **26**, 787–794 (1993).
77. Strobl, G. A new method of evaluating slit-smeared small-angle X-ray scattering data. *Acta Crystallogr. Sect. A* **26**, 367–375 (1970).
78. Vonk, C. A procedure for desmearing X-ray small-angle scattering curves. *J. Appl. Cryst.* **4**, 340–342 (1971).
79. Bonse, U. & Hart, M. Tailless X-ray single-crystal reflection curves obtained by multiple reflection. *Appl. Phys. Lett.* **7**, 238–240 (1965).
80. Pedersen, J. S. in *Modern Aspects of Small-Angle Scattering* (ed Brumberger, H.) 57–91 (Springer, 1995).
81. Gravatt, C. C. & Brady, G. W. Slit smearing effects in the Bonse–Hart small-angle X-ray diffractometer. *J. Appl. Cryst.* **2**, 289–295 (1969).
82. Bolze, J. & Gateshki, M. Highly versatile laboratory X-ray scattering instrument enabling (nano-)material structure analysis on multiple length scales by covering a scattering vector range of almost five decades. *Rev. Sci. Instrum.* **90**, 123103 (2019).
83. Round, A. et al. BioSAXS Sample Changer: a robotic sample changer for rapid and reliable high-throughput X-ray solution scattering experiments. *Acta Cryst. Sect. D.* **71**, 67–75 (2015).
84. Martel, A., Liu, P., Weiss, T. M., Niebuhr, M. & Tsuruta, H. An integrated high-throughput data acquisition system for biological solution X-ray scattering studies. *J. Synchrotron Radiat.* **19**, 431–434 (2012).
85. Hura, G. L. et al. Robust, high-throughput solution structural analyses by small angle X-ray scattering (SAXS). *Nat. Methods* **6**, 606–612 (2009).
86. David, G. & Perez, J. Combined sampler robot and high-performance liquid chromatography: a fully automated system for biological small-angle X-ray scattering experiments at the Synchrotron SOLEIL SWING beamline. *J. Appl. Cryst.* **42**, 892–900 (2009).
87. Osaka, K. et al. High-throughput and automated SAXS/USAXS experiment for industrial use at BL19B2 in SPring-8. *AIP Conf. Proc.* **1741**, 030003 (2016).
88. Lutz-Bueno, V. et al. Scanning-SAXS of microfluidic flows: nanostructural mapping of soft matter. *Lab.Chip* **16**, 4028–4035 (2016).
89. Pham, N. et al. Coupling high throughput microfluidics and small-angle X-ray scattering to study protein crystallization from solution. *Anal. Chem.* **89**, 2282–2287 (2017).
90. Buffet, A. et al. P03, the microfocus and nanofocus X-ray scattering (MiNaXS) beamline of the PETRA III storage ring: the microfocus endstation. *J. Synchrotron Radiat.* **19**, 647–653 (2012).
91. Hubbell, J. H. & Seltzer, S. M. X-Ray Mass Attenuation Coefficients. *NIST Standard Reference Database 126* https://doi.org/10.18434/T4D01F (2004).
92. Ballauff, M. & Jusufi, A. Anomalous small-angle X-ray scattering: analyzing correlations and fluctuations in polyelectrolytes. *Colloid Polym. Sci.* **284**, 1303–1311 (2006).
93. Seifert, S., Winans, R. E., Tiede, D. M. & Thiyagarajan, P. Design and performance of a ASAXS instrument at the Advanced Photon Source. *J. Appl. Cryst.* **33**, 782–784 (2000).
94. Berger, M. J. et al. *XCOM: Photon Cross Sections Database, NIST Standard Reference Database 8 (XGAM)* (NIST, 2010).
95. Stuhrmann, H. B. Resonant scattering in macromolecular structure research. Applications in molecular biology and material science. *Inorganica Chim. Acta* **79**, 87–88 (1983).
96. Stuhrmann, H. Contrast variation in X-ray and neutron scattering. *J. Appl. Cryst.* **40**, s23–s27 (2007).
97. Sztucki, M., Di Cola, E. & Narayanan, T. Anomalous small-angle X-ray scattering from charged soft matter. *Eur. Phys. J. Spec. Top.* **208**, 319–331 (2012).
98. Das, R. et al. Counterion distribution around DNA probed by solution X-ray scattering. *Phys. Rev. Lett.* **90**, 188103 (2003).
99. Zettl, T. et al. Absolute intramolecular distance measurements with angstrom-resolution using anomalous small-angle X-ray scattering. *Nano Lett.* **16**, 5353–5357 (2016).
100. Gruzinov, A. Y. et al. Anomalous SAXS at P12 beamline EMBL Hamburg: instrumentation and applications. *J. Synchrotron Radiat.* **28**, 812–823 (2021).
101. Wieland, D. C. F. et al. ASAXS measurements on ferritin and apoferritin at the bioSAXS beamline P12 (PETRA III, DESY). *J. Appl. Cryst.* **54**, 830–838 (2021).
102. Goerigk, G., Schweins, R., Huber, K. & Ballauff, M. The distribution of Sr^{2+} counterions around polyacrylate chains analyzed by anomalous small-angle X-ray scattering. *Europhys. Lett.* **66**, 331–337 (2004).
103. Yu, C., Koh, S., Leisch, J. E., Toney, M. F. & Strasser, P. Size and composition distribution dynamics of alloy nanoparticle electrocatalysts probed by anomalous small angle X-ray scattering (ASAXS). *Faraday Discuss.* **140**, 283–296 (2009).
104. Narayanan, T. et al. A multipurpose instrument for time-resolved ultra-small-angle and coherent X-ray scattering. *J. Appl. Cryst.* **51**, 1511–1524 (2018).
105. Graceffa, R. et al. Sub-millisecond time-resolved SAXS using a continuous-flow mixer and X-ray microbeam. *J. Synchrotron Radiat.* **20**, 820–825 (2013).
106. Graber, T. et al. BioCARS: a synchrotron resource for time-resolved X-ray science. *J. Synchrotron Radiat.* **18**, 658–670 (2011).
107. Cho, H. S., Schotte, F., Dashdorj, N., Kyndt, J. & Anfinrud, P. A. Probing anisotropic structure changes in proteins with picosecond time-resolved small-angle X-ray scattering. *J. Phys. Chem. B* **117**, 15825–15832 (2013).
108. Burian, M. et al. Picosecond pump-probe X-ray scattering at the Elettra SAXS beamline. *J. Synchrotron Radiat.* **27**, 51–59 (2020).
109. Weigand, S. J. & Keane, D. T. DND-CAT's new triple area detector system for simultaneous data collection at multiple length scales. *Nucl. Instrum. Methods Phys. Res. A Accel. Spectrom. Detect. Assoc. Equip.* **649**, 61–63 (2011).
110. Takata, S.-i. et al. The design and *q* resolution of the small and wide angle neutron scattering instrument (TAIKAN) in J-PARC. *JPS Conf. Proc.* **8**, 036020 (2015).
111. Kirby, N. M. et al. A low-background-intensity focusing small-angle X-ray scattering undulator beamline. *J. Appl. Cryst.* **46**, 1670–1680 (2013).
112. Pernot, P. et al. Upgraded ESRF BM29 beamline for SAXS on macromolecules in solution. *J. Synchrotron Radiat.* **20**, 660–664 (2013).
113. Blanchet, C. E. et al. Versatile sample environments and automation for biological solution X-ray scattering experiments at the P12 beamline (PETRA III, DESY). *J. Appl. Cryst.* **48**, 431–443 (2015).
114. Cowieson, N. P. et al. Beamline B21: high-throughput small-angle X-ray scattering at Diamond Light Source. *J. Synchrotron Radiat.* **27**, 1438–1446 (2020).
115. Jeng, U.-S. et al. A small/wide-angle X-ray scattering instrument for structural characterization of air–liquid interfaces, thin films and bulk specimens. *J. Appl. Cryst.* **43**, 110–121 (2010).
116. Liu, G. et al. Upgraded SSRF BL19U2 beamline for small-angle X-ray scattering of biological macromolecules in solution. *J. Appl. Cryst.* **51**, 1633–1640 (2018).
117. Bras, W. et al. Recent experiments on a small-angle/wide-angle X-ray scattering beam line at the ESRF. *J. Appl. Cryst.* **36**, 791–794 (2003).
118. Ilavsky, J. et al. Ultra-small-angle X-ray scattering instrument at the advanced photon source: history, recent development, and current status. *Metall. Mater. Trans. A* **44A**, 68–76 (2013).
119. Sztucki, M. & Narayanan, T. Development of an ultra-small-angle X-ray scattering instrument for probing the microstructure and the dynamics of soft matter. *J. Appl. Cryst.* **40**, s459–s462 (2007).
120. Andersen, K. H. et al. The instrument suite of the European Spallation Source. *Nucl. Instrum. Methods Phys. Res. A Accel. Spectrom. Detect. Assoc. Equip.* **957**, 163402 (2020).
121. Arai, M. & Maekawa, F. Japan Spallation Neutron Source (JSNS) of J-PARC. *Nucl. Phys. N.* **19**, 34–39 (2009).
122. Mason, T. E. et al. The Spallation Neutron Source in Oak Ridge: a powerful tool for materials research. *Phys. B: Condens. Matter* **385–386**, 955–960 (2006).
123. Heller, W. T. et al. The suite of small-angle neutron scattering instruments at Oak Ridge National Laboratory. *J. Appl. Cryst.* **51**, 242–248 (2018).
124. Richards, J. J., Gagnon, C. V. L., Krzywon, J. R., Wagner, N. J. & Butler, P. D. Dielectric RheoSANS — simultaneous interrogation of impedance, rheology and small angle neutron scattering of complex fluids. *JoVE* **122**, e55318 (2017).
125. Gurnon, A. K. et al. Measuring material microstructure under flow using 1–2 plane flow-small angle neutron scattering. *JoVE* **84**, e51068 (2014).
126. Navarro-López, A. et al. Furnace for in situ and simultaneous studies of nano-precipitates and phase transformations in steels by SANS and neutron diffraction. *Rev. Sci. Instrum.* **91**, 123903 (2020).
127. Widmann, T. et al. Flexible sample environment for the investigation of soft matter at the european spallation source: Part II — the GISANS setup. *Appl. Sci.* **11**, 4036 (2021).
128. Carl, N., Prévost, S., Schweins, R. & Huber, K. Contrast variation of micelles composed of Ca^{2+} and block copolymers of two negatively charged polyelectrolytes. *Colloid Polym. Sci.* **298**, 663–679 (2020).
129. Shibayama, M., Matsunaga, T. & Nagao, M. Evaluation of incoherent scattering intensity by transmission and sample thickness. *J. Appl. Cryst.* **42**, 621–628 (2009).
130. Avers, K. E. et al. Broken time-reversal symmetry in the topological superconductor UPt3. *Nat. Phys.* **16**, 531–535 (2020).
131. Wood, K. et al. QUOKKA, the pinhole small-angle neutron scattering instrument at the OPAL Research Reactor, Australia: design, performance, operation and scientific highlights. *J. Appl. Cryst.* **51**, 294–314 (2018).
132. Babcock, E. & Ioffe, A. Polarized ^{3}He neutron spin filter program at the JCNS. *Phys. B: Condens. Matter* **406**, 2448–2452 (2011).
133. Koizumi, S. et al. Focusing and polarized neutron small-angle scattering spectrometer (SANS-J-II). The challenge of observation over length scales from an angstrom to a micrometre. *J. Appl. Cryst.* **40**, s474–s479 (2007).
134. Gabel, F. et al. Protein dynamics studied by neutron scattering. *Q. Rev. Biophys.* **35**, 327–367 (2002).
135. Svergun, D. I. & Nierhaus, K. H. A map of protein–rRNA distribution in the 70S *Escherichia coli* ribosome. *J. Biol. Chem.* **275**, 14432–14439 (2000).
136. Svergun, D. I. et al. Solution scattering structural analysis of the 70S *Escherichia coli* ribosome by contrast variation. I. Invariants and validation of electron microscopy models. *J. Mol. Biol.* **271**, 588–601 (1997).
137. Svergun, D. I. et al. Solution scattering structural analysis of the 70S *Escherichia coli* ribosome by contrast variation. II. A model of the ribosome and its RNA at 3.5 nm resolution. *J. Mol. Biol.* **271**, 602–618 (1997).
138. Dewhurst, C. Novel multiple-beam very small angle neutron scattering (VSANS) using a conventional SANS instrument. *J. Appl. Cryst.* **47**, 1180–1189 (2014).
139. Van Every, E., Deyhim, A. & Kulesza, J. New very small angle neutron scattering (VSANS) instrument. *J. Phys. Conf. Ser.* **746**, 012025 (2016).
140. Vogtt, K. et al. A new time-of-flight small-angle scattering instrument at the Helmholtz-Zentrum Berlin: V16/VSANS. *J. Appl. Cryst.* **47**, 237–244 (2014).
141. Abbas, S. et al. On the design and experimental realization of a multislit-based very small angle neutron scattering instrument at the European Spallation Source. *J. Appl. Cryst.* **48**, 1242–1253 (2015).
142. Brûlet, A. et al. Toward a new lower limit for the minimum scattering vector on the very small angle neutron scattering spectrometer at Laboratoire Leon Brillouin. *J. Appl. Cryst.* **41**, 161–166 (2008).

143. Barker, J. G. et al. Design and performance of a thermal-neutron double-crystal diffractometer for USANS at NIST. *J. Appl. Cryst.* **38**, 1004–1011 (2005).
144. Rekveldt, M. T. et al. Spin-echo small angle neutron scattering in Delft. *Rev. Sci. Instrum.* **76**, 033901 (2005).
145. Andersson, R., Van Heijkamp, L. F., De Schepper, I. M. & Bouwman, W. G. Analysis of spin-echo small-angle neutron scattering measurements. *J. Appl. Cryst.* **41**, 868–885 (2008).
146. Rehm, C., Barker, J., Bouwman, W. G. & Pynn, R. DCD USANS and SESANS: a comparison of two neutron scattering techniques applicable for the study of large-scale structures. *J. Appl. Cryst.* **46**, 354–364 (2013).
147. Krouglov, T. et al. Structural transitions of hard-sphere colloids studied by spin-echo small-angle neutron scattering. *J. Appl. Cryst.* **36**, 1417–1423 (2003).
148. Tromp, R. H. & Bouwman, W. G. A novel application of neutron scattering on dairy products. *Food Hydrocoll.* **21**, 154–158 (2007).
149. Parnell, S. R. et al. Porosity of silica Stöber particles determined by spin-echo small angle neutron scattering. *Soft Matter* **12**, 4709–4714 (2016).
150. Smith, G. N. et al. Spin-echo small-angle neutron scattering (SESANS) studies of diblock copolymer nanoparticles. *Soft Matter* **15**, 17–21 (2019).
151. Schmitt, J. et al. Mesoporous silica formation mechanisms probed using combined spin-echo modulated small-angle neutron scattering (SEMSANS) and small-angle neutron scattering (SANS). *ACS Appl. Mater. Interfaces* **12**, 28461–28473 (2020).
152. Biswas, P., Sen, D. & Bouwman, W. Structural characterization of spray-dried microgranules by spin-echo small-angle neutron scattering. *Powder Technol.* **378**, 680–684 (2021).
153. Glinka, C. et al. Sub-millisecond time-resolved small-angle neutron scattering measurements at NIST. *J. Appl. Cryst.* **53**, 598–604 (2020).
154. Glinka, C. J. et al. The 30 m small-angle neutron scattering instruments at the National Institute of Standards and Technology. *J. Appl. Cryst.* **31**, 430–445 (1998).
155. Lindner, P. & Schweins, R. The D11 small-angle scattering instrument: a new benchmark for SANS. *Neutron. N.* **21**, 15–18 (2010).
156. Feoktystov, A. V. et al. KWS-1 high-resolution small-angle neutron scattering instrument at JCNS: current state. *J. Appl. Cryst.* **48**, 61–70 (2015).
157. Dewhurst, C. D. et al. The small-angle neutron scattering instrument D33 at the Institut Laue-Langevin. *J. Appl. Cryst.* **49**, 1–14 (2016).
158. Nelson, A. R. J. & Dewhurst, C. D. Towards a detailed resolution smearing kernel for time-of-flight neutron reflectometers. Corrigendum. *J. Appl. Cryst.* **47**, 1162 (2014).
159. Hammouda, B. & Mildner, D. F. R. Small-angle neutron scattering resolution with refractive optics. *J. Appl. Cryst.* **40**, 250–259 (2007).
160. Sokolova, A. et al. Performance and characteristics of the BILBY time-of-flight small-angle neutron scattering instrument. *J. Appl. Cryst.* **52**, 1–12 (2019).
161. Kampmann, R. et al. Horizontal ToF-neutron reflectometer REFSANS at FRM-II Munich/Germany: first tests and status. *Phys. B Condens. Matter* **385-386**, 1161–1163 (2006).
162. Heenan, R. K. et al. Small angle neutron scattering using SANS2D. *Neutron. N.* **22**, 19–21 (2011).
163. Koizumi, S. et al. Advanced small-angle scattering instrument available in the Tokyo area. Time-of-flight, small-angle neutron scattering developed on the iMATERIA diffractometer at the high intensity pulsed neutron source J-PARC. *Quantum Beam Sci.* **4**, 42 (2020).
164. Rauscher, M. et al. Grazing incidence small angle X-ray scattering from free-standing nanostructures. *J. Appl. Phys.* **86**, 6763–6769 (1999).
165. Huang, T. C., Toraya, H., Blanton, T. N. & Wu, Y. X-ray powder diffraction analysis of silver behenate, a possible low-angle diffraction standard. *J. Appl. Cryst.* **26**, 180–184 (1993).
166. Keiderling, U., Gilles, R. & Wiedenmann, A. Application of silver behenate powder for wavelength calibration of a SANS instrument — a comprehensive study of experimental setup variations and data processing techniques. *J. Appl. Cryst.* **32**, 456–463 (1999).
167. Nygård, K., Bunk, O., Perret, E., David, C. & van der Veen, J. F. Diffraction gratings as small-angle X-ray scattering calibration standards. *J. Appl. Cryst.* **43**, 350–351 (2010).
168. Pauw, B. R., Smith, A. J., Snow, T., Terrill, N. J. & Thunemann, A. F. The modular small-angle X-ray scattering data correction sequence. *J. Appl. Cryst.* **50**, 1800–1811 (2017).
169. Pedersen, J. S. Resolution effects and analysis of small-angle neutron-scattering data. *J. Phys. Iv* **3**, 491–498 (1993).
170. Mildner, D. F. R. & Carpenter, J. M. Optimization of the experimental resolution for small-angle scattering. *J. Appl. Cryst.* **17**, 249–256 (1984).
171. Rennie, A. R. et al. Learning about SANS instruments and data reduction from round robin measurements on samples of polystyrene latex. *J. Appl. Cryst.* **46**, 1289–1297 (2013).
172. Hajizadeh, N. R., Franke, D. & Svergun, D. I. Integrated beamline control and data acquisition for small-angle X-ray scattering at the P12 BioSAXS beamline at PETRAIII storage ring DESY. *J. Synchrotron Radiat.* **25**, 906–914 (2018).
173. Franke, D., Kikhney, A. G. & Svergun, D. I. Automated acquisition and analysis of small angle X-ray scattering. *Data. Nuc. Instr. Meth Phys. Res. Sect. A* **689**, 52–59 (2012).
174. Mühlbauer, S. et al. The new small-angle neutron scattering instrument SANS-1 at MLZ — characterization and first results. *Nucl. Instrum. Methods Phys. Res. A Accel. Spectrom. Detect. Assoc. Equip.* **832**, 297–305 (2016).
175. Karge, L., Gilles, R. & Busch, S. Calibrating SANS data for instrument geometry and pixel sensitivity effects: access to an extended *Q* range. *J. Appl. Cryst.* **50**, 1382–1394 (2017).
176. Lindner, P., Leclercq, F. & Damay, P. Analysis of water scattering used for calibration of small-angle neutron scattering (SANS) measurements. *Phys. B Condens. Matter* **291**, 152–158 (2000).
177. Brûlet, A., Lairez, D., Lapp, A. & Cotton, J.-P. Improvement of data treatment in small-angle neutron scattering. *J. Appl. Cryst.* **40**, 165–177 (2007).
178. Strzalka, J. A corrective prescription for GISAXS. *IUCrJ* **5**, 661–662 (2018).
179. Liu, J. & Yager, K. G. Unwarping GISAXS data. *IUCrJ* **5**, 737–752 (2018).
180. Brönnimann, C. & Trüb, P. in *Synchrotron Light Sources and Free-Electron Lasers: Accelerator Physics, Instrumentation and Science Applications* (eds Jaeschke, E. J., Khan, S., Schneider, J. R., & Hastings,J. B.) 995–1027 (Springer International, 2016).
181. Casanas, A. et al. EIGER detector: application in macromolecular crystallography. *Acta Crystallogr. Sect. D* **72**, 1036–1048 (2016).
182. Maj, P. et al. HyPix-3000 - a large area single-photon counting detector with two discriminator thresholds. *2014 IEEE Nuclear Science Symposium and Medical Imaging Conference (NSS/MIC)* https://doi.org/10.1109/NSSMIC.2014.7431095 (2014).
183. Kanaki, K. et al. A novel small-angle neutron scattering detector geometry. *J. Appl. Cryst.* **46**, 1031–1037 (2013).
184. Seibert, J., Boone, J. & Lindfors, K. *Flat-Field Correction Technique for Digital Detectors* Vol. 3336 (SPIE, 1998).
185. Zhang, F. et al. Glassy carbon as an absolute intensity calibration standard for small-angle scattering. *Metall. Mater. Trans. A* **41**, 1151–1158 (2010).
186. Fan, L., Degen, M., Bendle, S., Grupido, N. & Ilavsky, J. The absolute calibration of a small-angle scattering instrument with a laboratory X-ray source. *J. Phys. Conf. Ser.* **247**, 012005 (2010).
187. Orthaber, D., Bergmann, A. & Glatter, O. SAXS experiments on absolute scale with Kratky systems using water as a secondary standard. *J. Appl. Cryst.* **33**, 218–225 (2000).
188. Wignall, G. D. & Bates, F. S. Absolute calibration of small-angle neutron scattering data. *J. Appl. Cryst.* **20**, 28–40 (1987).
189. Dreiss, C. A., Jack, K. S. & Parker, A. P. On the absolute calibration of bench-top small-angle X-ray scattering instruments: a comparison of different standard methods. *J. Appl. Cryst.* **39**, 32–38 (2006).
190. Allen, A. J., Zhang, F., Kline, R. J., Guthrie, W. F. & Ilavsky, J. NIST Standard Reference Material 3600: absolute intensity calibration standard for small-angle X-ray scattering. *J. Appl. Cryst.* **50**, 462–474 (2017).
191. Bras, W., Koizumi, S. & Terrill, N. J. Beyond simple small-angle X-ray scattering: developments in online complementary techniques and sample environments. *IUCrJ* **1**, 478–491 (2014).
192. Georgiadis, M. et al. 3D scanning SAXS: a novel method for the assessment of bone ultrastructure orientation. *Bone* **71**, 42–52 (2015).
193. Salditt, T. & Köster, S. in *Nanoscale Photonic Imaging* (eds Salditt, T., Egner, A., & Luke, D. R.) 405–433 (Springer International, 2020).
194. Rai, D. K. et al. High-pressure small-angle X-ray scattering cell for biological solutions and soft materials. *J. Appl. Cryst.* **54**, 111–122 (2021).
195. Narayanan, T., Dattani, R., Möller, J. & Kwaśniewski, P. A microvolume shear cell for combined rheology and X-ray scattering experiments. *Rev. Sci. Instrum.* **91**, 085102 (2020).
196. Nogales, A., Thornley, S. A. & Mitchell, G. R. Shear cell for in situ WAXS, SAXS, and SANS experiments on polymer melts under flow fields. *J. Macromol. Sci. B* **43**, 1161–1170 (2004).
197. Zákutná, D. et al. In situ magnetorheological SANS setup at Institut Laue-Langevin. *Colloid Polym. Sci.* **299**, 281–288 (2021).
198. Schroer, M. A. et al. Smaller capillaries improve the small-angle X-ray scattering signal and sample consumption for biomacromolecular solutions. *J. Synchrotron Radiat.* **25**, 1113–1122 (2018).
199. Bucciarelli, S. et al. Size-exclusion chromatography small-angle X-ray scattering of water soluble proteins on a laboratory instrument. *J. Appl. Cryst.* **51**, 1623–1632 (2018).
200. Johansen, N. T., Pedersen, M. C., Porcar, L., Martel, A. & Arleth, L. Introducing SEC–SANS for studies of complex self-organized biological systems. *Acta Crystallogr. Sect. D.* **74**, 1178–1191 (2018).
201. Mathew, E., Mirza, A. & Menhart, N. Liquid-chromatography-coupled SAXS for accurate sizing of aggregating proteins. *J. Synchrotron Radiat.* **11**, 314–318 (2004).
202. Pérez, J. & Vachette, P. in *Biological Small Angle Scattering: Techniques, Strategies and Tips* (eds Chaudhuri, B., Muñoz, I. G., Qian, S. & Urban, V. S.) 183–199 (Springer, 2017).
203. Hutin, S., Brennich, M., Maillot, B. & Round, A. Online ion-exchange chromatography for small-angle X-ray scattering. *Acta Crystallogr. Sect. D.* **72**, 1090–1099 (2016).
204. Brennich, M. E., Round, A. R. & Hutin, S. Online size-exclusion and ion-exchange chromatography on a SAXS beamline. *JoVE* **119**, e54861 (2017).
205. Graewert, M. A. et al. Adding size exclusion chromatography (SEC) and light scattering (LS) devices to obtain high-quality small angle X-ray scattering (SAXS) data. *Crystals* **10**, 975 (2020).
206. Cammarata, M. et al. Tracking the structural dynamics of proteins in solution using time-resolved wide-angle X-ray scattering. *Nat. Methods* **5**, 881–886 (2008).
207. Möller, J., Léonardon, J., Gorini, J., Dattani, R. & Narayanan, T. A sub-ms pressure jump setup for time-resolved X-ray scattering. *Rev. Sci. Instrum.* **87**, 125116 (2016).
208. Rössle, M. et al. Time-resolved small-angle neutron scattering of proteins in solution. *Phys. B Condens. Matter* **276-278**, 532–533 (2000).
209. Terashima, T. et al. In situ and time-resolved small-angle neutron scattering observation of star polymer formation via arm-linking reaction in ruthenium-catalyzed living radical polymerization. *Macromolecules* **43**, 8218–8232 (2010).
210. Mason, T. G. & Lin, M. Y. Time-resolved small angle neutron scattering measurements of asphaltene nanoparticle aggregation kinetics in incompatible crude oil mixtures. *J. Chem. Phys.* **119**, 565–571 (2003).
211. Grillo, I. Applications of stopped-flow in SAXS and SANS. *Curr. Opin. Colloid Interface Sci.* **14**, 402–408 (2009).
212. Helfer, E., Panine, P., Carlier, M.-F. & Davidson, P. The interplay between viscoelastic and thermodynamic properties determines the birefringence of F-actin gels. *Biophys. J.* **89**, 543–553 (2005).
213. Babonneau, D. FitGISAXS: software package for modelling and analysis of GISAXS data using IGOR Pro. *J. Appl. Cryst.* **43**, 929–936 (2010).
214. Chourou, S. T., Sarje, A., Li, X. S., Chan, E. R. & Hexemer, A. HipGISAXS: a high-performance computing code for simulating grazing-incidence X-ray scattering data. *J. Appl. Cryst.* **46**, 1781–1795 (2013).
215. Lazzari, R. IsGISAXS: a program for grazing-incidence small-angle X-ray scattering analysis of supported islands. *J. Appl. Cryst.* **35**, 406–421 (2002).
216. Pospelov, G. et al. BornAgain: software for simulating and fitting grazing-incidence small-angle scattering. *J. Appl. Cryst.* **53**, 262–276 (2020).

217. Tian, B. et al. Small angle neutron scattering quantifies the hierarchical structure in fibrous calcium caseinate. *Food Hydrocoll.* **106**, 105912 (2020).
218. Stribeck, N., Almendarez Camarillo, A., Nöchel, U., Bösecke, P. & Bayer, R. K. Early oriented isothermal crystallization of polyethylene studied by high-time-resolution SAXS/WAXS. *Anal. Bioanal. Chem.* **387**, 649 (2006).
219. Krishnamurthy, A. et al. Multiscale polymer dynamics in hierarchical carbon nanotube grafted glass fiber reinforced composites. *ACS Appl. Polym. Mater.* **1**, 1905–1917 (2019).
220. Huang, X. et al. In situ constructing the kinetic roadmap of octahedral nanocrystal assembly toward controlled superlattice fabrication. *J. Am. Chem. Soc.* **143**, 4234–4243 (2021).
221. Akcora, P. et al. Anisotropic self-assembly of spherical polymer-grafted nanoparticles. *Nat. Mater.* **8**, 354–359 (2009).
222. Beaucage, G. Approximations leading to a unified exponential/power-law approach to small-angle scattering. *J. Appl. Cryst.* **28**, 717–728 (1995).
223. Beaucage, G. & Schaefer, D. W. Structural studies of complex systems using small-angle scattering: a unified Guinier/power-law approach. *J. Noncryst. Solids* **172–174**, 797–805 (1994).
224. Mylonas, E. & Svergun, D. I. Accuracy of molecular mass determination of proteins in solution by small-angle X-ray scattering. *J. Appl. Cryst.* **40**, S245–S249 (2007).
225. Stribeck, N. & Nochel, U. A method for merging of ultra-small-angle X-ray scattering and smeared small-angle X-ray scattering patterns of fibers. *J. Appl. Cryst.* **41**, 715–722 (2008).
226. Skou, S., Gillilan, R. E. & Ando, N. Synchrotron-based small-angle X-ray scattering of proteins in solution. *Nat. Protoc.* **9**, 1727–1739 (2014).
227. Porod, G. Die Rontgenkleinwinkelstreuung Von Dichtgepackten Kolloiden Systemen. 1 [German]. *Kolloid Z. Z Polym.* **124**, 83–114 (1951).
228. Debye, P., Anderson, H. R. Jr & Brumberger, H. Scattering by an inhomogeneous solid. II. The correlation function and its application. *J. Appl. Phys.* **28**, 679–683 (1957).
229. Rambo, R. P. & Tainer, J. A. Characterizing flexible and intrinsically unstructured biological macromolecules by SAS using the Porod–Debye law. *Biopolymers* **95**, 559–571 (2011).
230. Franke, D., Jeffries, C. M. & Svergun, D. I. Machine learning methods for X-ray scattering data analysis from biomacromolecular solutions. *Biophys. J.* **114**, 2485–2492 (2018).
231. Hammouda, B. A new Guinier–Porod model. *J. Appl. Cryst.* **43**, 716–719 (2010).
232. Receveur-Brechot, V. & Durand, D. How random are intrinsically disordered proteins? A small angle scattering perspective. *Curr. Protein Peptide Sci.* **13**, 55–75 (2012).
233. Svergun, D. I., Semenyuk, A. V. & Feigin, L. A. Small-angle-scattering-data treatment by the regularization method. *Acta Crystallogr. Sect. A* **44**, 244–250 (1988).
234. Hansen, S. & Pedersen, J. S. A comparison of 3 different methods for analyzing small-angle scattering data. *J. Appl. Cryst.* **24**, 541–548 (1991).
235. Glatter, O. Convolution square root of band-limited symmetrical functions and its application to small-angle scattering data. *J. Appl. Cryst.* **14**, 101–108 (1981).
236. Glatter, O. & Hainisch, B. Improvements in real-space deconvolution of small-angle scattering data. *J. Appl. Cryst.* **17**, 435–441 (1984).
237. Oliveira, C. L. P. et al. Gaussian deconvolution: a useful method for a form-free modeling of scattering data from mono- and multilayered planar systems. *J. Appl. Cryst.* **45**, 1278–1286 (2012).
238. Rayleigh, L. The incidence of light upon a transparent sphere of dimensions comparable with the wave-length. *P R. Soc. Lond. Conta* **84**, 25–46 (1910).
239. Pedersen, J. S. Analysis of small-angle scattering data from colloids and polymer solutions: modeling and least-squares fitting. *Adv. Colloid Interfac.* **70**, 171–210 (1997).
240. Pedersen, J. S. in *Neutrons, X-Rays and Light: Scattering Methods Applied to Soft Condensed Matter* (eds Lindner, P. & Zemb, T.) 391–420 (Elsevier, 2002).
241. Konarev, P. V. & Svergun, D. I. A posteriori determination of the useful data range for small-angle scattering experiments on dilute monodisperse systems. *IUCrJ* **2**, 352–360 (2015).
242. Franke, D., Jeffries, C. M. & Svergun, D. I. Correlation map, a goodness-of-fit test for one-dimensional X-ray scattering spectra. *Nat. Methods* **12**, 419–422 (2015).
243. Svergun, D. I. & Pedersen, J. S. Propagating errors in small-angle scattering data treatment. *J. Appl. Cryst.* **27**, 241–248 (1994).
244. Pedersen, J. S., Posselt, D. & Mortensen, K. Analytical treatment of the resolution function for small-angle scattering. *J. Appl. Cryst.* **23**, 321–333 (1990).
245. Caponetti, E., Floriano, M. A., Didio, E. & Triolo, R. On the shape of the radial-distribution function of an assembly of monodisperse ellipsoidal scatterers. *J. Appl. Cryst.* **26**, 612–615 (1993).
246. Glatter, O. Determination of particle-size distribution-functions from small-angle scattering data by means of the indirect transformation method. *J. Appl. Cryst.* **13**, 7–11 (1980).
247. Pedersen, J. S. Determination of size distributions from small-angle scattering data for systems with effective hard-sphere interactions. *J. Appl. Cryst.* **27**, 595–608 (1994).
248. Pauw, B. R., Kastner, C. & Thunemann, A. F. Nanoparticle size distribution quantification: results of a small-angle X-ray scattering inter-laboratory comparison. *J. Appl. Cryst.* **50**, 1280–1288 (2017).
249. Pedersen, J. S. Analysis of small-angle scattering data from micelles and microemulsions: free-form approaches and model fitting. *Curr. Opin. Colloid Interface Sci.* **4**, 190–196 (1999).
250. Shipovskov, S. et al. Water-in-oil micro-emulsion enhances the secondary structure of a protein by confinement. *Chemphyschem* **13**, 3179–3184 (2012).
251. Kirste, R. G., Oberthur, R. C. in *Small Angle X-ray Scattering* (eds Glatter, O. & Kratky, O.) 387–431 (Academic, 1982).
252. Menon, S. V. G., Manohar, C. & Srinivasa Rao, K. A new interpretation of the sticky hard sphere model. *J. Chem. Phys.* **95**, 9186–9190 (1991).
253. Percus, J. K. & Yevick, G. J. Analysis of classical statistical mechanics by means of collective coordinates. *Phys. Rev.* **110**, 1–13 (1958).
254. Sharma, R. V. & Sharma, K. C. The structure factor and the transport properties of dense fluids having molecules with square well potential, a possible generalization. *Phys. A Stat. Mech. Appl.* **89**, 213–218 (1977).
255. Kinning, D. J. & Thomas, E. L. Hard-sphere interactions between spherical domains in diblock copolymers. *Macromolecules* **17**, 1712–1718 (1984).
256. Debye, P. Molecular-weight determination by light scattering. *J. Phys. Colloid Chem.* **51**, 18–32 (1947).
257. Benoit, H. On the effect of branching and polydispersity on the angular distribution of the light scattered by Gaussian coils. *J. Polym. Sci.* **11**, 507–510 (1953).
258. Svaneborg, C. & Pedersen, J. S. A formalism for scattering of complex composite structures. I. Applications to branched structures of asymmetric sub-units. *J. Chem. Phys.* **136**, 104105 (2012).
259. Pedersen, J. S. & Gerstenberg, M. C. Scattering form factor of block copolymer micelles. *Macromolecules* **29**, 1363–1365 (1996).
260. Burchard, W. & Kajiwara, K. Statistics of stiff chain molecules.1. Particle scattering factor. *Proc. R. Soc. Lon. A* **316**, 185 (1970).
261. Debye, P. X-ray dispersal. *Ann. Phys. Berlin* **46**, 809–823 (1915).
262. Bernado, P., Mylonas, E., Petoukhov, M. V., Blackledge, M. & Svergun, D. I. Structural characterization of flexible proteins using small-angle X-ray scattering. *J. Am. Chem. Soc.* **129**, 5656–5664 (2007).
263. Franke, D. & Svergun, D. I. DAMMIF, a program for rapid ab-initio shape determination in small-angle scattering. *J. Appl. Cryst.* **42**, 342–346 (2009).
264. Svergun, D., Barberato, C. & Koch, M. H. J. CRYSOL — a program to evaluate X-ray solution scattering of biological macromolecules from atomic coordinates. *J. Appl. Cryst.* **28**, 768–773 (1995).
265. Svergun, D. I. Restoring low resolution structure of biological macromolecules from solution scattering using simulated annealing. *Biophys. J.* **77**, 2896–2896 (1999).
266. Panjkovich, A. & Svergun, D. I. Deciphering conformational transitions of proteins by small angle X-ray scattering and normal mode analysis. *Phys. Chem. Chem. Phys.* **18**, 5707–5719 (2016).
267. Petoukhov, M. V. et al. Reconstruction of quaternary structure from X-ray scattering by equilibrium mixtures of biological macromolecules. *Biochemistry* **52**, 6844–6855 (2013).
268. Petoukhov, M. V. & Svergun, D. I. Global rigid body modeling of macromolecular complexes against small-angle scattering data. *Biophys. J.* **89**, 1237–1250 (2005).
269. Schneidman-Duhovny, D., Hammel, M. & Sali, A. FoXS: a web server for rapid computation and fitting of SAXS profiles. *Nucleic Acids Res.* **38**, W540–W544 (2010).
270. Grudinin, S., Garkavenko, M. & Kazennov, A. Pepsi-SAXS: an adaptive method for rapid and accurate computation of small-angle X-ray scattering profiles. *Acta Cryst. Sect. D.* **73**, 449–464 (2017).
271. Svergun, D. I. et al. Protein hydration in solution: experimental observation by X-ray and neutron scattering. *Proc. Natl Acad. Sci. USA* **95**, 2267–2272 (1998).
272. Schneidman-Duhovny, D., Hammel, M., Tainer, John, A. & Sali, A. Accurate SAXS profile computation and its assessment by contrast variation experiments. *Biophys. J.* **105**, 962–974 (2013).
273. Schneidman-Duhovny, D., Hammel, M., Tainer, J. A. & Sali, A. FoXS, FoXSDock and MultiFoXS: single-state and multi-state structural modeling of proteins and their complexes based on SAXS profiles. *Nucleic Acids Res.* **44**, W424–W429 (2016).
274. Petoukhov, M. V. et al. New developments in the ATSAS program package for small-angle scattering data analysis. *J. Appl. Cryst.* **45**, 342–350 (2012).
275. Svergun, D. I., Petoukhov, M. V. & Koch, M. H. J. Determination of domain structure of proteins from X-ray solution scattering. *Biophys. J.* **80**, 2946–2953 (2001).
276. Kozin, M. B. & Svergun, D. I. Automated matching of high- and low-resolution structural models. *J. Appl. Cryst.* **34**, 33–41 (2001).
277. Tria, G., Mertens, H. D. T., Kachala, M. & Svergun, D. I. Advanced ensemble modelling of flexible macromolecules using X-ray solution scattering. *IUCrJ* **2**, 207–217 (2015).
278. Arnold, T. et al. Implementation of a beam deflection system for studies of liquid interfaces on beamline I07 at Diamond. *J. Synchrotron Radiat.* **19**, 408–416 (2012).
279. Seeck, O. H. et al. The high-resolution diffraction beamline P08 at PETRA III. *J. Synchrotron Radiat.* **19**, 30–38 (2012).
280. Annighöfer, B. et al. A high pressure cell using metallic windows to investigate the structure of molecular solutions up to 600 MPa by small-angle neutron scattering. *Rev. Sci. Instrum.* **90**, 025106 (2019).
281. Schroer, M. A. et al. High-pressure SAXS study of folded and unfolded ensembles of proteins. *Biophys. J.* **99**, 3430–3437 (2010).
282. Singh, I., Themistou, E., Porcar, L. & Neelamegham, S. Fluid shear induces conformation change in human blood protein von Willebrand factor in solution. *Biophys. J.* **96**, 2313–2320 (2009).
283. Josts, I. et al. Structural kinetics of MsbA investigated by stopped-flow time-resolved small-angle X-ray scattering. *Structure* **28**, 348–354.e3 (2020).
284. Ibrahim, Z. et al. Time-resolved neutron scattering provides new insight into protein substrate processing by a AAA+ unfoldase. *Sci. Rep.* **7**, 40948 (2017).
285. Weiss, T. M. et al. Dynamics of the self-assembly of unilamellar vesicles. *Phys. Rev. Lett.* **94**, 038303 (2005).
286. Mertens, H. D. T. & Svergun, D. I. Structural characterization of proteins and complexes using small-angle X-ray solution scattering. *J. Struct. Biol.* **172**, 128–141 (2010).
287. Schneidman-Duhovny, D. & Hammel, M. Modeling structure and dynamics of protein complexes with SAXS profiles. *Methods Mol. Biol.* **1764**, 449–473 (2018).
288. Kikhney, A. G. & Svergun, D. I. A practical guide to small angle X-ray scattering (SAXS) of flexible and intrinsically disordered proteins. *FEBS Lett.* **589**, 2570–2577 (2015).
289. Sagar, A., Svergun, D. & Bernadó, P. in *Intrinsically Disordered Proteins: Methods and Protocols* (eds Kragelund, B. B. & Skriver, K.) 249–269 (Springer, 2020).
290. Konarev, P. V., Volkov, V. V., Sokolova, A. V., Koch, M. H. J. & Svergun, D. I. PRIMUS: a Windows PC-based system for small-angle scattering data analysis. *J. Appl. Cryst.* **36**, 1277–1282 (2003).
291. Konarev, P. V. & Svergun, D. I. Direct shape determination of intermediates in evolving macromolecular solutions from small-angle scattering data. *IUCrJ* **5**, 402–409 (2018).

292. Burian, M. & Amenitsch, H. Dummy-atom modelling of stacked and helical nanostructures from solution scattering data. *IUCrJ* **5**, 390–401 (2018).
293. Mertens, H. D. T. & Svergun, D. I. Combining NMR and small angle X-ray scattering for the study of biomolecular structure and dynamics. *Arch. Biochem. Biophys.* **628**, 33–41 (2017).
294. Evrard, G., Mareuil, F., Bontems, F., Sizun, C. & Perez, J. DADIMODO: a program for refining the structure of multidomain proteins and complexes against small-angle scattering data and NMR-derived restraints. *J. Appl. Cryst.* **44**, 1264–1271 (2011).
295. Zhao, C. & Shukla, D. SAXS-guided enhanced unbiased sampling for structure determination of proteins and complexes. *Sci. Rep.* **8**, 17748 (2018).
296. Grant, T. D. Ab initio electron density determination directly from solution scattering data. *Nat. Methods* **15**, 191–193 (2018).
297. Konarev, P. V. & Svergun, D. I. Limitations of the iterative electron density reconstruction algorithm from solution scattering data. *Nat. Methods* **18**, 244–245 (2021).
298. Grant, T. D. Reply to: Limitations of the iterative electron density reconstruction algorithm from solution scattering data. *Nat. Methods* **18**, 246–248 (2021).
299. Perez, J. & Koutsioubas, A. Memprot: a program to model the detergent corona around a membrane protein based on SEC-SAXS data. *Acta Crystallogr.D.* **71**, 86–93 (2015).
300. Pedersen, M. C., Arleth, L. & Mortensen, K. WillItFit: a framework for fitting of constrained models to small-angle scattering data. *J. Appl. Cryst.* **46**, 1894–1898 (2013).
301. Trewhella, J., Gallagher, S. C., Krueger, J. K. & Zhao, J. Neutron and X-ray solution scattering provide insights into biomolecular structure and function. *Sci. Prog.* **81**, 101–122 (1998).
302. Olah, G. A., Rokop, S. E., Wang, C. L. A., Blechner, S. L. & Trewhella, J. Troponin I encompasses an extended Troponin C in the Ca^{2+}-bound complex: a small-angle X-ray and neutron scattering study. *Biochemistry* **33**, 8233–8239 (1994).
303. Olah, G. A. & Trewhella, J. A model structure of the muscle protein complex $4Ca^{2+}$ · Troponin C · Troponin I derived from small-angle scattering data: implications for regulation. *Biochemistry* **33**, 12800–12806 (1994).
304. Jeffries, C. M., Pietras, Z. & Svergun, D. I. The basics of small-angle neutron scattering (SANS for new users of structural biology). *EPJ Web Conf.* **236**, 03001 (2020).
305. Cornilescu, G. et al. Structural analysis of multi-helical RNAs by NMR–SAXS/WAXS: application to the U4/U6 di-snRNA. *J. Mol. Biol.* **428**, 777–789 (2016).
306. Schwieters, C. D. et al. Solution structure of the 128 kDa enzyme I dimer from *Escherichia coli* and Its 146 kDa complex with HPr using residual dipolar couplings and small- and wide-angle X-ray scattering. *J. Am. Chem. Soc.* **132**, 13026–13045 (2010).
307. Mahieu, E. & Gabel, F. Biological small-angle neutron scattering: recent results and development. *Acta Cryst. D.* **74**, 715–726 (2018).
308. Zhao, J., Hoye, E., Boylan, S., Walsh, D. A. & Trewhella, J. Quaternary structures of a catalytic subunit-regulatory subunit dimeric complex and the holoenzyme of the cAMP-dependent protein kinase by neutron contrast variation. *J. Biol. Chem.* **273**, 30448–30459 (1998).
309. Krueger, J. K., Gallagher, S. C., Wang, C. L. A. & Trewhella, J. Calmodulin remains extended upon binding to smooth muscle caldesmon: a combined small-angle scattering and Fourier transform infrared spectroscopy study. *Biochemistry* **39**, 3979–3987 (2000).
310. Whitten, A. E. et al. The structure of the KinA–Sda complex suggests an allosteric mechanism of histidine kinase inhibition. *J. Mol. Biol.* **368**, 407–420 (2007).
311. Maric, S. et al. Time-resolved small-angle neutron scattering as a probe for the dynamics of lipid exchange between human lipoproteins and naturally derived membranes. *Sci. Rep.* **9**, 7591 (2019).
312. Maric, S. et al. Stealth carriers for low-resolution structure determination of membrane proteins in solution. *Acta Cryst. D. Biol. Cryst.* **70**, 317–328 (2014).
313. Koutsioubas, A., Berthaud, A., Mangenot, S. & Pérez, J. Ab initio and all-atom modeling of detergent organization around Aquaporin-0 based on SAXS data. *J. Phys. Chem. B* **117**, 13588–13594 (2013).
314. Bengtsen, T. et al. Structure and dynamics of a nanodisc by integrating NMR, SAXS and SANS experiments with molecular dynamics simulations. *eLife* **9**, e56518 (2020).
315. Whitten, A. E., Jeffries, C. M., Harris, S. P. & Trewhella, J. Cardiac myosin-binding protein C decorates F-actin: implications for cardiac function. *Proc. Natl Acad. Sci. USA* **105**, 18360–18365 (2008).
316. Majorošová, J. et al. Effect of the concentration of protein and nanoparticles on the structure of biohybrid nanocomposites. *Biopolymers* **111**, e23342 (2020).
317. Johansen, D., Jeffries, C. M. J., Hammouda, B., Trewhella, J. & Goldenberg, D. P. Effects of macromolecular crowding on an intrinsically disordered protein characterized by small-angle neutron scattering with contrast matching. *Biophys. J.* **100**, 1120–1128 (2011).
318. Hirai, M. et al. Observation of protein and lipid membrane structures in a model mimicking the molecular-crowding environment of cells using neutron scattering and cell debris. *J. Phys. Chem. B* **123**, 3189–3198 (2019).
319. Giehm, L., Svergun, D. I., Otzen, D. E. & Vestergaard, B. Low-resolution structure of a vesicle disrupting α-synuclein oligomer that accumulates during fibrillation. *Proc. Natl Acad. Sci. USA* **108**, 3246–3251 (2011).
320. Langkilde, A. E., Morris, K. L., Serpell, L. C., Svergun, D. I. & Vestergaard, B. The architecture of amyloid-like peptide fibrils revealed by X-ray scattering, diffraction and electron microscopy. *Acta Cryst. Sect. D* **71**, 882–895 (2015).
321. Vestergaard, B. et al. A helical structural nucleus is the primary elongating unit of insulin amyloid fibrils. *PLoS Biol.* **5**, e134 (2007).
322. Zheng, W. et al. Probing the action of chemical denaturant on an intrinsically disordered protein by simulation and experiment. *J. Am. Chem. Soc.* **138**, 11702–11713 (2016).
323. Fuertes, G. et al. Decoupling of size and shape fluctuations in heteropolymeric sequences reconciles discrepancies in SAXS vs. FRET measurements. *Proc. Natl Acad. Sci. USA* **114**, E6342–E6351 (2017).
324. Vestergaard, B. Analysis of biostructural changes, dynamics, and interactions — small-angle X-ray scattering to the rescue. *Arch. Biochem. Biophys.* **602**, 69–79 (2016).
325. Kirby, N. M. & Cowieson, N. P. Time-resolved studies of dynamic biomolecules using small angle X-ray scattering. *Curr. Opin. Struct. Biol.* **28**, 41–46 (2014).
326. Czajka, A. & Armes, S. P. Time-resolved small-angle X-ray scattering studies during aqueous emulsion polymerization. *J. Am. Chem. Soc.* **143**, 1474–1484 (2021).
327. Lund, R. et al. Structural observation and kinetic pathway in the formation of polymeric micelles. *Phys. Rev. Lett.* **102**, 188301 (2009).
328. Jensen, G. V. et al. Direct observation of the formation of surfactant micelles under nonisothermal conditions by synchrotron SAXS. *J. Am. Chem. Soc.* **135**, 7214–7222 (2013).
329. Kalkowski, J. et al. In situ measurements of polymer micellization kinetics with millisecond temporal resolution. *Macromolecules* **52**, 3151–3157 (2019).
330. Hayward, D. W., Chiappisi, L., Prévost, S., Schweins, R. & Gradzielski, M. A small-angle neutron scattering environment for in-situ observation of chemical processes. *Sci. Rep.* **8**, 7299 (2018).
331. Keidel, R. et al. Time-resolved structural evolution during the collapse of responsive hydrogels: the microgel-to-particle transition. *Sci. Adv.* **4**, eaao7086 (2018).
332. Sankhala, K. et al. Self-assembly of block copolymers during hollow fiber spinning: an in situ small-angle X-ray scattering study. *Nanoscale* **11**, 7634–7647 (2019).
333. Räntzsch, V. et al. Polymer crystallization studied by hyphenated rheology techniques: rheo-NMR, rheo-SAXS, and rheo-microscopy. *Macromol. Mater. Eng.* **304**, 1800586 (2018).
334. Zhu, P. et al. The segmental responses to orientation and relaxation of thermoplastic poly(ether-ester) elastomer during cyclic deformation: an in-situ WAXD/SAXS study. *Polymer* **188**, 122120 (2020).
335. McCulloch, B. et al. Dynamics of magnetic alignment in rod–coil block copolymers. *Macromolecules* **46**, 4462–4471 (2013).
336. Schaff, F. et al. Six-dimensional real and reciprocal space small-angle X-ray scattering tomography. *Nature* **527**, 353–356 (2015).
337. Liebi, M. et al. Nanostructure surveys of macroscopic specimens by small-angle scattering tensor tomography. *Nature* **527**, 349–352 (2015).
338. Conceição, A. L. C., Perlich, J., Haas, S. & Funari, S. S. SAXS-CT: a nanostructure resolving microscopy for macroscopic biologic specimens. *Biomed. Phys. Eng. Express* **6**, 035012 (2020).
339. Lee, S. et al. In situ study of ABC triblock terpolymer self-assembly under solvent vapor annealing. *Macromolecules* **52**, 1853–1863 (2019).
340. Meyer, A. et al. In situ grazing-incidence small-angle X-ray scattering observation of block-copolymer templated formation of magnetic nanodot arrays and their magnetic properties. *Nano Res.* **10**, 456–471 (2017).
341. Li, Z. et al. Linking experiment and theory for three-dimensional networked binary metal nanoparticle–triblock terpolymer superstructures. *Nat. Commun.* **5**, 3247 (2014).
342. Li, T., Senesi, A. J. & Lee, B. Small angle X-ray scattering for nanoparticle research. *Chem. Rev.* **116**, 11128–11180 (2016).
343. Liu, X. et al. Effects of geometric confinement on caging and dynamics of polymer-tethered nanoparticle suspensions. *Macromolecules* **54**, 426–439 (2021).
344. Kusano, T. et al. Interplay between interparticle potential and adsorption structure in nanoparticle dispersions with polymer addition as displayed by small-angle scattering. *Langmuir* **37**, 7503–7512 (2021).
345. Toso, S. et al. Multilayer diffraction reveals that colloidal superlattices approach the structural perfection of single crystals. *ACS Nano* **15**, 6243–6256 (2021).
346. Dey, A. et al. State of the art and prospects for halide perovskite nanocrystals. *ACS Nano* **15**, 10775–10981 (2021).
347. De Geuser, F. & Deschamps, A. Precipitate characterisation in metallic systems by small-angle X-ray or neutron scattering. *Comptes Rendus Phys.* **13**, 246–256 (2012).
348. Preston, G. The diffraction of X-rays by age-hardening aluminium copper alloys. *Proc. R. Soc. A Math. Phys. Sci.* **167**, 526–538 (1938).
349. Zhang, F. et al. In situ structural characterization of ageing kinetics in aluminum alloy 2024 across angstrom-to-micrometer length scales. *Acta Mater.* **111**, 385–398 (2016).
350. Mathon, M. H. et al. A SANS investigation of the irradiation-enhanced α–α′ phases separation in 7–12 Cr martensitic steels. *J. Nucl. Mater.* **312**, 236–248 (2003).
351. Kelly, T. F. in *Springer Handbook of Microscopy* (eds Hawkes, P. W. & Spence, J. C. H.) 715–763 (Springer International, 2019).
352. Briggs, S. A. et al. A combined APT and SANS investigation of α′ phase precipitation in neutron-irradiated model FeCrAl alloys. *Acta Mater.* **129**, 217–228 (2017).
353. Ohnuma, M. et al. A new method for the quantitative analysis of the scale and composition of nanosized oxide in 9Cr-ODS steel. *Acta Mater.* **57**, 5571–5581 (2009).
354. Anovitz, L. M. & Cole, D. R. Characterization and analysis of porosity and pore structures. *Rev. Mineral. Geochem.* **80**, 61–164 (2015).
355. Hall, P. L., Mildner, D. F. R. & Borst, R. L. Small-angle scattering studies of the pore spaces of shaly rocks. *J. Geophys. Res. Solid. Earth* **91**, 2183–2192 (1986).
356. Radlinski, A. P., Boreham, C. J., Wignall, G. D. & Lin, J. S. Microstructural evolution of source rocks during hydrocarbon generation: a small-angle-scattering study. *Phys. Rev. B* **53**, 14152–14160 (1996).
357. Anovitz, L. M. et al. A new approach to quantification of metamorphism using ultra-small and small angle neutron scattering. *Geochim. Cosmochim. Acta* **73**, 7303–7324 (2009).
358. Clarkson, C. R. et al. Pore structure characterization of North American shale gas reservoirs using USANS/SANS, gas adsorption, and mercury intrusion. *Fuel* **103**, 606–616 (2013).
359. Allen, A. J., Thomas, J. J. & Jennings, H. M. Composition and density of nanoscale calcium–silicate–hydrate in cement. *Nat. Mater.* **6**, 311–316 (2007).
360. Allen, A. Time-resolved phenomena in cements, clays and porous rocks. *J. Appl. Cryst.* **24**, 624–634 (1991).
361. Thomas, J. J., Jennings, H. M. & Allen, A. J. The surface area of hardened cement paste as measured by various techniques. *Concr. Sci. Eng.* **1**, 45–64 (1999).
362. Paul, T. et al. Quantification of thermal oxidation in metallic glass powder using ultra-small angle X-ray scattering. *Sci. Rep.* **9**, 6836 (2019).

363. Lee, S. et al. Oxidative decomposition of methanol on subnanometer palladium clusters: the effect of catalyst size and support composition. *J. Phys. Chem. C.* **114**, 10342–10348 (2010).
364. Lee, S., Lee, B., Seifert, S., Vajda, S. & Winans, R. E. Simultaneous measurement of X-ray small angle scattering, absorption and reactivity: a continuous flow catalysis reactor. *Nucl. Instrum. Methods Phys. Res. A Accel. Spectrom. Detect. Assoc. Equip.* **649**, 200–203 (2011).
365. Jiang, Z., Lee, D. R., Narayanan, S., Wang, J. & Sinha, S. K. Waveguide-enhanced grazing-incidence small-angle X-ray scattering of buried nanostructures in thin films. *Phys. Rev. B* **84**, 075440 (2011).
366. Trewhella, J. et al. Report of the wwPDB Small-Angle Scattering Task Force: data requirements for biomolecular modeling and the PDB. *Structure* **21**, 875–881 (2013).
367. Trewhella, J. et al. 2017 publication guidelines for structural modelling of small-angle scattering data from biomolecules in solution: an update. *Acta Crystallogr. D Struct. Biol.* **73**, 710–728 (2017).
368. Pearson, K. X. On the criterion that a given system of deviations from the probable in the case of a correlated system of variables is such that it can be reasonably supposed to have arisen from random sampling. *London, Edinburgh Dublin Philos. Mag. J. Sci.* **50**, 157–175 (1900).
369. Kikhney, A. G., Borges, C. R., Molodenskiy, D. S., Jeffries, C. M. & Svergun, D. I. SASBDB: towards an automatically curated and validated repository for biological scattering data. *Protein Sci.* **29**, 66–75 (2020).
370. Valentini, E., Kikhney, A. G., Previtali, G., Jeffries, C. M. & Svergun, D. I. SASBDB, a repository for biological small-angle scattering data. *Nucleic Acids Res.* **43**, D357–D363 (2015).
371. Varadi, M. et al. pE-DB: a database of structural ensembles of intrinsically disordered and of unfolded proteins. *Nucleic Acids Res.* **42**, D326–D335 (2014).
372. Vallat, B., Webb, B., Westbrook, J. D., Sali, A. & Berman, H. M. Development of a prototype system for archiving integrative/hybrid structure models of biological macromolecules. *Structure* **26**, 894–904. e2 (2018).
373. Ward, A. B., Sali, A. & Wilson, I. A. Biochemistry. Integrative structural biology. *Science* **339**, 913–915 (2013).
374. Sali, A. et al. Outcome of the First wwPDB Hybrid/Integrative Methods Task Force Workshop. *Structure* **23**, 1156–1167 (2015).
375. Hall, S. R., Allen, F. H. & Brown, I. D. The Crystallographic Information File (CIF): a new standard archive file for crystallography. *Acta Crystallogr. Sect. A* **47**, 655–685 (1991).
376. Adams, P. D. et al. Announcing mandatory submission of PDBx/mmCIF format files for crystallographic depositions to the Protein Data Bank (PDB). *Acta Crystallogr. Sect. D.* **75**, 451–454 (2019).
377. Kachala, M., Westbrook, J. & Svergun, D. Extension of the sasCIF format and its applications for data processing and deposition. *J. Appl. Cryst.* **49**, 302–310 (2016).
378. Konnecke, M. et al. The NeXus data format. *J. Appl. Cryst.* **48**, 301–305 (2015).
379. Jemian, P. R. et al. NXcanSAS: standard to store reduced SAS data of any dimension. *Acta Crystallogr. Sect. A* **73**, C1442 (2017).
380. Petoukhov, M. V. & Svergun, D. I. Ambiguity assessment of small-angle scattering curves from monodisperse systems. *Acta Crystallogr. Sect. D* **71**, 1051–1058 (2015).
381. Stachowski, T. R., Snell, M. E. & Snell, E. H. SAXS studies of X-ray induced disulfide bond damage: engineering high-resolution insight from a low-resolution technique. *PLoS ONE* **15**, e0239702 (2020).
382. Brooks-Bartlett, J. C. et al. Development of tools to automate quantitative analysis of radiation damage in SAXS experiments. *J. Synchrotron Radiat.* **24**, 63–72 (2017).
383. Hopkins, J. B. & Thorne, R. E. Quantifying radiation damage in biomolecular small-angle X-ray scattering. *J. Appl. Cryst.* **49**, 880–890 (2016).
384. Jeffries, C. M., Graewert, M. A., Svergun, D. I. & Blanchet, C. E. Limiting radiation damage for high-brilliance biological solution scattering: practical experience at the EMBL P12 beamline PETRAIII. *J. Synchrotron Radiat.* **22**, 273–279 (2015).
385. Castellví, A., Pascual-Izarra, C., Crosas, E., Malfois, M. & Juanhuix, J. Improving data quality and expanding BioSAXS experiments to low-molecular-weight and low-concentration protein samples. *Acta Crystallogr. D* **76**, 971–981 (2020).
386. Kirby, N. et al. Improved radiation dose efficiency in solution SAXS using a sheath flow sample environment. *Acta Crystallogr. D* **72**, 1254–1266 (2016).
387. Ryan, T. M. et al. An optimized SEC-SAXS system enabling high X-ray dose for rapid SAXS assessment with correlated UV measurements for biomolecular structure analysis. *J. Appl. Cryst.* **51**, 97–111 (2018).
388. Kuwamoto, S., Akiyama, S. & Fujisawa, T. Radiation damage to a protein solution, detected by synchrotron X-ray small-angle scattering: dose-related considerations and suppression by cryoprotectants. *J. Synchrotron Radiat.* **11**, 462–468 (2004).
389. Lopez, C. G. et al. Microfluidic devices for small-angle neutron scattering. *J. Appl. Cryst.* **51**, 570–583 (2018).
390. Ghosh, R. E. & Rennie, A. R. Assessment of detector calibration materials for SANS experiments. *J. Appl. Cryst.* **32**, 1157–1163 (1999).
391. Do, C. et al. Understanding inelastically scattered neutrons from water on a time-of-flight small-angle neutron scattering (SANS) instrument. *Nucl. Instrum. Methods Phys. Res. A: Accel. Spectrom. Detect. Assoc. Equip.* **737**, 42–46 (2014).
392. Oba, Y. et al. Magnetic scattering in the simultaneous measurement of small-angle neutron scattering and Bragg edge transmission from steel. *J. Appl. Cryst.* **49**, 1659–1664 (2016).
393. Tremsin, A. S. et al. Energy-resolved neutron imaging options at a small angle neutron scattering instrument at the Australian Center for Neutron Scattering. *Rev. Sci. Instrum.* **90**, 035114 (2019).
394. Rubinson, K. A., Stanley, C. & Krueger, S. Small-angle neutron scattering and the errors in protein structures that arise from uncorrected background and intermolecular interactions. *J. Appl. Cryst.* **41**, 456–465 (2008).
395. Jacrot, B. & Zaccai, G. Determination of molecular weight by neutron scattering. *Biopolymers* **20**, 2413–2426 (1981).
396. Chen, P.-c, Masiewicz, P., Perez, K. & Hennig, J. Structure-based screening of binding affinities via small-angle X-ray scattering. *IUCrJ* **7**, 644–655 (2020).
397. Inoue, R. et al. Newly developed laboratory-based size exclusion chromatography small-angle X-ray scattering system (La-SSS). *Sci. Rep.* **9**, 12610 (2019).
398. Brookes, E., Vachette, P., Rocco, M. & Perez, J. US-SOMO HPLC-SAXS module: dealing with capillary fouling and extraction of pure component patterns from poorly resolved SEC–SAXS data. *J. Appl. Cryst.* **49**, 1827–1841 (2016).
399. Meisburger, S. P., Xu, D. & Ando, N. REGALS: a general method to deconvolve X-ray scattering data from evolving mixtures. *IUCrJ* **8**, 225–237 (2021).
400. Baxter, R. J. Percus–Yevick equation for hard spheres with surface adhesion. *J. Chem. Phys.* **49**, 2770–2774 (1968).
401. De Kruif, C. G. et al. Adhesive hard-sphere colloidal dispersions. A small-angle neutron-scattering study of stickiness and the structure factor. *Langmuir* **5**, 422–428 (1989).
402. Derjaguin, B. V., Churaev, N. V. & Muller, V. M. in *Surface Forces* 293–310 (Springer, 1987).
403. Kotlarchyk, M., Stephens, R. B. & Huang, J. S. Study of Schultz distribution to model polydispersity of microemulsion droplets. *J. Phys. Chem.* **92**, 1533–1538 (1988).
404. Copley, J. The significance of multiple scattering in the interpretation of small-angle neutron scattering experiments. *J. Appl. Cryst.* **21**, 639–644 (1988).
405. Jensen, G. V. & Barker, J. G. Effects of multiple scattering encountered for various small-angle scattering model functions. *J. Appl. Cryst.* **51**, 1455–1466 (2018).
406. Frielinghaus, H. Strategies for removing multiple scattering effects revisited. *Nucl. Instrum. Methods Phys. Res. A: Accel. Spectrom. Detect. Assoc. Equip.* **904**, 9–14 (2018).
407. Allen, A. J. & Berk, N. F. Analysis of small-angle scattering data dominated by multiple scattering for systems containing eccentrically shaped particles or pores. *J. Appl. Cryst.* **27**, 878–891 (1994).
408. Folkertsma, L. et al. Synchrotron SAXS and impedance spectroscopy unveil nanostructure variations in redox-responsive porous membranes from poly(ferrocenylsilane) poly(ionic liquid)s. *Macromolecules* **50**, 296–302 (2017).
409. Metwalli, E. et al. A novel experimental approach for nanostructure analysis: simultaneous small-angle X-ray and neutron scattering. *J. Appl. Cryst.* **53**, 722–733 (2020).
410. Koczwara, C. et al. Towards real-time ion-specific structural sensitivity in nanoporous carbon electrodes using in situ anomalous small-angle X-ray scattering. *ACS Appl. Mater. Interfaces* **11**, 42214–42220 (2019).
411. Martinez, N. et al. Real time monitoring of water distribution in an operando fuel cell during transient states. *J. Power Sour.* **365**, 230–234 (2017).
412. Morin, A. et al. Quantitative multi-scale operando diagnosis of water localization inside a fuel cell. *J. Electrochem. Soc.* **164**, F9–F21 (2016).
413. Martinez, N. et al. Combined operando high resolution SANS and neutron imaging reveals in-situ local water distribution in an operating fuel cell. *ACS Appl. Energy Mater.* **2**, 8425–8433 (2019).
414. Bauer, P. S. et al. In-situ aerosol nanoparticle characterization by small angle X-ray scattering at ultra-low volume fraction. *Nat. Commun.* **10**, 1122 (2019).
415. Guizar-Sicairos, M., Georgiadis, M. & Liebi, M. Validation study of small-angle X-ray scattering tensor tomography. *J. Synchrotron Radiat.* **27**, 779–787 (2020).
416. Lee, J. et al. In situ measurement of ionomer water content and liquid water saturation in fuel cell catalyst layers by high-resolution small-angle neutron scattering. *ACS Appl. Energy Mater.* **3**, 8393–8401 (2020).
417. Lahey-Rudolph, J. M. et al. Rapid screening of in cellulo grown protein crystals via a small-angle X-ray scattering/X-ray powder diffraction synergistic approach. *J. Appl. Cryst.* **53**, 1169–1180 (2020).
418. Cai, J., Townsend, J. P., Dodson, T. C., Heiney, P. A. & Sweeney, A. M. Eye patches: protein assembly of index-gradient squid lenses. *Science* **357**, 564–569 (2017).
419. Yip, K. M., Fischer, N., Paknia, E., Chari, A. & Stark, H. Atomic-resolution protein structure determination by cryo-EM. *Nature* **587**, 157–161 (2020).
420. Nakane, T. et al. Single-particle cryo-EM at atomic resolution. *Nature* **587**, 152–156 (2020).
421. Amann-Winkel, K. et al. X-ray and neutron scattering of water. *Chem. Rev.* **116**, 7570–7589 (2016).
422. Kim, HenryS. et al. SAXS/SANS on supercharged proteins reveals residue-specific modifications of the hydration shell. *Biophys. J.* **110**, 2185–2194 (2016).
423. Gabel, F. & Bellissent-Funel, M.-C. C-Phycocyanin hydration water dynamics in the presence of trehalose: an incoherent elastic neutron scattering study at different energy resolutions. *Biophys. J.* **92**, 4054–4063 (2007).
424. Schirò, G. et al. Translational diffusion of hydration water correlates with functional motions in folded and intrinsically disordered proteins. *Nat. Commun.* **6**, 6490 (2015).
425. Niskanen, J. et al. Compatibility of quantitative X-ray spectroscopy with continuous distribution models of water at ambient conditions. *Proc. Natl Acad. Sci. USA* **116**, 4058–4063 (2019).
426. Bu, W. & Schlossman, M. L. in *Synchrotron Light Sources and Free-Electron Lasers: Accelerator Physics, Instrumentation and Science Applications* (eds Jaeschke, E. J., Khan, S., Schneider, J. R. & Hastings, J. B.) 1897–1933 (Springer International, 2020).
427. Franke, D. et al. ATSAS 2.8: a comprehensive data analysis suite for small-angle scattering from macromolecular solutions. *J. Appl. Cryst.* **50**, 1212–1225 (2017).
428. Grishaev, A., Guo, L., Irving, T. & Bax, A. Improved fitting of solution X-ray scattering data to macromolecular structures and structural ensembles by explicit water modeling. *J. Am. Chem. Soc.* **132**, 15484–15486 (2010).
429. Hopkins, J. B., Gillilan, R. E. & Skou, S. BioXTAS RAW: improvements to a free open-source program for small-angle X-ray scattering data reduction and analysis. *J. Appl. Cryst.* **50**, 1545–1553 (2017).
430. Perkins, S. J. et al. Atomistic modelling of scattering data in the Collaborative Computational Project for Small Angle Scattering (CCP-SAS). *J. Appl. Cryst.* **49**, 1861–1875 (2016).
431. Ginsburg, A. et al. D+: software for high-resolution hierarchical modeling of solution X-ray scattering from complex structures. *J. Appl. Cryst.* **52**, 219–242 (2019).

432. Filik, J. et al. Processing two-dimensional X-ray diffraction and small-angle scattering data in DAWN 2. *J. Appl. Cryst.* **50**, 959–966 (2017).
433. Benecke, G. et al. A customizable software for fast reduction and analysis of large X-ray scattering data sets: applications of the new DPDAK package to small-angle X-ray scattering and grazing-incidence small-angle X-ray scattering. *J. Appl. Cryst.* **47**, 1797–1803 (2014).
434. Hammersley, A. FIT2D: a multi-purpose data reduction, analysis and visualization program. *J. Appl. Cryst.* **49**, 646–652 (2016).
435. Dewhurst, C. GRASP: Graphical Reduction and Analysis SANS Program for Matlab. *ILL Neutrons for Society* https://www.ill.eu/users/support-labs-infrastructure/software-scientific-tools/grasp/ (2003).
436. Bergmann, A., Fritz, G. & Glatter, O. Solving the generalized indirect Fourier transformation (GIFT) by Boltzmann simplex simulated annealing (BSSA). *J. Appl. Cryst.* **33**, 1212–1216 (2000).
437. Jiang, Z. GIXSGUI: a MATLAB toolbox for grazing-incidence X-ray scattering data visualization and reduction, and indexing of buried three-dimensional periodic nanostructured films. *J. Appl. Cryst.* **48**, 917–926 (2015).
438. Ilavsky, J. & Jemian, P. R. Irena: tool suite for modeling and analysis of small-angle scattering. *J. Appl. Cryst.* **42**, 347–353 (2009).
439. Arnold, O. et al. Mantid — data analysis and visualization package for neutron scattering and μ SR experiments. *Nucl. Instrum. Methods Phys. Res. A Accel. Spectrom. Detect. Assoc. Equip.* **764**, 156–166 (2014).
440. Ilavsky, J. Nika: software for two-dimensional data reduction. *J. Appl. Cryst.* **45**, 324–328 (2012).
441. Kline, S. Reduction and analysis of SANS and USANS data using IGOR Pro. *J. Appl. Cryst.* **39**, 895–900 (2006).
442. Förster, S., Apostol, L. & Bras, W. Scatter: software for the analysis of nano- and mesoscale small-angle scattering. *J. Appl. Cryst.* **43**, 639–646 (2010).
443. Breßler, I., Kohlbrecher, J. & Thunemann, A. F. SASfit: a tool for small-angle scattering data analysis using a library of analytical expressions. *J. Appl. Cryst.* **48**, 1587–1598 (2015).
444. Liu, C.-H. et al. sasPDF: pair distribution function analysis of nanoparticle assemblies from small-angle scattering data. *J. Appl. Cryst.* **53**, 699–709 (2020).
445. Brookes, E. & Rocco, M. Recent advances in the UltraScan SOlution MOdeller (US-SOMO) hydrodynamic and small-angle scattering data analysis and simulation suite. *Eur. Biophys. J.* **47**, 855–864 (2018).
446. Knight, C. J. & Hub, J. S. WAXSiS: a web server for the calculation of SAXS/WAXS curves based on explicit-solvent molecular dynamics. *Nucleic Acids Res.* **43**, W225–W230 (2015).
447. With, S. et al. Fast diffusion-limited lyotropic phase transitions studied in situ using continuous flow microfluidics/microfocus-SAXS. *Langmuir* **30**, 12494–12502 (2014).
448. Konishi, T. et al. Origin of SAXS intensity in the low-*q* region during the early stage of polymer crystallization from both the melt and glassy state. *Phys. Rev. Mater.* **2**, 105602 (2018).
449. Fleury, G. et al. Micellar-mediated block copolymer ordering dynamics revealed by in situ grazing incidence small-angle X-ray scattering during spin coating. *Adv. Funct. Mater.* **29**, 1806741 (2019).
450. Mable, C. J. et al. Time-resolved SAXS studies of the kinetics of thermally triggered release of encapsulated silica nanoparticles from block copolymer vesicles. *Macromolecules* **50**, 4465–4473 (2017).
451. Shim, J., Bates, F. S. & Lodge, T. P. Bicontinuous microemulsions in partially charged ternary polymer blends. *ACS Macro Lett.* **8**, 1166–1171 (2019).
452. Tashiro, K. & Yamamoto, H. Structural evolution mechanism of crystalline polymers in the isothermal melt-crystallization process: a proposition based on simultaneous WAXD/SAXS/FTIR measurements. *Polymers* **11**, 1316 (2019).
453. Samant, S. et al. Ordering pathway of block copolymers under dynamic thermal gradients studied by in situ GISAXS. *Macromolecules* **49**, 8633–8642 (2016).
454. Yu, F. et al. Block copolymer self-assembly-directed and transient laser heating-enabled nanostructures toward phononic and photonic quantum materials. *ACS Nano* **14**, 11273–11282 (2020).
455. Lopez, C. G., Watanabe, T., Martel, A., Porcar, L. & Cabral, J. T. Microfluidic-SANS: flow processing of complex fluids. *Sci. Rep.* **5**, 7727 (2015).
456. Philipp, M. et al. Sorption of water and initial stages of swelling of thin PNIPAM films using in situ GISAXS microfluidics. *Langmuir* **31**, 9619–9627 (2015).
457. Lin, Y.-J., Chuang, W.-T. & Hsu, S.-H. Gelation mechanism and structural dynamics of chitosan self-healing hydrogels by in situ SAXS and coherent X-ray scattering. *ACS Macro Lett.* **8**, 1449–1455 (2019).
458. Dunderdale, G. J., Davidson, S. J., Ryan, A. J. & Mykhaylyk, O. O. Flow-induced crystallisation of polymers from aqueous solution. *Nat. Commun.* **11**, 3372 (2020).
459. Schlenk, M. et al. Parallel and perpendicular alignment of anisotropic particles in free liquid microjets and emerging microdroplets. *Langmuir* **34**, 4843–4851 (2018).
460. Defebvin, J., Barrau, S., Stoclet, G., Rochas, C. & Lefebvre, J.-M. In situ SAXS/WAXS investigation of the structural evolution of poly(vinylidene fluoride) upon uniaxial stretching. *Polymer* **84**, 148–157 (2016).
461. Pepin, J., Gaucher, V., Rochas, C. & Lefebvre, J.-M. In-situ SAXS/WAXS investigations of the mechanically-induced phase transitions in semi-crystalline polyamides. *Polymer* **175**, 87–98 (2019).
462. Zhao, H. et al. A real-time WAXS and SAXS study of the structural evolution of LLDPE bubble. *J. Polym. Sci. Part. B Polym. Phys.* **56**, 1404–1412 (2018).
463. Cheshire, M. C. et al. Wellbore cement porosity evolution in response to mineral alteration during CO_2 flooding. *Environ. Sci. Technol.* **51**, 692–698 (2017).
464. Coakley, J. et al. Precipitation processes in the β-titanium alloy Ti–5Al–5Mo–5V–3Cr. *J. Alloy. Compd.* **646**, 946–953 (2015).
465. Alauhdin, M. et al. Monitoring morphology evolution within block copolymer microparticles during dispersion polymerisation in supercritical carbon dioxide: a high pressure SAXS study. *Polym. Chem.* **10**, 860–871 (2019).
466. Bahadur, J. et al. Determination of closed porosity in rocks by small-angle neutron scattering. *J. Appl. Cryst.* **49**, 2021–2030 (2016).
467. Hu, T. et al. Nondestructive and quantitative characterization of bulk injection-molded polylactide using SAXS microtomography. *Macromolecules* **53**, 6498–6509 (2020).
468. Leu, L. et al. Multiscale description of shale pore systems by scanning SAXS and WAXS microscopy. *Energy Fuels* **30**, 10282–10297 (2016).
469. Reichardt, M. et al. X-ray structural analysis of single adult cardiomyocytes: tomographic imaging and microdiffraction. *Biophys. J.* **119**, 1309–1323 (2020).
470. Gopinadhan, M. et al. Controlling orientational order in block copolymers using low-intensity magnetic fields. *Proc. Natl Acad. Sci. USA* **114**, E9437–E9444 (2017).
471. Gu, Y. et al. Photoswitching topology in polymer networks with metal–organic cages as crosslinks. *Nature* **560**, 65–69 (2018).
472. Harada, M. & Katagiri, E. Mechanism of silver particle formation during photoreduction using in situ time-resolved SAXS analysis. *Langmuir* **26**, 17896–17905 (2010).
473. Bikondoa, O., Carbone, D., Chamard, V. & Metzger, T. H. Ageing dynamics of ion bombardment induced self-organization processes. *Sci. Rep.* **3**, 1850 (2013).
474. Olichwer, N., Meyer, A., Yesilmen, M. & Vossmeyer, T. Gold nanoparticle superlattices: correlating chemiresistive responses with analyte sorption and swelling. *J. Mater. Chem. C* **4**, 8214–8225 (2016).
475. Hejral, U., Müller, P., Balmes, O., Pontoni, D. & Stierle, A. Tracking the shape-dependent sintering of platinum–rhodium model catalysts under operando conditions. *Nat. Commun.* **7**, 10964 (2016).
476. Mochizuki, T. et al. Temperature- and humidity-controlled SAXS analysis of proton-conductive ionomer membranes for fuel cells. *ChemSusChem* **7**, 729–733 (2014).
477. Schwartzkopf, M. et al. Role of sputter deposition rate in tailoring nanogranular gold structures on polymer surfaces. *ACS Appl. Mater. Interfaces* **9**, 5629–5637 (2017).
478. Zhang, P. et al. Manipulating the assembly of spray-deposited nanocolloids: in situ study and monolayer film preparation. *Langmuir* **32**, 4251–4258 (2016).
479. Dudenas, P. J. & Kusoglu, A. Evolution of ionomer morphology from dispersion to film: an in situ X-ray study. *Macromolecules* **52**, 7779–7785 (2019).
480. Dendooven, J. et al. Mobile setup for synchrotron based in situ characterization during thermal and plasma-enhanced atomic layer deposition. *Rev. Sci. Instrum.* **87**, 113905 (2016).
481. Ruge, M., Golks, F., Zegenhagen, J., Magnussen, O. M. & Stettner, J. In operando GISAXS studies of mound coarsening in electrochemical homoepitaxy. *Phys. Rev. Lett.* **112**, 055503 (2014).
482. Schaffer, C. J. et al. Morphological degradation in low bandgap polymer solar cells — an in operando study. *Adv. Energy Mater.* **6**, 1600712 (2016).
483. Kabir, S. et al. Elucidating the dynamic nature of fuel cell electrodes as a function of conditioning: an ex situ material characterization and in situ electrochemical diagnostic study. *ACS Appl. Mater. Interfaces* **11**, 45016–45030 (2019).
484. Hattendorff, J., Seidlmayer, S., Gasteiger, H. A. & Gilles, R. Li-ion half-cells studied operando during cycling by small-angle neutron scattering. *J. Appl. Cryst.* **53**, 210–221 (2020).
485. Allen, A. J., Ilavsky, J., Jemian, P. R. & Braun, A. Evolution of electrochemical interfaces in solid oxide fuel cells (SOFC): a Ni and Zr resonant anomalous ultra-small-angle X-ray scattering study with elemental and spatial resolution across the cell assembly. *RSC Adv.* **4**, 4676–4690 (2014).
486. Milsom, A. et al. The persistence of a proxy for cooking emissions in megacities: a kinetic study of the ozonolysis of self-assembled films by simultaneous small & wide angle X-ray scattering (SAXS/WAXS) and Raman microscopy. *Faraday Discuss.* **226**, 364–381 (2021).
487. Geuchies, J. J. et al. In situ study of the formation mechanism of two-dimensional superlattices from PbSe nanocrystals. *Nat. Mater.* **15**, 1248–1254 (2016).
488. Yang, F. et al. Investigation of the interaction between nafion ionomer and surface functionalized carbon black using both ultrasmall angle X-ray scattering and cryo-TEM. *ACS Appl. Mater. Interfaces* **9**, 6530–6538 (2017).
489. Rebollar, E. et al. In situ monitoring of laser-induced periodic surface structures formation on polymer films by grazing incidence small-angle X-ray scattering. *Langmuir* **31**, 3973–3981 (2015).
490. Ilavsky, J. et al. Ultra-small-angle X-ray scattering at the advanced photon source. *J. Appl. Cryst.* **42**, 469–479 (2009).
491. Ilavsky, J. et al. Development of combined microstructure and structure characterization facility for in situ and operando studies at the Advanced Photon Source. *J. Appl. Cryst.* **51**, 867–882 (2018).
492. Blanton, T. N. et al. JCPDS — International Centre for Diffraction Data round robin study of silver behenate. A possible low-angle X-ray diffraction calibration standard. *Powder Diffr.* **10**, 91–95 (1995).
493. Paula, F. Ld. O. SAXS analysis of magnetic field influence on magnetic nanoparticle clusters. *Condens. Matter* **4**, 55 (2019).
494. Moore, P. Small-angle scattering. Information content and error analysis. *J. Appl. Cryst.* **13**, 168–175 (1980).
495. Svergun, D. Determination of the regularization parameter in indirect-transform methods using perceptual criteria. *J. Appl. Cryst.* **25**, 495–503 (1992).
496. Provencher, S. W. A constrained regularization method for inverting data represented by linear algebraic or integral equations. *Computer Phys. Commun.* **27**, 213–227 (1982).
497. Liao, F. et al. Self-assembly of a silicon-containing side-chain liquid crystalline block copolymer in bulk and in thin films: kinetic pathway of a cylinder to sphere transition. *Nanoscale* **11**, 285–293 (2019).
498. Andrews, R. N., Serio, J., Muralidharan, G. & Ilavsky, J. An in situ USAXS–SAXS–WAXS study of precipitate size distribution evolution in a model Ni-based alloy. *J. Appl. Cryst.* **50**, 734–740 (2017).
499. Piiadov, V., Ares de Araújo, E., Oliveira Neto, M., Craievich, A. F. & Polikarpov, I. SAXSMoW 2.0:

online calculator of the molecular weight of proteins in dilute solution from experimental SAXS data measured on a relative scale. *Protein Sci.* **28**, 454–463 (2019).
500. Hajizadeh, N. R., Franke, D., Jeffries, C. M. & Svergun, D. I. Consensus Bayesian assessment of protein molecular mass from solution X-ray scattering data. *Sci. Rep.* **8**, 7204 (2018).
501. Rambo, R. P. & Tainer, J. A. Accurate assessment of mass, models and resolution by small-angle scattering. *Nature* **496**, 477–481 (2013).

Acknowledgements
The authors acknowledge the support of iNEXT-Discovery, project number 871037, funded by the Horizon 2020 programme of the European Commission and the Bundesministerium für Bildung und Forschung (BMBF) grant 16QK10A 'SAS-BSOFT' (to D.I.S.).

Author contributions
Introduction (C.M.J., D.I.S., J.S.P. and A.V.S.); Experimentation (C.M.J., D.I.S., J.I., A.Ma., S.H., A.Me., J.S.P. and A.V.S.); Results (C.M.J., D.I.S., J.I., J.S.P. and A.V.S.); Applications (C.M.J., D.I.S., J.I., S.H. and A.Me.); Reproducibility and data deposition (C.M.J., D.I.S. and J.I.); Limitations and optimizations (C.M.J., D.I.S., J.I., A.Ma., S.H., A.Me. and A.V.S.); Outlook (C.M.J., D.I.S., A.Ma. and A.V.S.); Overview of the Primer (D.I.S. and C.M.J.).

Competing interests
The authors declare no competing interests.

Peer review information
Nature Reviews Methods Primers thanks B. Abecassis, J. Lipfert, D. Zákutná and the other, anonymous, reviewer(s) for their contribution to the peer review of this work.

Publisher's note
Springer Nature remains neutral with regard to jurisdictional claims in published maps and institutional affiliations.

RELATED LINKS
Argonne National Laboratory SAXS and USAXS packages (Irena, Nika Indra): https://usaxs.xray.aps.anl.gov/software-description
As low as reasonably achievable (ALARA): https://www.cdc.gov/nceh/radiation/alara.html#::text=ALARA%20stands%20for%20%E2%80%9Cas%20low,time%2C%20distance%2C%20and%20shielding
BioXTAS RAW: https://bioxtas-raw.readthedocs.io/en/latest/
canSAS initiative: http://www.cansas.org
CCP-SAS web project: http://ccpsas.org/about.html
ESRF FIT2D home page: https://www.esrf.eu/computing/scientific/FIT2D/
ESRF SAXS program package: https://www.esrf.eu/home/UsersAndScience/Experiments/CBS/ID02/available_software/saxs-program-package.html
ESRF SAXS software tools: https://www.esrf.eu/home/UsersAndScience/Experiments/CBS/ID02/available_software.html
ESRF Scatter program for data analysis: https://www.esrf.eu/UsersAndScience/Experiments/CRG/BM26/SaxsWaxs/DataAnalysis/Scatter
European Molecular Biology Laboratory ATSAS data analysis software: https://www.embl-hamburg.de/biosaxs/software.html
European Molecular Biology Laboratory ATSAS online and web services: https://www.embl-hamburg.de/biosaxs/online.html
foXS: https://modbase.compbio.ucsf.edu/foxs/
GISAXS Community Website: http://gisaxs.com/index.php/Main_Page
GISAXS Community Website from the University of Hamburg: http://www.gisaxs.de/
GISAXS Community Website table of contents: http://gisaxs.com/index.php/Special:AllPages
GIXSGUI: https://www.aps.anl.gov/Science/Scientific-Software/GIXSGUI
HiPGISAXS: https://hipgisaxs.github.io/
ImageJ: https://imagej.nih.gov/ij/
Institut Laue-Langevin (ILL) - GRASP SANS analysis and data reduction: https://www.ill.eu/users/support-labs-infrastructure/software-scientific-tools/grasp
IsGISAXS: https://www.insp.upmc.fr/oxydes/IsGISAXS/isgisaxs.htm
Mantid: https://www.mantidproject.org/Main_Page
MULCh: ModULes for the analysis of Contrast variation data: https://smb-research.smb.usyd.edu.au/NCVWeb/
NIST Neutron activation and scattering calculator: https://www.ncnr.nist.gov/resources/activation/
NIST SANS and USANS data reduction and analysis software: https://www.nist.gov/ncnr/data-reduction-analysis/sans-software
NIST Scattering Length Density Calculator: https://www.ncnr.nist.gov/resources/sldcalc.html
NIST XCOM: Photon Cross Sections Database: https://www.nist.gov/pml/xcom-photon-cross-sections-database
NIST X-Ray Mass Attenuation Coefficients: https://www.nist.gov/pml/x-ray-mass-attenuation-coefficients
OneDep System: https://deposit-2.wwpdb.org/
Paul Scherrer Institute, PSI, SASfit package: https://www.psi.ch/en/sinq/sansi/sasfit
PDB-Dev databank: https://pdb-dev.wwpdb.org/
Pepsi-SAXS: https://team.inria.fr/nano-d/software/pepsi-saxs/
Protein Ensemble Database: https://proteinensemble.org
Resources from the National Institute of Standards and Technology: https://www.ncnr.nist.gov/resources/
SAS Portal: http://smallangle.org/
SASSIE-web: https://sassie-web.chem.utk.edu/sassie2/
SasView: https://www.sasview.org/
Saxier SAS forum: https://www.saxier.org/forum/
SAXSMoW (SAXS Molecular Weight): http://saxs.ifsc.usp.br/
ScÅtter, Lawrence Berkeley National Laboratory, Advanced Light Source: https://bl1231.als.lbl.gov/saxs_protocols/
SCATTER, ESRF: https://www.esrf.fr/UsersAndScience/Experiments/CRG/BM26/SaxsWaxs/DataAnalysis/Scatter
Small Angle Scattering Biological Data Bank (SASBDB): https://www.sasbdb.org/
UniProt nomenclature: www.uniprot.org
US-SOMO: https://somo.aucsolutions.com/
WAXSIS: http://waxsis.uni-goettingen.de/